



The University of Sheffield

Data-driven state estimation of large-scale battery systems

*A thesis submitted in partial fulfilment of the requirements for the degree of
Doctor of Philosophy*

Zhuo WANG

February 2022

Abstract

The system states of a grid-connected battery energy storage system (BESS), state of charge (SOC) and state of health (SOH), are essential for its control to trade energy and provide services such as frequency response. There is significant work in estimating these states at cell-level, however, for a large-scale BESS these methods have not been examined before to see whether they can scale. There are a number of challenges with large BESS that need to be considered. The first is that these often contain 10,000-100,000s of cells where interconnections make the system more complex. The second is that estimation methods rely on accurate and reliable measurements of voltage and current, for large BESS where the range of the sensors is larger the errors will be higher. This thesis also considers the real-world scenario where data granularity, accuracy and quality is variable.

In this work it is shown how cell-level state estimation techniques can be utilised on large-scale BESSs using experimental data from a 2MW, 1MWh BESS. The results show how a Dual Sigma Point Kalman Filter (DSPKF) SOC estimation can provide improved accuracy over the integrated commercial battery management system SOC estimation. It is then demonstrated how the DSPKF parameters can be tuned by a genetic algorithm to simplify selection to generalise the application of the method for different BESSs. Using system round-trip efficiency (RTE) measurements, validation on the accuracy of the methodology is provided.

This thesis also proposes how the improved SOC estimation can be combined with a total least-squares (TLS) method for capacity estimation to less than 1% error. To achieve this an approach is presented for data selection that is required to minimize the error. Finally, parameters of the equivalent circuit model (ECM) of BESSs are estimated in the weight filter of the DSPKF and the results are validated by a voltage simulation process. Throughout the thesis online system state estimation is demonstrated using both designed test and real-world operational data where the BESS has provided contracted frequency response services to the GB National Grid.

List of Publications

Parts of the work presented in this thesis have been reported in the following internationally-respected publications:

Journal Publications

1. **Z. Wang**, D. T. Gladwin, M. J. Smith and S. Haass, “Practical state estimation using Kalman filter methods for large-scale battery systems,” *Applied Energy*, vol. 294, July, 2021.

Conference Proceedings

1. **Z. Wang**, D. T. Gladwin, M. J. Smith and T. L. Fantham, “Data-selection for state estimation of large-scale battery systems,” *IECON*, October, 2021.

Acknowledgements

I am sincerely grateful for my supervisor Prof. Dan Gladwin's excellent guidance and support. Without him, the whole PhD journey would not happen.

I thank the funding from Siemens through EPSRC, making my work possible. My thanks to Dr Stefan Haass, Dr Timothy Hughes from Siemens particularly for their help through my PhD.

My gratitude to my parents, who has been educating me to enjoy my life and supporting me spiritually and financially. With their love, I feel I can overcome anything. I hope they can have a healthy and happy life coming.

I feel grateful to have wonderful colleagues in the research group and in the university. My special thanks to Dr Matt Smith and Tom Fantham, for their continuous help and the knowledge they share, which is important for my study. I also thank the critical help from Dr Shahab Nejad at the early stage of my PhD. My thanks to other academic staff in the department: Prof. Martin Foster, Prof. Dave Stone, Prof. Ziqiang Zhu and Prof. Chee Hing Tan.

I would like to thank Dr Rui Zhao, Dr Xiaolin Mou, John Lea-Wilson, Dr Rhys Munden, Andrew Rule, Zeyuan Wang and Yingcheng Wang for their friendship with me.

Finally, I would like to thank everyone who gave me support during my five-year study in Sheffield and every friend I have met.

Contents

Abstract	i
List of Publications	ii
Acknowledgements	iii
Nomenclature	xiv
List of Symbols	xvii
1 Introduction	1
1.1 Background & Motivation	1
1.2 Thesis Contributions	4
2 Literature Review	6
2.1 Definitions	6
2.2 Battery chemistries and the market	8
2.2.1 Lead-acid battery	8
2.2.2 Conventional lithium-ion batteries	8
2.2.3 Lithium-titanate battery	10
2.2.4 Sodium-ion battery	11
2.2.5 Sodium sulphur battery	11
2.2.6 Redox Flow battery	12
2.2.7 Lithium sulphur battery	12
2.2.8 Lithium-air battery	13
2.2.9 Solid state battery	13
2.2.10 Battery market	14
2.2.11 Summary	14
2.3 National Grid frequency response services	14
2.4 Battery systems and their management of optimisation	17
2.5 Battery state of charge algorithms	19
2.5.1 Coulomb counting	19

2.5.2	Kalman filter methods	20
2.5.3	Artificial neural networks method	22
2.5.4	Other methods and summary	24
2.6	Battery state of health algorithms	25
2.6.1	Direct measurement	26
2.6.2	Model-based methodology	27
2.6.3	Degradation modelling	28
2.6.4	Data-driven methodology	31
2.6.5	Summary	33
2.7	Prognostics of batteries	34
2.8	State estimation for battery systems	36
2.9	Thesis objectives	37
3	Experimental setup	38
3.1	Introduction	38
3.2	Willenhall Energy Storage System (WESS)	38
3.3	Other batteries used to investigate the algorithms	43
3.3.1	NMC and LTO cells	43
3.3.2	GS Yuasa rack	43
3.3.3	GS Yuasa battery system	46
3.4	Cell-level battery test equipment	47
3.5	Data profiles	47
3.5.1	A DFR data profile	47
3.5.2	WESS data profiles commonly used in chapters	50
3.5.3	OCV data profiles	52
4	SOC estimation of large-scale battery systems	55
4.1	Introduction	55
4.2	DEKF and DSPKF implementation on large-scale battery systems	56
4.2.1	Equations and battery models	56
4.2.2	From cell-level to system-level	62
4.3	Genetic algorithm	63
4.4	SOC estimation results	66
4.4.1	Cell-level results	66
4.4.2	Rack-level and a small battery system results	67
4.4.3	System-level results	69
4.5	Comparison of WESS efficiency calculation using DSPKF SOC and BMS SOC	71
4.5.1	Methodology	73
4.5.2	Efficiency results	76

4.5.3	Summary	77
4.6	Dealing with invalid data for BESS SOC estimation	77
4.6.1	Methodology	80
4.6.2	Results	82
4.6.3	Summary	84
4.7	Conclusion	85
5	Capacity and SOH estimation of large-scale battery systems	86
5.1	Introduction	86
5.2	TLS implementation on large-scale battery systems	88
5.2.1	TLS algorithm	88
5.2.2	TLS implementation from cell-level to system-level	89
5.3	TLS capacity estimation results	89
5.3.1	Rack-level capacity estimation results	90
5.3.2	System-level capacity estimation results	92
5.4	Data selection for system-level estimation	94
5.4.1	Methodology	95
5.4.2	Results and discussion	99
5.4.3	Summary	99
5.5	Comparison of capacity estimation using BMS SOC and DSPKF SOC	100
5.6	Battery capacity tracking using DSPKF and TLS	103
5.6.1	Capacity tracking of an NMC cell	104
5.6.2	Capacity tracking results of GS Yuasa battery energy storage system	105
5.7	BESS capacity estimation using power and SOC	108
5.7.1	Methodology	108
5.7.2	Results and discussion	109
5.7.3	Summary	113
5.8	Conclusion	116
6	Parameter estimation of large-scale battery systems	117
6.1	Introduction	117
6.2	Parameter estimation results from cell-level to system-level	118
6.2.1	Parameter estimation results: cell-level	118
6.2.2	Parameter estimation results: WESS	119
6.2.3	Parameter estimation results: GS Yuasa BESS	120
6.3	Voltage simulation to validate parameter estimation results	122
6.3.1	Simulation model	122
6.3.2	Simulation results	123

6.4	Conclusions	127
7	Conclusions & Further Work	129
	References	132
	Appendix	147
.1	Data links	147

List of Figures

1.1	Percentage of frequency out of deadband of GB National Grid from Jan. 2014 to Dec. 2020	2
2.1	Battery system state estimation flowchart	22
3.1	Photographs of (a) the WESS and (b) some racks inside the WESS.	41
3.2	Photographs of (a) a sample module inside the WESS and (b) a simple cell inside the WESS.	42
3.3	Battery system configuration of the WESS.	42
3.4	System diagram of the WESS.	42
3.5	Example WESS data on grafana: constant cycling.	43
3.6	WESS operation data in 3 days (a) system-level current, voltage, BMS SOC and power and (b) temperature of each string and system average temperature.	44
3.7	NMC cells: the CHAM cell on the left and the JGNE cell on the right.	45
3.8	Photographs of (a) GS Yuasa LIM50ER rack, (b) GS Yuasa LIM50E module and (c) GS Yuasa cell inside the modules.	45
3.9	Photograph of the ADEPT BESS.	47
3.10	Pictures of cell-level battery test equipment (a) EIS tester (b) Maccor battery tester and (c) an environmental chamber.	48
3.11	Dynamic frequency response (a) power vs. frequency envelope and (b) example of BESS power response.	48
3.12	Data profiles of the WESS (a) Constant cycling, (b) a mixed profile and (c) DFR.	52
3.13	LTO cell SOC estimation results with an OCV profile (a) cell voltage, (b) cell current and (c) SOC estimation results using Coulomb counting.	53
3.14	OCV-SOC test data profile of the WESS.	54

4.1	Equivalent circuit models of (a) first-order for the LTO cell and the WESS and (b) second-order for other batteries.	60
4.2	WESS OCV-SOC relationships: scaled from cell-level vs system-level.	63
4.3	The evolution of GA for DSPKF: (a) Q values at the first generation, (b) R values at the first generation, (c) Q values at the 10th generation and (d) R values at the 10th generation.	65
4.4	The evolution of GA for DSPKF: all generations together (a) Q values and (b) R values.	66
4.5	LTO cell SOC estimation results using the OCV data profile.	67
4.6	LTO cell SOC estimation results with an EFR low profile (a) cell voltage, (b) cell current and (c) SOC estimation results.	68
4.7	GS Yuasa BESS short data profile (a) voltage and (b) current.	69
4.8	DSPKF SOC results of (a) a GS Yuasa rack and (b) a GS Yuasa battery system.	69
4.9	WESS DSPKF SOC estimation results of (a) constant cycling, (b) mixed profile and (c) dynamic frequency response.	71
4.10	WESS DEKF SOC estimation results of (a) constant cycling, (b) mixed profile and (c) dynamic frequency response.	72
4.11	WESS DSPKF SOC estimation results of using (a) an ECM with 2-RC branches and (b) system-level OCV-SOC relationship.	72
4.12	WESS tests for round trip efficiency calculations (a) test 1 and (b) test 2.	75
4.13	Battery RTE against C-rate and DoD, using (a) DSPKF SOC and (b) BMS SOC.	78
4.14	Battery RTE against C-rate and SOC, using (a) DSPKF SOC and (b) BMS SOC.	78
4.15	Inverter import efficiency against C-rate and DoD, using (a) DSPKF SOC and (b) BMS SOC.	78
4.16	Inverter import efficiency against C-rate and SOC, using (a) DSPKF SOC and (b) BMS SOC.	79
4.17	Inverter export efficiency against C-rate and DoD, using (a) DSPKF SOC and (b) BMS SOC.	79
4.18	Inverter export efficiency against C-rate and SOC, using (a) DSPKF SOC and (b) BMS SOC.	79
4.19	System RTE against C-rate and DoD, using (a) DSPKF SOC and (b) BMS SOC.	80
4.20	System RTE against C-rate and SOC, using (a) DSPKF SOC and (b) BMS SOC.	80
4.21	WESS operation data profile for investigating invalid data.	82

4.22	SOC estimation results affected by invalid data (a) DEKF SOC and (b) DSPKF SOC.	83
4.23	SOC estimation results after using previous data during invalid data periods (a) DEKF SOC and (b) DSPKF SOC. . . .	83
4.24	DEKF invalid data results with other methods (a) pause the algorithm and (b) curve fitting.	83
5.1	Degradation of the CHAM cell (a) degradation shown as discharge capacity and (b) degradation shown as nominal capacity.	87
5.2	Yuasa rack data profile for capacity estimation (a) voltage, (b) current and (c) SOC.	90
5.3	Capacity estimation results of a GS Yuasa NMC battery rack.	91
5.4	Capacity estimation results of (a) constant cycling (~ 6.5 hours), (b) mixed profile (~ 9 hours) and (c) dynamic frequency response (~ 7 hours). The red dotted lines show $\pm 1\%$ error around the 1600 Ah assumed capacity.	94
5.5	A WESS 6-hour data profile for investigating the value of m and data length.	95
5.6	How the value of m and data length affect capacity estimation results (a) relationship between m and capacity estimation results and (b) Convergence time of the TLS algorithm.	96
5.7	Diagram of data-selection for BESS capacity estimation	97
5.8	Capacity estimation result comparison using a whole year data (a) use raw data, (b) only deal with invalid data and (c) with data-selection techniques.	98
5.9	Investigate the effects of SOC variation using data of a year. .	100
5.10	Capacity results of one year using (a) BMS SOC and (b) DEKF SOC.	101
5.11	Capacity tracking using capacity correction technique over one year of data.	103
5.12	Capacity tracking results of a JGNE NMC cell (a) tracking by the capacity correction algorithm and (b) tracking by the TLS algorithm.	105
5.13	3-year operating data of the GS Yuasa BESS.	106
5.14	Capacity results of 3 years of GS Yuasa BESS using (a) DSPKF SOC and (b) BMS SOC.	107
5.15	Capacity estimation using power and SOC of constant cycling.	109
5.16	WESS data at 1C in Oct. 2019 (a) power and current, (b) power and SOC and (C) power and dc-link power.	110
5.17	Capacity results of one year using (a) power and BMS SOC and (b) power and DSPKF SOC.	111

5.18	Capacity estimation using dc-link power and DSPKF SOC. . .	112
5.19	Capacity results of 2019 (a) using power and DSPKF SOC directly and (b) assuming only 22 inverters out of 24 worked in the whole year.	113
5.20	Considering inverter efficiency using one year data of 2018 (a) using power and DSPKF SOC directly and (b) assuming the inverter efficiency is fixed at 94%.	114
5.21	Considering inverter efficiency using the relationship between efficiency and power, capacity estimation results of 2018 (a) the relationship between inverter efficiency and power, (b) using the mapping and (c) using the mapping with a higher criterion of SOC variation.	115
6.1	LTO cell parameter estimation results of the OCV profile (a) initialise with a value much larger than the experimental value and (b) initialise with value much smaller than the experimental value.	119
6.2	LTO cell parameter estimation results of the EFR low profile (a) initialise with a value much larger than the experimental value and (b) initialise with value much smaller than the experimental value.	120
6.3	NMC cell R_s tracking (a) of the whole battery life and (b) of the whole battery life at fixed SOC.	121
6.4	EIS results of (a) a new JGNE NMC cell and (b) a JGNE NMC cell that reached EOL.	121
6.5	WESS parameter estimation with constant cycling (a) initialise with a value much larger than the calculated value and (b) initialise with value much smaller than the calculated value.	122
6.6	WESS parameter estimation with another profile (a) DSPKF and BMS SOC estimations of this profile, (b) initialise with a value much larger than the calculated value and (c) initialise with value much smaller than the calculated value.	123
6.7	WESS operation data with longer operation time	124
6.8	GS Yuasa BESS R_s tracking (a) of the 3 year operation and (b) of the 3 year operation at fixed SOC.	124
6.9	Voltage simulation results of an LTO cell from data profiles (a) OCV and (b) EFR low.	125
6.10	Voltage simulation results of the JGNE cell.	126
6.11	Voltage simulation results of an WESS with different profiles, using DSPKF SOC and BMS SOC (a) constant cycling, (b) mixed profile and (c) dynamic frequency response.	128

7.1	Battery system state estimation flowchart	130
-----	-----------------------------------------------------	-----

List of Tables

2.1	Comparison of different battery chemistries	16
2.2	Mandatory and firm frequency response services	16
2.3	Advantages and disadvantages of different battery SOC algorithms.	25
2.4	Summary of data-driven SOH algorithms	34
3.1	WESS specifications	40
3.2	Cell specifications	46
3.3	Maccor S4000 specifications	49
3.4	BioLogic SP-300 specifications	50
4.1	Multi-scale DSPKF implementation	57
4.2	DEKF implementation	59
4.3	GA settings	63
5.1	WESS Actual capacity calculations in May 2018	92
5.2	WESS Actual capacity calculations in Oct. 2019	93
5.3	WESS Actual capacity calculations in May 2021	93

Nomenclature

ABS Absolute value.

ANN Artificial neural networks.

AWTLS Approximate weighted total least squares.

BESS Battery energy storage system.

BMS Battery management system.

CCCV Constant-current, constant-voltage.

CHAM ShenZhen Cham Battery Technology Co.,Ltd.

DC Dynamic containment.

DEAP Distributed Evolutionary Algorithm in Python.

DEKF Dual extended Kalman filter.

DFR Dynamic frequency response.

DM Dynamic moderation.

DoD Depth of discharge.

DR Dynamic regulation.

DSPKF Dual Sigma point Kalman filter.

DTV Differential thermal voltammetry.

ECM Equivalent circuit model.

EFR Enhanced Frequency Response.

EIS Electrochemical Impedance Spectroscopy.

EOL End of life.

FFR Firm Frequency Response.

GA Genetic algorithm.

ICA Incremental capacity analysis.

IMMPF Interacting multiple model particle filter.

KF Kalman filter.

LFP Lithium iron phosphate.

Li-ion Lithium-ion.

LTO Lithium titanate oxide.

MAE Mean average error.

NCA Lithium nickel cobalt aluminium oxide.

NMC Lithium-ion Nickel, Manganese and Cobalt.

OCV Open-circuit-voltage.

PHM Prognostics and health management.

PSO Particle swarm optimisation.

RMSE Root mean square error.

RMU Rack management unit.

RNN Recurrent neural networks.

RTE Round trip efficiency.

RUL Remaining useful life.

RVM Relevance vector machine.

SOC State of charge.

SOH State of health.

SPKF Sigma point Kalman filter.

STD Standard deviation.

SVM Support vector machines.

TLS Total least squares.

WESS Willenhall Energy Storage System.

WTLS weighted total least squares.

List of Symbols

Ah Ampere hour.

C C-rate.

dV Derivative of voltage.

E Expectations,energy.

η efficiency.

H Hour.

HC High current.

I Current.

K The gain in the capacity correction technique.

L Kalman gains.

m size of data data segments in the TLS algorithm.

P Power.

Q Process noise.

R Sensor noise,resistance.

S second.

τ time constant.

V Voltage.

W Watt.

Chapter 1

Introduction

1.1 Background & Motivation

Global warming and pollution caused by burning fossil fuels is widely recognised as an imminent threat to the planet[1]. Renewable energy sources like wind and solar power can help to mitigate these problems, but their variability of generation over short time durations can cause instabilities in voltage and frequency of electricity networks[2]. The amount of power generated from these renewable sources depends on natural conditions, where generation exceeds demand, reliable methods are needed to store this excess energy. Conversely, where demand exceeds supply, energy storage may be used to provide support and stability to the grid whilst additional generation capacity becomes available.

Figure 1.1 shows the percentage of frequency measurements (sampled at 1Hz) of the GB's National Grid that out of deadband from Jan. 2014 to Dec. 2020. The frequency of the GB's National Grid should be maintained close to 50 Hz and the deadband shown here is defined as frequencies larger than 49.95 Hz or smaller than 50.05 Hz. Any frequency variations that end up outside this frequency range require frequency response services to correct the balance between supply and demand. These services traditionally either increase the power or decrease the power from a generator depending on the deviation of frequency from 50Hz over a short time scale (1 second). It can

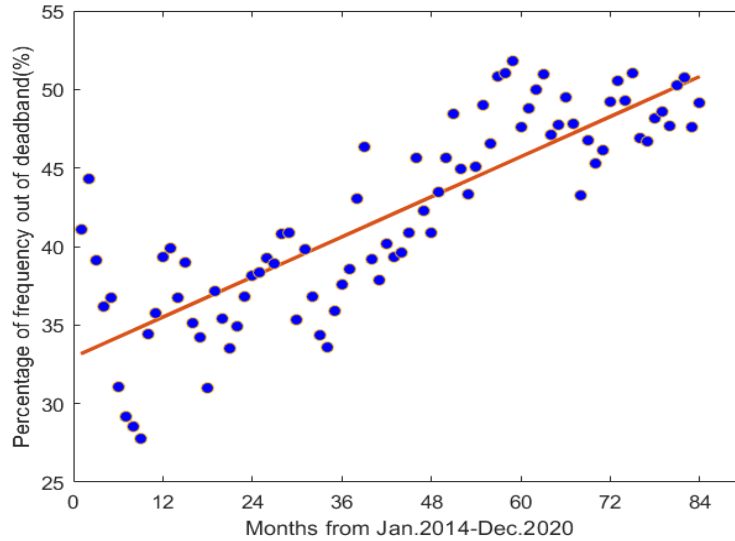


Figure 1.1: Percentage of frequency out of deadband of GB National Grid from Jan. 2014 to Dec. 2020

be seen that the percentage of frequencies that are outside of the deadband is increasing. Therefore, it can be argued that there is increased instability on the GB National Grid and these problems are likely to be replicated in other parts of the world since the penetration of renewable energy is increasing globally. To help with balancing, energy storage systems (ESS) are viewed as a good solution as they can both import power (effectively decreasing supply or increasing demand) and export power (effectively increasing supply or decreasing demand).

Large-scale battery energy storage systems (BESSs) have recently emerged as a popular ESS technology to provide a variety of grid support services [3]. This is due to their fast response, relatively easy scalability and recently decreasing costs. A range of GB National Grid frequency response services such as firm frequency response and fast reserve can be achieved by BESSs [4], they can also be used to achieve price arbitrage and balancing services. The recent advances in battery chemistry technologies have improved the performance of BESS in terms of higher volumetric energy capacities, better round-trip efficiencies, and longer lifetime. To make effective use of these

advances, to successfully provide grid support and maximise the return on investment for battery owners, advanced battery management systems (BMS) need to be developed.

State of charge (SOC) and state of health (SOH) are the two essential indicators that need to be estimated by the BMS. Capacity, which represents the maximum electrical charge that a battery can store presently, is directly related to these two indicators. SOH is the quotient of the actual capacity and the nominal capacity, whereas, SOC is the percentage of charge held by the battery presently with respect to the actual capacity. The capacity of a battery reduces over time and its rate of degradation is predominantly dependant upon the type of usage. The accuracy of SOC [5] and SOH [6] estimations at the cell-level have improved significantly over recent years from numerous researchers. However, for large-scale battery systems, the accurate estimation of SOC and SOH is a relatively new topic.

The accurate estimation of a BESS's capacity and SOC are critical for its operation. Batteries have limited lifespans; when the criterion of the end of life, often around 70% or 80% of nominal capacity, is reached, the battery will no longer serve the need of the application. Moreover, as the efficiency of the battery decreases, there is a higher risk of permanent failure of cells within the battery system. As providing services reduces the SOH, the service must be financially beneficial when taking into consideration the loss of capacity incurred. Accurate SOH prediction allows for an estimation of the cost in terms of battery degradation of a service to be compared against the profit earned by performing the service. In this way, it is possible to optimise the control and availability of the services provided, to generate maximum profit whilst causing minimum degradation of the BESS. It is also important to be able to predict the capability of the system to store energy going forward, thus being able to avoid services that require more energy than the BESS can provide. The necessities for accurate SOC estimation are more straightforward: the owner of a BESS needs to know how much energy is currently stored to provide grid services and actively manage the SOC to remain within the service requirements.

1.2 Thesis Contributions

This thesis presents the challenges of implementing cell-level state estimation techniques on large-scale BESSs and introduces novel methods for their successful realisation. For the first time, experimental results on a BESS with over 20k battery cells are presented demonstrating SOC, SOH and parameter-estimations. The implementation of the DSPKF and TLS, as well as SOC and capacity estimation results have been published in a journal [7]. Figure 7.1 provides an overview of how the various methods interact, with the numbers in each box indicating the relevant sections in this thesis. All data from the BESS is obtained at the highest level in the system as compared to interfacing at lower levels that would produce faster sampled and consistent data. This is representative of asset owner access to data in a real-world system and demonstrates the potential for the methodologies presented in this work to process data both locally and remotely, for example in cloud based systems as used by aggregators.

BESS SOC estimation

This chapter first demonstrates the implementations of DSPKF and DEKF on a BESS for SOC estimation, and proposes using a genetic algorithm (GA) to solve the parameter selection problem. The results show that the DSPKF and the BMS SOC are a good match with the GA providing acceptable solutions. An analysis between using a system-level measured OCV-SOC and a scaled cell-level OCV-SOC relation is presented. Methods for overcoming the invalid data problem of a BESS for SOC estimation are introduced. Using system round-trip efficiency (RTE) measurements, validation on the accuracy of the methodology is evidenced.

BESS capacity and SOH estimation

In this chapter, for online system capacity estimation, a total least-squares (TLS) methodology is demonstrated for the first time on a large-scale BESS that discovers the need for data selection and data cleansing. System-level

degradation experimental results are also presented to validate the system-level capacity estimation results. In addition to system current, the TLS algorithm requires an SOC estimation input, to demonstrate the accuracy of the DSPKF algorithm this is used and compared against the existing BMS SOC. Then, a method is proposed to improve SOC estimation and capacity accuracy as the BESS degrades. The BESS used in the work has not significantly degraded, therefore capacity tracking using the algorithms presented on a smaller Lithium-ion Nickel, Manganese and Cobalt (NMC) battery system is demonstrated and the results are promising. Finally, it is demonstrated that where only grid-side power and SOC is known, for example in an aggregator scenario, the TLS algorithm can be used but the analysis in this thesis shows, for the first time, that a mapping of efficiency of the inverter against power is required for accurate results.

Estimation of the series resistor in the battery equivalent circuit model of a BESS

The DSPKF algorithm holds an estimation for the series resistor in the battery equivalent circuit model (ECM). This chapter uses experimental results to analyse how effective this is with and without the novel implementation methods presented in the earlier chapters. The estimated values are used in a simulated ECM circuit to calculate terminal voltage and compared against systems measured values. Again, to demonstrate using a system that has degraded, the experiment is repeated on the smaller NMC battery system and an NMC cell that has reached the end of life (EOL).

Chapter 2

Literature Review

In this chapter, battery chemistries, battery system grid services, battery system optimisation and battery SOC and SOH algorithms are reviewed from the literature.

2.1 Definitions

Various terminologies exist for batteries to characterise their performance. The most commonly used terms in the literature are summarised here.

Ampere-hour (Ah) capacity. Ah charge capacity is often used for describing the total amount of releasable charge stored in a battery under predefined conditions. The rated Ah charge capacity is the battery's nominal discharge capacity (manufacturer's standard conditions).

C-rate. This is a measure of the rate at which a fully charged battery uses one hour to discharge its nominal Ah capacity under standard conditions. For example, a 20Ah lithium-titanate battery will require a current of 20A to discharge the battery in 1 hour (1C) fully, a current rate of 2C for this battery would mean using 40 A to discharge it. C-rate is also used for charging in the same manner.

Specific Energy. This is used to quantify the amount of energy a battery can store per unit mass, expressed in Wh/kg.

Energy Density. This is the nominal battery energy stored per unit

volume, expressed in Wh/l.

Internal Resistance. This is the ohmic voltage drop in a battery under operation, which is different for charging and discharging and may vary with respect to the battery's operating conditions and age.

Calendar Life. This terminology refers to the period that a battery can be stored before it reaches the end of life. It can be seen as a gradual degradation of the battery when the battery is inactive or with minimal use.

Cycling Life. This is the number of full cycles a battery can achieve before the end of life.

Self-Discharge. This is the reduction of a battery's stored charge without any external connections to the battery's terminals.

State-of-Charge (SOC). This is the remaining quantity of releasable charge with respect to the maximum available charge capacity.

Depth-of-Discharge (DoD). DoD is to indicate the percentage of the total Ah capacity that has been removed from the battery, which is the complement of SOC.

State-of-Health (SOH). SOH is the condition of a battery, with respect to ideal conditions (100%) and it is normally defined as actual capacity divided by nominal capacity.

End-of-life (EOL). This is the point that a battery needs to be replaced, and it normally happens when a battery has 70% or 80% of its original capacity. However, it is application-specific, batteries in a BESS could still work with lower than 70% SOH.

Float charge voltage. The voltage where the battery is maintained at 100% SOC after charging to compensate self-discharge of the battery.

Open-circuit-voltage (OCV). The voltage between battery terminals without a load. It increases with state of charge.

Electrochemical Impedance Spectroscopy (EIS). Battery electrochemical impedance is normally measured by applying small AC potentials over a range of frequencies to the cell, obtaining current responses.

2.2 Battery chemistries and the market

Battery chemistries are the heart of battery performance and utilisation. In the history of battery development, there have been several key developments. From lead-acid to lithium-ion, electrochemistry has been leading the development of the entire battery industry. There are studies for new battery materials that can overcome the limitations of Li-ion batteries, i.e., the energy density of lithium-ion batteries is approaching the boundaries[8].

2.2.1 Lead-acid battery

This kind of battery has a long history as the oldest rechargeable battery. The negative active material is metallic lead, and the positive active material is lead oxide when it is fully charged. Both the negative and positive active materials become $PbSO_4$ when fully discharged. The electrolyte is sulphuric acid (H_2SO_4), with a concentration of approximately 33.5%. CC-CV charging regime is commonly used: at the beginning, the constant current is used of typically $C/2$ or $C/5$ until the voltage reaches the float charge voltage, after which the voltage is held, and the battery is charged with a gradually smaller current. The open-circuit voltage at full charge is 2.1 V, and the open-circuit voltage at full discharge is 1.95 V [9].

Advantages: Low cost and simplicity to manufacture, low self-discharge (temperature dependent), high voltage per cell, large specific power and capable of discharging with large currents.

Disadvantages: Heavy, poor low-temperature characteristics, low specific and energy densities, slow charge, short cycle life, repeated deep-cycling can reduce battery life significantly and transportation restrictions.

2.2.2 Conventional lithium-ion batteries

Lithium is the lightest metal, but it can provide the largest specific energy. Lithium-metal batteries were first invented with very high energy densities but were not safe enough because of the unavoidable dendrites generated on the anode during cycling that could cause electrical short-circuiting. To

address the instability issues of such batteries, lithium-ion batteries were invented as a replacement [10].

Lithium-ion batteries were used in portable electronics first because of the high energy density but now are also very popular in electric vehicles and energy storage systems. It has a high energy density and power density. Conventional lithium-ion batteries use graphite anode and lithium-metal-oxide cathode, separated by a nanoporous separator, and the electrolyte is a lithium salt solution. Lithium ions are charge carriers, and both the anode and the cathode are the hosts of lithium ions. The two electrodes allow lithium ions to be transported to the other electrode and there is no breaking or re-formation of chemical bonds. This helps to avoid the formation of inter-phase surfaces (such as sulfation of the lead-acid electrodes) and hence makes the lifespan of lithium-ion batteries longer. During discharge, lithium ions flow from the anode (negative electrode) to the cathode (positive electrode), and the direction is opposite for the charging process [11].

A solid-electrolyte interface (SEI) is formed on the anode and electrolyte boundary. Initially, SEI formation protects the electrode against solvent decomposition, but over time the SEI layer is thicker, which leads to a gradual capacity fade [12]. Therefore, SEI is essential for the study of battery SOH.

To charge a lithium-ion battery, CC-CV regime is usually undertaken, like for a lead-acid battery. However, the OCV curve when discharging is sometimes quite flat within the range of 20% to 80% SOC, which makes SOC estimation methods that rely on the OCV-SOC relationship difficult to implement. The floating voltages of lithium-ion batteries depend on the positive active material.

By comparing the different Li-ion chemistries, lithium nickel manganese cobalt oxide (NMC) batteries are normally known to have the best overall performance considering cost, specific energy, specific power, life span and safety. This kind of battery is the most popular in the market nowadays thanks to its excellent specific energy, replacing the previously widely used lithium iron phosphate (LFP) cells. However, these kinds of batteries may suffer from low C-rate. Besides, it has a shorter lifespan, and is less safe than the LFP ones.

Ageing can occur in cathode, anode and electrolyte. There are some fault mechanisms of lithium-based batteries:

Overcharging: this leads to thermal decomposition and may be worse as a fire is an eventuality. Over discharging: short-circuiting can happen, and lead to permanent capacity loss. Overheating: SEI is temperature sensitive and can decompose above 110 °C. This may be due to internal problems such as overcharging and can also lead to fires. Short-circuiting and physical abuse are dangerous.

Advantages: High energy and power density; long cycle life; high cell voltage; fast charge capable; high discharge rates; low self-discharge rate (temperature dependent).

Disadvantages: The relatively high price needs to be under consideration; safety issues such as over-charging/ over-discharging; complex charging requirements; the need for protection/management system; SOC measurements are harder than the Lead-acid ones.

2.2.3 Lithium-titanate battery

This kind of battery is normally only used in Japanese products. A lithium titanate battery is modified from the conventional lithium-ion batteries, using lithium-titanate nanocrystals on the surface of the anode to replace graphite, providing more active surface area [13]. This allows electrons to enter and leave anodes quickly (for fast charging). The cathode and electrolyte materials remain the same as conventional lithium-ion batteries. The equation below shows one of the chemical equations of a lithium-titanate battery.



Advantages: Fast charging is possible and the charging current can be larger than conventional lithium-ion batteries; safer than conventional lithium-ion ones; excellent low-temperature performance on both low-temperature capacity and health effects; no SEI film formation and this contributes to the improvement of safety over conventional Lithium-ion batteries; thermal stability at high temperature is also better than other Li-ion counterparts; the

long lifespan (can be over 10000 cycles) makes this kind of battery promising candidate for grid-level energy storage.

Disadvantages: Low inherent voltage (2.4V); which is much smaller than conventional lithium-ion batteries (around 3.7V); most importantly, it is expensive; it is also limited by low specific energy.

2.2.4 Sodium-ion battery

Sodium exists more widely on earth than lithium, which makes sodium-ion batteries simple to manufacture and cheap. Therefore, scientists have been trying to replace lithium with sodium in batteries for a long time [14]. Li-ion batteries have been preferred because of the discovery of using carbon as the anode in the 1990's to achieve large capacity [15]. However, in 2000, a new anode material of sodium-ion batteries found by Stevens and Dahn could match the specific capacity of the Li-ion batteries, making sodium-ion batteries back to the competition.

The low electrochemical potential of sodium makes sodium-ion batteries particularly attractive for grid-connected BESSs. Being abundant and cheap are also advantages of using sodium-ion batteries in stationary large-scale BESSs [14].

Currently, the main challenge of Sodium-ion batteries is the low effectiveness of the electrode materials [16].

Advantages: Cheap, safe, especially suitable for large-scale BESSs.

Challenges: Electrode materials, ionic size of sodium ions, the conductivity of active materials [17].

2.2.5 Sodium sulphur battery

Sodium sulphur batteries were first introduced in 1968 [18], using two highly active materials, sodium and sulphur, separated by a solid electrolyte. This kind of battery has to be operated in temperatures over 300 °C [19]. Sodium sulphur battery performs well in terms of cycling life, round-trip efficiency, and energy density, making it suitable for stationary energy storage. One of the disadvantages is that sodium is hazardous [20]. To date, the cost

reduction of sodium sulphur batteries has not been significant, compared with other types of batteries like lithium-ion.

Advantages: long Cycle life, high round-trip efficiency, large energy density.

Challenges: must be operated at high temperature, relatively low power density, relatively high cost.

2.2.6 Redox Flow battery

Developed in 1970s, a redox flow battery (RFB) runs according to reversible oxidation and reduction. It consists of separate energy and power modules [19]. An ion-exchange membrane is used to separate the positive and negative half-cells and energy conversion is achieved by pumping the electrolyte. Among various RFBs, vanadium redox flow battery (VRFB) is popular because of the large availability, high energy efficiency, low capital cost, long cycle life and low toxicity [21]. In general, RFBs have the following advantages: suitable for large-scale energy storage [22], power and energy are not coupled, long service life and the safety [23]. As of disadvantages, RFBs need breakthrough on fundamental materials and they are generally not competitive in terms of the cost.

Advantages: long cycle life, safety, suitable for large-scale energy storage.

Challenges: Cost reduction, key materials.

2.2.7 Lithium sulphur battery

In this kind of battery, sulphur is used replacing currently used cathode materials, with a high theoretical specific capacity, and the negative electrode is lithium [8]. These batteries are attractive in recent years because the energy density and specific capacity could be as high as 2600 Wh/kg and 1675 mAh/g [24], which are much higher than a conventional Li-ion battery.

Advantages: Very high energy density and specific capacity; light because of using sulphur; the cost can be lower than lithium-ion batteries because of the use of sulphur.

Challenges: the utilisation of the materials to reach the theoretical capacity [24]; The volumetric instability during cycling; polysulfide dissolution and shuttling that could lead to current leakage, and affect cycle-ability and columbic efficiency[25].

2.2.8 Lithium-air battery

This kind of battery uses oxidation of lithium at the anode and reduction of lithium at the cathode to induce a current flow [26]. Metal-air batteries are attractive because of the potential high energy density, compared to all other battery chemistries. The energy density of lithium-air batteries is very attractive because it can reach 1700 Wh/kg which is very close to the energy density of gasoline. The practical energy density of Li-S is 370 Wh/kg, and the energy density is rarely above 250 Wh/kg for current Li-ion batteries [27].

Advantages: Very high energy density; high specific energy.

Challenges: To breathe oxygen from ambient environment [28], power density is currently very low; Low rate capability; Low round-trip energy efficiency; Short life [29].

2.2.9 Solid state battery

An all-solid-state battery has both solid electrodes and solid electrolytes. It has been proposed and developed to solve the problems of lithium-ion batteries, especially the safety issues [30]. Recently in [31], authors proposed a design of an all-solid-state battery to achieve excellent energy density, cycle life and overcome the Coulombic efficiency challenge.

Advantages: Both high energy density and power density; no problems with electrolyte leakage; long lifespan; performance is not affected by temperature; high energy to weight ratio; may be ideal for use in electric vehicles.

Challenges: Coulombic efficiency; The materials of essential electrolyte; the creation of stable interfaces between battery components[32].

2.2.10 Battery market

The battery market is growing fast. From portable devices, electric cars, energy storage systems, to other industries like aircraft. The overall dominating chemistry in the market is lithium-ion, where NMC and LFP are the most popular ones, and battery manufacturers mainly use different raw material ratios. In terms of manufactures, east Asian ones are dominating. Chinese manufacturers such as CATL (the largest producer of lithium-ion batteries for electric vehicles) and BYD have significantly increased in the number of products they produce and could be more critical in the lithium-ion battery market in the near future. Korean and Japanese manufacturers such as LG Chem, Samsung, Panasonic and Toshiba are also popular in the world. Manufacturers have been cooperating with automotive and energy storage companies closely. For example, the relationships between Panasonic and Tesla [33], CATL and BMW [34].

2.2.11 Summary

Lithium-ion batteries are currently dominating the market, because they have the best overall performance. NMC and LFP are currently the most common chemistries commercially. However, several new chemistries have exhibited great potential at the research stage, including Lithium-sulfur, Lithium-air and all-solid-state batteries, to overcome the disadvantages of Lithium-ion batteries. Besides, Sodium-ion batteries have the potential to replace the Li-ion ones, especially for large-scale BESSs. Table 2.1 compares different battery chemistries. The battery market is still expanding sharply and it may play an essential part in the urgent need to control global warming.

2.3 National Grid frequency response services

There is a range of balancing services that the National Grid provides to maintain the quality and security of the GB electricity supply[35], and they are required to maintain the frequency at 50Hz $\pm 1\%$, i.e., sufficient generation

and/or demand for electricity supply. The most common balancing services of the National Grid are included in this section.

Dynamic and non-dynamic (static) frequency responses are the two main categories of frequency response. Static frequency response is usually a discrete triggered service at a defined frequency deviation. For dynamic frequency response (DFR), the energy changes in line with system frequency so it is a continuous service.

Mandatory frequency response

Mandatory frequency response are held automatically and quickly, to keep frequency within operational limits. Traditional generators have to be able to provide mandatory frequency response. This kind of response is an automatic change in response to a frequency change. This kind of response in the National Grid includes three response services, and they respond to an increase or a decrease in demand, as shown in table 2.2.

Firm frequency response (FFR)

Firm frequency response has more providers than mandatory frequency response, and it is procured through a competitive tender process (i.e., to invite bids for a project). FFR provides both dynamic and non-dynamic responses to changes in frequency. FFR service is a commitment from a provider to either operate at a pre-specified level of power (static) or operate in a frequency sensitive mode (dynamic) for a set period. The detailed services are the same as the mandatory frequency response as shown in table 2.2.

Enhanced frequency response (EFR)

This service can change the active power in proportion based on a frequency deviation. The response time is much shorter than the responses mentioned in the mandatory frequency response. Although this service has been withdrawn, one of the data profiles shown in this work is generated by doing this service. Besides, the underlying principle of EFR (i.e. power demand in response to frequency deviation), is still the basis of current frequency response services.

Table 2.1: Comparison of different battery chemistries

Chemistry	Main advantages	Main disadvantages/challenges	Stage of development for BESS
Lead-acid	Low cost, capable of large discharge currents	Heavy, short cycle life, slow charge	deployed commercially
Conventional Li-ion	Best overall performance commercially	Safety issues, energy density is reaching the limit	deployed commercially
LTO	Safety, excellent cycle life and low temperature performance	Expensive, low voltage	deployed commercially
Sodium ion	Cheap, safe, candidate for large-scale BESSs	Electrode materials, conductivity of materials	deployed commercially
Sodium sulphur	long Cycle life, large energy density	No significant cost reduction	deployed commercially
Redox flow	long Cycle life, safety	Cost reduction, key materials	deployed commercially
Lithium sulphur	very high energy density, low cost	Materials, volumetric instability	developmental
Lithium-air	Very high energy density, high specific energy	Low power density, short life	developmental
Solid state	High energy density, safety, lifespan	Coulombic efficiency, materials	developmental

Table 2.2: Mandatory and firm frequency response services

	Response time	Sustainable time
Primary response	10 s	20 s
Secondary response	30 s	30 min
High frequency response	10 s	indefinitely

Dynamic containment, dynamic moderation and dynamic regulation

These 3 services are all classified as DFR. Dynamic containment (DC) is to operate after a significant deviation in frequency, which is fast-acting. Dynamic moderation (DM) is designed to deal with sudden large imbalances of frequency. Both DC and DM operate in a post-fault way. Dynamic regulation (DR) is a pre-fault service, which aims to correct continuous but small frequency deviations slowly.

2.4 Battery systems and their management of optimisation

Battery systems have the potential to take the dominant position of pumped hydroelectric energy storage. Before 2014, sodium sulphur batteries played a crucial role in the electric power market, but lithium-ion batteries and redox flow batteries, especially the former have been drawing significant attention in recent years. The reason is that they can achieve better performance and at lower costs than the sodium sulphur ones [19]. Battery systems cannot solve all the energy problems, but they can provide improvements in grid reliability [36].

The optimisation of a battery system includes minimising the degradation and maximising stacking revenue. A BESS can be run for arbitrage (store electricity when the price is lower and sell it when the price is higher). However, the necessity of trade needs to be evaluated. The system has to be replaced when it meets the end of life or is not able to meet the criteria of the grid, so degradation is a kind of cost. Therefore, the comparison between the degradation cost and the revenue needs to be done. The prognostics algorithms for minimising degradation and optimisation algorithms for maximising revenue are essential for BESS.

In 2008, Armand et al. [37] suggested batteries could be the best sustainable way for increasing electricity demand and predicted future possible advanced battery chemistries. They also described the importance of nan-

otechnology and organic-based technology (electrodes made from biomass) for batteries development to solve environmental problems.

New battery chemistries have been investigated for battery systems due to the limitations of the price, availability and safety issues of Li. Na^+ , K^+ , Mg^{2+} , Zn^{2+} in electrolytes have been reported as alternatives because they are cheaper, safer and eco-friendly. Su et al. [38] proposed a design of potassium-ion batteries that have a range of advantages: low cost, non-toxicity, high capacity, and long cycle life, making them attractive for large-scale BESSs.

Redox-flow batteries (RFBs) are also good choices because of the independence between power and energy capacity, very long cycle life, safety and good transient behaviour. However, commercial RFBs normally have low energy density and poor stability. Li et al. [39] reported a novel vanadium redox flow battery with about 70% increase in energy capacity and excellent stability between -5 to 50 °C (Li-ion batteries' performance is often affected by temperature).

Second life usage of electric vehicle batteries could lead to a significant decrease in the cost of grid-level energy storage. EV Li-Ion battery packs will remain approximately 80 % of their SOH after being removed (if an EV battery has degraded a lot it cannot support the vehicle for a long enough trip), which would make a second use as stationary energy storage possible. Authors in [40] assumed that EV batteries' first use could be for 8 years, and then they could be reused for another 10 years. They analysed the potential environmental costs and advantages of battery second life in ESS. In addition, they emphasised the importance of SOH in second life for energy efficiency.

Reniers et al. [41] proposed accurate battery degradation models for optimal control of grid-connected Li-ion batteries, to predict battery degradation, thereby performing price arbitrage. The result of their optimisation algorithms is the optimal current (for both charging and discharging) at each point in time for each battery model. The critical conclusion in this work is that a greater battery capacity can be used by implementing more accurate battery models. This work shows good results, and it could be useful for future research, but it is model-based rather than data-driven as in this

thesis.

There are a few studies in the literature that used optimisation algorithms to do battery-system optimisation. A simulated Annealing algorithm (a probabilistic technique for optimising functions of various variables) was used for minimising the cost of a hybrid energy system [42]. A Genetic algorithm (a global search method, discussed more in Chapter 4) was used in [43] to maximise the useful life of a lead-acid battery system.

2.5 Battery state of charge algorithms

State of charge (SOC) of Li-ion batteries cannot be measured directly and can only be estimated since it is affected by various factors such as current, temperature, charge/discharge history and SOH. Thus, the algorithms for estimating SOC are essential to make the results as reliable as possible, and estimating SOC is one of the main tasks of battery management systems (BMS). There is a range of SOC algorithms, and they are either direct or indirect. In this section, only popular methods are reviewed in detail.

2.5.1 Coulomb counting

Coulomb counting is the most often used method in industry and commercial applications to estimate SOC. The equation of calculating SOC is shown in (2.2)[44]. The change in SOC is calculated by accumulating the charge transferred in or out of the battery, therefore, the initial SOC must be available to estimate SOC in this method.

$$SOC(t_0 + \tau) = SOC(t_0) + \frac{1}{C_{rated}SOH} \int_{t_0}^{t_0+\tau} -Idt \quad (2.2)$$

where $SOC(t_0)$ is the initial SOC, C_{rated} the rated (nominal) capacity, τ the time duration of charge or discharge, and I is the input or output current. Note that in this thesis, the discharge current is defined as positive, which is in line with convention.

The advantage of Coulomb counting is its simplicity and that it is a direct

method, where the SOC and capacity (discussed later) can be estimated requiring only the measurement of the current [45]. However, it can be very inaccurate. There are losses during charging and discharging, and these, in addition to self-discharging, result in errors. The measurement of current is another problem since the current sensors can be affected by offset errors or noisy measurements, and these combined errors accumulate into increasingly large errors as time passes. The estimated SOC will diverge from the actual SOC, although a reset mechanism using the open-circuit voltage and SOC relationship (OCV-SOC relationship), discussed in more detail in section 4 can mitigate this but only under ideal conditions not necessarily witnessed by an online operational BESS.

2.5.2 Kalman filter methods

Kalman filter (KF) methods can provide very accurate indirect estimations of SOC. They compute a weighted average of the measured value and the predicted value by utilising a set of recursive equations to minimise the noise values [46]. The weighted average (Kalman gain) is calculated by placing heavier weights on more likely values according to the error covariances.

Minimising both the state and the error covariance is the heart of the solution in KF methods. Prediction and correction are the two main steps in KF: in the prediction step, the state of the system is estimated using the previous measurement, then in the correction step, the estimated state is updated with the measurement.

$$KG = \frac{E_{EST}}{E_{EST} + E_{MEA}} \quad (2.3)$$

where KG is the Kalman gain, E_{EST} the error in the estimate, and E_{MEA} is the error in the measurement which can be calculated according to the knowledge of sensor accuracy or set by experience. The Kalman gain is updated every iteration.

$$EST_t = EST_{t-1} + KG[MEA - EST_{t-1}] \quad (2.4)$$

where EST_t is the current estimate, EST_{t-1} the previous estimate and MEA is the measurement.

$$E_{EST_t} = [1 - KG](E_{EST_{t-1}}) \quad (2.5)$$

where E_{EST_t} is the new error in the estimate.

The main procedures for implementing a Kalman filter can also be summarised as three: the calculations of Kalman gain, the current estimate and the new error in the estimate, which are shown in equations 2.3, 2.4 and 2.5 respectively. A flowchart of KF implementation is shown in Figure 2.1.

Battery systems are nonlinear so a standard (non-extended) Kalman filter cannot be used. The Extended Kalman filter (EKF) was first proposed in [46], but the Sigma Point Kalman filter (SPKF) [47] is more advanced than EKF, and is seen as the state-of-art of KF algorithms. SPKF computes the covariance matrix by using the results of a number of function evaluations, which decrease the error of linearisation significantly. Moreover, SPKF can achieve higher accuracy with similar computational complexity to EKF. There are various sigma-point methods, and among them, the Central Difference Kalman Filter (CDKF) is chosen in this work because it is simpler to be implemented and has higher theoretical accuracy [48].

Dual Sigma Point Kalman filter (DSPKF) [49] and dual extended Kalman filter (DEKF) [50] can realise the estimation of both state and parameter values with two separate filters. The two filters in these methods are called state filter and weight filter respectively, and the weight filter is designed for equivalent circuit parameter estimation since the parameters vary slowly with time for a battery. Therefore, DSPKF is more accurate than a single SPKF that has fixed parameters. The two filters run in parallel, they adapt the parameters and the state respectively with some information exchange.

There is a range of studies that use KF methods to estimate SOC and capacity. In [46], a KF was first proposed for battery applications, the inputs include the current, voltage and temperature experienced by the cell, and the output is the SOC. The SOC is first predicted using a battery model then, the open-circuit voltage can be formulated according to the OCV-SOC

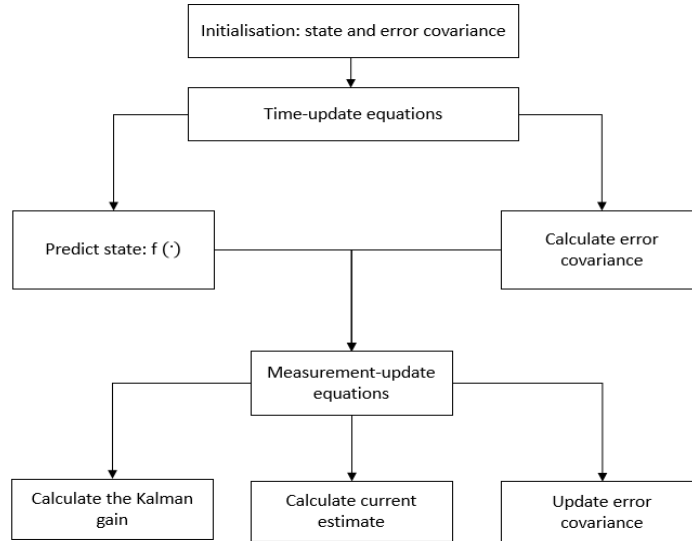


Figure 2.1: Battery system state estimation flowchart

relationship. Thereafter, the OCV is used to calculate the terminal voltage, which is compared with the measured voltage to correct the prediction. Zou et al.[51] proposed a novel combined SOC and SOH estimator, and in this work, SOC was estimated in real-time using a second-order EKF (two state variables), and SOH was updated offline using a fourth-order EKF. Authors in [52] proposed a multi-scale DEKF algorithm for lithium-ion batteries to significantly reduce the computational burden, based on that the parameters estimated in the weight filter do not change quickly.

KF methods are not complex and can be implemented with a systematic approach offering high accuracy and robustness against poor initialisation. The disadvantages are that they are sensitive to modelling accuracy; the battery operation environment should be in the zero-mean noise condition (Gaussian)[53].

2.5.3 Artificial neural networks method

Data-driven methodology has drawn significant attention recently, thanks to the rapid development of machine learning. A complicated but accurate model of a system can be trained first, using sufficient data, after which

the model is used to predict the required values, such as SOC and SOH in battery systems. These methods can be even more accurate than the Kalman filtering, including artificial neural network (ANN), support vector machine (SVM) etc. [19], but they require a significant amount of data and demand higher computation. They are frequently applied for the prediction of SOH and remaining useful life (RUL)[54].

Artificial neural networks (ANNs) are computing systems that are built like biological neural networks in animal brains. They can learn (progressively improve performance on) tasks from examples. Essentially, machines do not need to be task-specific programmed using ANNs. Artificial neurons are units or nodes in these systems. Signals (real numbers) are transmitted between artificial neurons. Non-linear functions of inputs are used to calculate the outputs of artificial neurons. Artificial neurons have a weight to adjust the learning process, affecting the strength of the signals between neurons. Artificial neurons are organised in layers and signals may traverse the layers multiple times from the first layer (input) to the last.

The backpropagation neural network [55] has an excellent ability of complex nonlinear mapping, which makes it a good choice for SOC estimation because the relationship between the input and SOC is nonlinear and complicated (can be affected by various factors). An artificial neural network that calculates battery SOC using historical data including voltage, current and the ambient temperature of a battery was proposed in [56]. In addition, classic SOC estimators like the KF family usually rely on battery models that require knowledge inside a battery, which can affect the SOC estimation results significantly. In comparison, ANNs can be utilised for all batteries, without the need of building an accurate model, providing training data. Besides, a neural network is capable of estimating SOC with an unknown initial SOC [56]. The drawback is that ANNs need a huge amount of data to analyse and the networks can be very complicated.

2.5.4 Other methods and summary

Coulomb Counting is simple to implement and often used to estimate SOC but normally not accurate enough for long-term usage. Therefore, indirect methods that could be more accurate and reliable are introduced to estimate SOC. Apart from KF methods and machine learning methods, there are also open-circuit voltage and Electro-chemical Impedance Spectroscopy (EIS) methods that are commonly used and relevant to the work conducted in this thesis.

Battery open-circuit voltage (OCV) that is the voltage when a battery reaches balance after sufficient resting time, is a function of SOC. This method measures a range of open-circuit voltages at different SOC values, forming a look-up table (OCV-SOC relationship)[57]. This method can be accurate but suffers from the long rest time [58], hysteresis between the charge and discharge voltage [59], and the difference between batteries that are even from the same manufactures. Despite the disadvantages of using this method alone, the OCV-SOC relationship is essential when it is used with a battery equivalent circuit model (ECM) in other methods like the KF methods introduced above (section 2.5.2).

EIS is also a frequently used indirect method, using the relationship between the variation of impedance and SOC [60], or combining with OCV to further reduce errors [61]. The drawback of this method is that it is not practical in most applications (a long time needed to take a measurement and it is difficult to be done online). However, the idea of using EIS and an appropriate model to calculate the impedance value is widely applied with KF methods [46, 49].

KF's performance depends on the accuracy of the models, whereas ANNs need sufficient training data. However, provided with these, the actual KF or ANN SOC estimator can hardly be ideal due to the different internal parameters in cells of the same type even if they are from the same manufacturer [56]. Thus, adaptability is essential for highly reliable SOC estimators, considering the variations mentioned above of parameters and temperature through the battery lifetime [62]. The advantages and disadvantages of different SOC

Table 2.3: Advantages and disadvantages of different battery SOC algorithms.

Method	Advantage	Disadvantage
Coulomb Counting	Simple and easy to implement	Relies heavily on the current sensor's precision, often suffers from accumulated errors, needs the knowledge of initial SOC.
Open circuit voltage [57, 63]	Simple, suitable for applications with small currents.	Not very good for lithium-ion batteries since they have a flat OCV-SOC curve, sensitive to the precision of the voltage sensor, time-consuming.
Kalman filter [46, 50, 64]	Closed loop, online and accurate, not difficult to implement. KF shows good convergence ability.	High requirement for the model accuracy, high computation complexity.
Neural network and fuzzy logic [56, 65]	Generic and have good non-linear mapping, no need for an accurate battery model.	Sensitive to the quantity and quality of battery data.

algorithms are shown in table 2.3.

Fusion methods that combine above-mentioned methods can further improve the accuracy of SOC estimation, with an increase in complexity. For example, a fusion method, which combines ANNs and EKF with an adaptive covariance matrix for the system noise has also been proposed and achieved excellent accuracy, but requires both model accuracy and high data quality [66]. For more SOC estimation algorithms and more details, see [5, 67]

2.6 Battery state of health algorithms

The decrease in SOH is described as the degradation of batteries. Both power fade and capacity fade (energy fade) are signs of batteries degradation. The increase of the internal resistance affects power fade because less power can be provided with an increase in resistance. With an increase in cycling times,

the capacity of the battery decreases so that the available energy is decreased. The SOH problem is not the same for different battery chemistries.

There are a few reasons for the degradation of batteries, such as material stress and fatigue, electrode delamination, electrolyte decomposition, solid electrolyte interface (SEI) growth, and lithium deposition [68]. The degradation is profoundly affected by time, temperature, SOC and C-rate.

The ageing phenomenon is a combination of calendar ageing and cycling ageing. Calendar ageing is the degradation of a battery over time without cycling or uses, which is dominated by the formation of SEI (affected by temperature and SOC). Cycling ageing is the life lost when a battery is cycled, affected by C-rate, temperature, SOC and SOH. Very high C-rate can increase the rate of degradation significantly; very high or low temperature is harmful to battery health; Higher depth of discharge is also a reason for the increase of degradation rate.

More factors need to be considered at the system-level than the cell-level to estimate SOH. For example, imbalance among the cells and contact resistance variation with time and other conditions [68]. There are detailed schematics of battery degradation in [69], based on chemical explanations. Diagnostics is about the state of the battery now, while prognostics is the prediction of the battery in the future based on a set of given conditions that the battery will be subjected to.

There is a range of methods to estimate SOH. The algorithms mostly at the cell-level, can be classified into three main categories: direct measurement, model-based methods and data-driven methods.

2.6.1 Direct measurement

Coulomb counting may be suitable for capacity estimation only when a full discharge is available (or almost full discharge, to be proposed later) and when accurate current sensors are available. This method cannot be utilised when a BESS is in operation for grid services and requires the BESS to go offline to carry out a full discharge. Similar to equation (2.2), the calculation

of capacity is shown in (2.6) by integrating the discharge current.

$$C = \int_{t_{start}}^{t_{end}} I_D dt \quad (2.6)$$

where t_{start} is the start time of the discharge process, t_{end} the end time and I_D is the discharge current.

As mentioned in SOC algorithms, Coulomb counting is suitable for both SOC and capacity estimations, so the advantages and disadvantages of this method for both estimations are the same.

2.6.2 Model-based methodology

State/ parameter observer

This category of SOH algorithms includes DEKF (extended Kalman filter) method, dual sliding mode observer [70], and particle filter. Advantages are that they are online and closed-loop. A relatively heavy computational burden is one of the main disadvantages. Besides, they are sensitive to the battery models, as discussed in section 2.5.2.

Particle filters are also called Sequential Monte Carlo Methods. They are a set of genetic, Monte Carlo algorithms (output may be incorrect with a certain probability) for solving filtering problems. Bayes' theorem describes the probability of an event according to prior knowledge of conditions, which might be related to the event. These filters are used in signal processing and Bayesian statistical inference (using Bayes' theorem to update the probability for a hypothesis). In [71], two degradation models, whose parameters are updated by a particle filter are proposed.

Kalman filter methods

A DEKF or a DSPKF can estimate both SOC and SOH by adding capacity as a parameter, together with other ECM parameters, to be estimated by the weight filter. This is because according to equation 2.2, SOC and SOH are related to each other closely, which is essential for the work represented

in this thesis. The basic knowledge of the KF family and the review of some representative works have been done in the review of SOC algorithms (section 2.5).

Observing internal resistance

The increase in the value of the series resistor in the ECM model of a Li-ion battery is an indicator of degradation [72]. Thus, there is a range of studies that estimate SOH using the change in the value of this resistor [73, 74].

In [72], authors proposed an on-board internal resistor estimation for EV SOH monitoring. They use terminal voltage and current measurement during battery operation as the identification signal and calculate the resistance with an adapted model, followed by the determination of the degradation index. This work achieved low computational burden, high robustness and good accuracy. It is worth mentioning that this work also considers the compensation of various temperatures, but not under dynamic load. Authors in [75] introduced a degradation model based on EIS measurements and a SOH monitor using recurrent neural networks (RNN), validated by the data from the real-life EV operating profile. They take the truth that the value of the resistors varies at different SOCs (OCV) into account. However this study is based on simulation rather than real-life operational data. The use of RNN increase the performance of the SOH monitor but inevitably requires a large amount of data.

These methods rely heavily on the accuracy of the ECM. The challenges are the difference between cells and the fact that the value of the resistor is affected by various factors, such as temperature and SOC.

2.6.3 Degradation modelling

Electro-chemical models

There is a range of studies focusing on the electro-chemical models of batteries, including the degradation of film resistance and the solid-electrolyte interface (SEI). In [76], an electro-chemical model was built to describe the

impact of SEI growth on cell capacity. The effects of SEI were investigated in [77].

Single-particle models can be used to estimate parameters, as they are simplifications of the 1D formulation for a lithium-ion battery. In [78], such a model with refined cell parameters was proposed based on simulation for investigating the factors of capacity fade of an LFP cell for both cycling and calendar ageing. The results showed that the significant factor of capacity loss during storage and cycling conditions is the loss of cyclable lithium. They illustrated theoretical and physical interpretations of some battery ageing phenomena. The disadvantages of particle models are that they could not solve SOH estimation issues directly and they used complicated partial differential equations.

Empirical and Semi-empirical performance models

Empirical modelling is based on entirely experimental results, i.e., for a given input the output can be measured. An empirical battery degradation model can be built, for example by curve fitting techniques, with the effects of the above-mentioned factors. Semi-empirical modelling combines experimental with theoretical modelling (circuit model-based methods). For a given input, the output/answer cannot be measured, and according to measured variables and theoretical considerations that relate the variables through fundamental principles (stress factors of SOH), the output/answer can be sought.

In [79], a semi-empirical degradation model that uses both destructive physical analysis and non-destructive electro-chemical analysis was proposed. In this paper, the four mentioned parameters: time, temperature, DoD and C-rate were investigated to predict SOH. An empirical model was built based on a large cycle-test matrix as well as a least-squares regression model. The authors attempted to establish a generalised life model considering time, C-rate and temperature. In different cases, the adopted life models (equations) were not identical, but all consisted of the mentioned four parameters. The models can work in various cycling conditions. As a result, at low C-rates, time and temperature are the main factors of capacity fade; at high C-rates,

the effects of cycle rates become significant. Another important conclusion in this paper is that capacity loss is significantly affected by time and temperature. The main drawback of this study is that the temperature range is limited.

In [80], a fatigue approach was used to do life-prediction. SOC and C-rate were chosen as stress factors as they have a significant impact on the extent of ageing. The authors found that the shape of current pulses has a minor effect on battery degradation. They provided the curves of stress factors versus cycles to fatigue failure and used a hypothesis for damage accumulation in a stress-varying profile.

Petit et al. [81] proposed an empirical degradation model considering 4 stress factors: SOC and temperature for calendar ageing; temperature and current for cycle ageing. This method was intended for V2G (vehicle to grid [82]) and two kinds of cells: LFP and NCA (lithium nickel cobalt aluminium oxide) were investigated. The authors concluded that the NCA based battery was more sensitive to cycle ageing. The downside of this method is that it neglected resistance increase, and the stress factors under consideration were limited to be only two for both calendar ageing and cycle ageing.

Xu et al. [83] introduced a semi-empirical degradation model of Lithium-ion batteries according to operating profiles. A rain-flow cycle-counting algorithm (a method to analyse fatigue data) was implemented to quantify the number of cycles based on the battery's SOC profile. They tune the model coefficients using data from the manufacturer. The stress factor models contain a temperature stress model; a SOC stress model; a time stress model and a DoD stress model. It is necessary to mention that the new empirical DoD stress model in this research can be used for both LFP and NMC batteries. The improvement of this study could be introducing more stress factors and making the rain-flow algorithm online.

2.6.4 Data-driven methodology

Directly mapping from ageing cycle to SOH

This category of methods estimates the battery SOH directly given a time series of capacity values over cycle numbers. Either machine learning algorithms or curve fitting techniques use capacity and number of cycles data pairs. Then SOH and EOL (end of life) are able to be estimated. Bayesian Monte Carlo and Artificial neural networks were used with other techniques to achieve direct mapping SOH prediction.

In [84], adaptive neural networks and linear prediction error methods were implemented by directly mapping the capacity-cycle data pairs. This method has the advantage of establishing a linear model for prognostics and remain useful life (RUL) prediction. Besides, two prognostics and health management (PHM) techniques with high accuracy were also presented.

The Dempster-Shafer theory (a general framework about uncertainty and an effective data fusion method) and Bayesian Monte Carlo (BMC) methodology were applied to observe the generative mechanism of the capacity-cycle data pairs in [85]. Bayesian Monte Carlo, which is a combination of Bayesian inference (using Bayes' theorem to update the probability for a hypothesis when some evidence or information is available) and Monte Carlo methods (a variety of computational algorithms that rely on repeated random sampling for numerical results) has been proposed for SOH estimation. Firstly, the Dempster-Shafer theory is used to obtain the information from available battery data to initialise model parameters. Then, BMC updates the model parameters using new measurements.

The accuracy of direct mapping could work well provided there is enough good quality data but ignoring stressing factors is the problem. Even for the cells that are from the same manufacture, the degradation curves are not identical, which exposes the problem of these methods for being non-generic.

Mapping from stressing factors or features extracted to SOH

In these methods, some readily measurable variables or features are the input of degradation models, such as historical SOC, temperature, discharge

current and depth of discharge (DoD).

This category of methods includes ANN, fuzzy logic, and support vector machines (SVM).

Fuzzy logic is a method based on the degree of truth rather than purely true or false. In [65], SOC is estimated by its correlation with battery impedance at one or two frequencies. Likewise, cycle number (SOH) is also related to impedance and frequency. The advantage is that fuzzy logic does not need an exact mathematical model to make a decision about a coefficient's selection [86]. However fuzzy logic may suffer from estimation accuracies [87].

Signal processing method

Signal processing techniques can also be used to analyse the health performance of batteries, including incremental capacity analysis (ICA), differential voltage analysis (DVA) and differential thermal voltammetry (DTV). Authors in [88] use the quantitative correlations between the IC (incremental capacity) peaks/ dV (differential voltage) and the cell faded capacity to estimate SOH. In [89], DTV is defined as the ratio of the temperature and voltage differentials (dT and dV), with respect to time. DTV is used for tracking degradation during a galvanostatic charge /discharge process with available measurements of the voltage and the temperature. Considering these methods may be sensitive to noise and hard to achieve on-board SOH monitoring, they could be combined with machine learning algorithms such as SVM [90].

Statistical metrics

Statistical dependence exploration examines the major factors affecting lithium-ion battery degradation [91]. This category of methods includes dependency analysis [92] and sample entropy [54, 68].

SampEn (sample entropy) feature can depict degradation and health condition of batteries. In [68], a relationship between the sample entropy of voltage sequence and capacity loss was built. Advanced sparse Bayesian pre-

dictive modelling (SBPM, an advanced machine learning algorithm) was used to establish the relationship. After using the sample entropy algorithm, the sample entropy and capacities were input to the SBPM system to learn the underlying mapping system. This method showed a better result over SVM (support vector machine) with much less complexity. An improved sample entropy (enhanced sample entropy) was proposed to be more practical [54], and the results showed that the error of the SOH estimator is as low as 2%. The main drawback of statistical methods is still the high criteria placed on data quality and quantity.

Among various SOH only algorithms [93], total least-square based methods can be relatively simply to implement, without the sacrifice of accuracy, if the data quality is guaranteed. In [94], the relationship between current integration and SOC variation was used as the foundation of total least-square based methods for capacity estimation. These algorithms, which include weighted total least squares (WTLS), total least squares (TLS) and approximate weighted total least squares (AWTLS), attempt to find an estimated capacity that minimises the sum of squared errors, which is done recursively. TLS is used in this work for system-level capacity estimation and the details of applying this method are in section 5.

2.6.5 Summary

There are other methods apart from the above-mentioned ones, for example, durability model-based open-loop methods [95, 96] and the battery model-based parameter identification closed-loop method [97]. They are not popular due to complexity and accuracy problems.

The rate of battery degradation depends on environmental impacts and operation profiles. Chemical analysis methods are hard to apply to electrical circuits. The impedance method can be accurate but it is complicated and offline (i.e. not in real-time). Machine learning algorithms and sample entropy are the most popular algorithms to estimate SOH. They can all be very accurate, but with high requirements on data quality and quantity. Most research of SOH algorithms is still at the cell-level, and the performance on

Table 2.4: Summary of data-driven SOH algorithms

Method	Examples	Advantages	Disadvantages
Directly mapping from cycle number to SOH	Adaptive neural networks and linear prediction error [84]; Bayesian Monte Carlo [85].	Straightforward, good nonlinear mapping	missing stressing factors and sensitive to the quantity and quality of battery data.
Mapping from stressing factors/features to SOH	Neural network, support vector machine and fuzzy logic [86, 98, 99, 100]	Not difficult to implement, good nonlinear mapping and accurate.	Sensitivity to the quantity and quality of battery data
Signal processing	ICA, DVA and DTV [88, 89]	Simple, accurate ,[89]	Easily affected by noise
Statistical methods	Dependency analysis and sample entropy [54, 92]	Simple, accurate	Sensitive to the quantity and quality of battery data
Least-square methods	Total least square methods[94]	Very Simple to implement	Sensitive to the quality of battery data

the system-level could be different, but these methods can still be tried. The summary of popular data-driven SOH algorithms is shown in table 2.4. For more SOH estimation algorithms and more details, see [6, 54].

2.7 Prognostics of batteries

Diagnostics and prognostics of SOH for batteries are two popular research areas. Prognostics of batteries is the main part of prognostics and health management (PHM) in batteries [89]. Prognostics tries to deal with the degradation of batteries. There are two aims of prognostics: the first one is to predict the remaining useful life (RUL) of batteries; the second one is to assess the confidence of the uncertainty estimate. The main aim of

PHM is to make sure the battery operates within the designed time limits. The accuracy of predicting RUL is important since risks and failures can be prevented if the estimation is accurate.

It can be seen that prognostics and SOH are closely related, so many SOH algorithms can also achieve prognostics. Prognostics methodologies can be divided into mechanism analysis based methods, data-driven based methods, and fusion methods that combine the above mentioned two methods. Apart from the works discussed above for SOH estimation, there are several other novel studies in recent years.

Data-driven approaches have become popular, and a simple method in this category is to use a direct mapping between cycle number and SOH. Richardson et al. [89] proposed to use Gaussian process (GP) regression for predicting battery life. GP is a kind of Bayesian non-parametric method, which models complex systems by dealing with uncertainty and defines a probability distribution over the function (capacity over cycles). Residuals can be modelled by a GP and the function is a sample from a Gaussian process [101]. The results show that this work overcomes the limitations of previous research of GPs for RUL prediction with reasonable accuracy. However, the authors argue that pure data-driven approaches should be used only when no function form of the underlying model is available. The limitation is that they assumed future capacity depends solely on past data.

Su et al. [102] proposed an interacting multiple model particle filter (IMMPF) method for RUL prediction. The authors achieved improving the accuracy of conventional battery capacity models. The results show that these models use fewer parameters, with stable and high prediction accuracy and narrowed uncertainty probability distribution function because the IMMPF method can balance the global and local nonlinear performance. A model based on mean entropy and relevance vector machine (RVM), was proposed and used to estimate SOH and RUL [103]. This work shows how to achieve precise results of RUL prediction. In comparison, RVM performs better than SVM and autoregressive integrated moving average (ARIMA) models. Authors in [104] proposed a method to predict RUL based on the Verhulst model, particle swarm optimisation (PSO) and particle filter (PF).

The authors use these technologies to form a fitting model and a predicting model, with high accuracy and fewer parameters than previous methods [105].

It is not hard to conclude that battery prognostics based on data-driven methods have made significant progress in the last few years [106]. Data-driven methods do not require an accurate mechanism analysis of the system but require an amount of high-quality data as discussed in SOH algorithms 2.6.

2.8 State estimation for battery systems

According to the reviews above, there are already a wide variety of methods to estimate battery capacity and SOC, but most of them focus at the cell-level. Plett. et al. [107] proposed a Bar-Delta filtering method for estimating the battery pack states, not only estimating the pack-average states but also the differences between the cell and pack-average states. In [108], an online estimation technology based on KF methods for SOC of all cells in the pack was proposed. Authors in [109] achieved accurate SOC estimation of a battery pack using an adaptive extended Kalman filter. Although the above methods could work well for battery packs, they would be much slower to be implemented for large-scale battery systems due to the significantly higher number of cells.

Recently, a digital twin method [110] for online SOC and SOH estimation was proposed. The authors built a cloud BMS with the Internet of things and achieved small errors for both state estimations. However, this study only uses a very small battery system, with 4 cells to validate the algorithms. A series of studies on a sample of Spanish photovoltaic household-prosumers [111, 112] showed factors that could affect a battery system's lifetime and predicted a battery bank's lifetime under fluctuating loads. The limitation is that this series of studies are based on fixed battery degradation parameters, which may not be practical.

To conclude, battery systems that previous studies use to demonstrate their methodologies contain a very small number of cells relative to large-scale

grid-connected BESS. A large-scale BESS system will be made up of storage units that can contain in excess of 20k-100k cells each and with it come challenges in measurement, data granularity, accuracy and data quality. The state estimation of an entire large-scale BESS for increased accuracy, beyond commonly used methods, has not been presented in the literature.

2.9 Thesis objectives

From the literature review above, it can be concluded that state estimation algorithms have only been implemented on the cell-level and battery systems with very limited size. Therefore, an objective will be to investigate whether the more advanced methods such as the Kalman filter family and machine learning algorithms provide similarly good results on large-scale grid connected batteries. These methods will require sensor data from the battery therefore the research should consider where on the system this data is taken from and how it affects the results. For the SOC it should be an objective to experimentally compare it against the SOC provided by the manufacturers BMS and if improvements are observed, then to understand under what conditions this can be exploited. In the literature online methods have been demonstrated under mostly ideal conditions, this research should consider real-world conditions and also account for the scenario where these algorithms could run remotely. The final objective is to investigate if the state estimation algorithms can provide other indicators on the health of the battery or whether the equivalent circuit parameters can be extracted at this scale to aid in modelling and simulation.

Chapter 3

Experimental setup

3.1 Introduction

To investigate system-level state estimation algorithms, this thesis uses various batteries, from single cells to battery systems. In this chapter, the batteries, test equipment and commonly used data profiles in chapters are detailed. The main battery investigated in this research is the Willenhall Energy Storage System (WESS), and will be introduced first, followed by others.

3.2 Willenhall Energy Storage System (WESS)

In this thesis cell-level DSPKF techniques are going to be demonstrated on a large scale BESS called the WESS as it is located at Willenhall, in the UK. WESS is the largest research based grid-connected lithium titanate energy storage facility in the GB [4], which was commissioned in 2016 by The University of Sheffield (TUoS). It is sited at a 33kV/11kV substation and is connected at 11kV to the grid through a 11kV/350V 2.1MVA transformer.

As stated in chapter 2, Lithium titanate (LTO) batteries are safer, offering high charge/discharge rates, low-temperature operation and significantly longer lifespans [113] by comparison with conventional lithium-ion batteries. The disadvantages of these cells are their higher cost and that they operate

at a lower voltage, however this can be overcome in BESSs by connecting more cells in series.

The system consists of 21,120 Toshiba LTO cells and the highest power and energy capacity are 2 MW and 1 MWh respectively. The nominal capacity of a single cell is 20 Ah and for the system is 1600 Ah. The system consists of 40 racks in parallel, 22 modules in series in every rack, and 24 cells in each module in a 2P12S configuration. Physically in the battery container 2 racks make up a string due to the height restriction and the increased number of cells required in series due to the low LTO voltage. In this thesis the words string and rack are used interchangeably to be consistent with other usages of the terms in the literature. A schematic of the battery system configuration is illustrated in Figure 3.3. The specifications of the WESS are shown in table 3.1. The modules in each rack communicate over CAN bus to a rack management unit (RMU) that collects the voltages of all the parallel connected cells (12 voltage measurements). The RMU also measures the total current in/out of each rack, which is then communicated back over CAN bus along with voltage information (cell Min/Max and rack voltage) to a system BMS. The system BMS measures the overall dc-link voltage and current that is connected to the inverter. The BMS reports over Modbus TCP/IP various system parameters, those important for this thesis are, dc-link voltage, current and SOC. The photographs of the WESS, some racks in the WESS, an LTO module and an LTO cell in the system are shown in Figure 3.1 and Figure 3.2. A diagram of the system is shown in Figure 3.4.

Each rack is fitted with a current sensor so the system-level current is obtained by summing the rack currents. System-level voltage is the same for each of the 40 racks. The system-level SOC can be defined by averaging the rack-level SOCs that are calculated by the rack currents when the system is operating since when it is in equilibrium state, the SOCs of the racks and cells should be the same. The system-level capacity is the sum of all the 40 racks' capacities and a rack's capacity is about twice that of a cell. The rack-level measurements are not considered in this work because the system-level (dc-link) current, voltage and SOC are provided by the BMS and the system capacity can be estimated based on these system-level values alone.

Table 3.1: WESS specifications

Manufacture	Toshiba
Max power	2 MW
Nominal capacity (kWh)	968
Nominal capacity (Ah)	1600
Max power	2 MW
Nominal voltage (V)	610
Min voltage (V)	550
Max voltage (V)	712
No. of cells in total	21120
No. of strings	40
No. of modules in each string	22
No. of cells in each module	24
Cell model	SciB 20 Ah
Cell chemistry	LTO
Inverter capacity (MVA)	2
NO. of inverters	24
Transformer capacity (MVA)	2.1

The BMS reported SOC of the WESS is an estimate using a Coulomb-counting method and uses the OCV-SOC relationship for correction when the battery is at a predefined condition (only known to the manufacturer) during voltage relaxation. As previously discussed in section 2.5.1, the Coulomb-counting estimated SOC suffers from error accumulation over periods of sustained charge/discharge.

The data collected from WESS is stored in real-time to a time-series database, influxDB. The data can be viewed and downloaded by use of Grafana, which is a data-visualisation tool. An example of Grafana is shown in Figure 3.5.

An example of WESS operation is shown in Figure 3.6. The 3-day data in Figure 3.6a include system-level current, voltage, BMS SOC and power. Note that the zeros in the voltage and SOC profile indicate the occurrence of invalid data, which will be discussed in detail later (section 4.6). The control of the system is managed by a National Instruments CompactRIO which runs control software and a GUI developed by researchers at TUoS.



Figure 3.1: Photographs of (a) the WESS and (b) some racks inside the WESS.

This controller allows the system to be operated, at its most simplest level, by direct command of real power and reactive power through the GUI. It also supports the import or algorithms for control such as the frequency response services described in this thesis. Under day-to-day operation the controller communicates over a secure connection to a trading company that operates the battery to generate income in the various markets. For the work in this thesis some of the experimental data is taken through direct control of the battery using power request profiles that are imported into the controller. Other data is taken from its normal day-to-day operation.

An air-conditioning system aims to maintain the temperature of the cells to a narrow range of between 20-30°C under normal operation. In Figure 3.6b, the average temperature of all the cells in each rack is shown, and the thick blue trace is the average temperature of all the cells in the WESS. This is done to investigate whether temperature variations affect the accuracy of the state estimation algorithms that are introduced in this work.

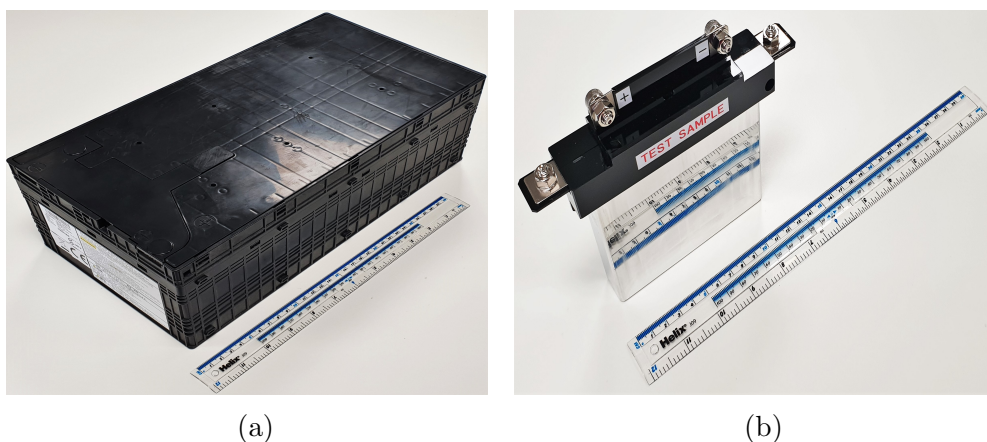


Figure 3.2: Photographs of (a) a sample module inside the WESS and (b) a simple cell inside the WESS.

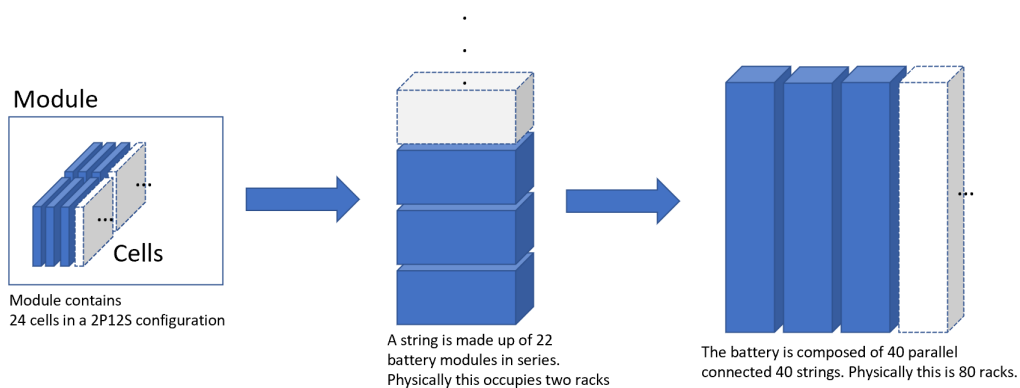


Figure 3.3: Battery system configuration of the WESS.

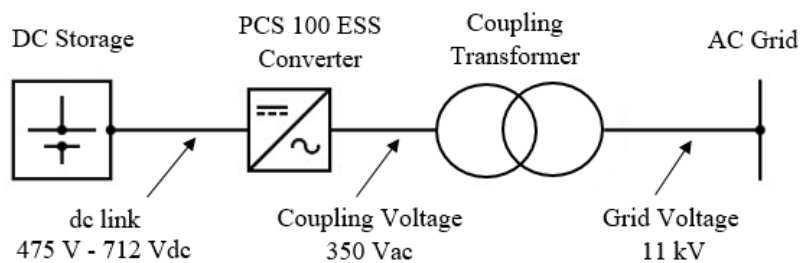


Figure 3.4: System diagram of the WESS.



Figure 3.5: Example WESS data on grafana: constant cycling.

3.3 Other batteries used to investigate the algorithms

3.3.1 NMC and LTO cells

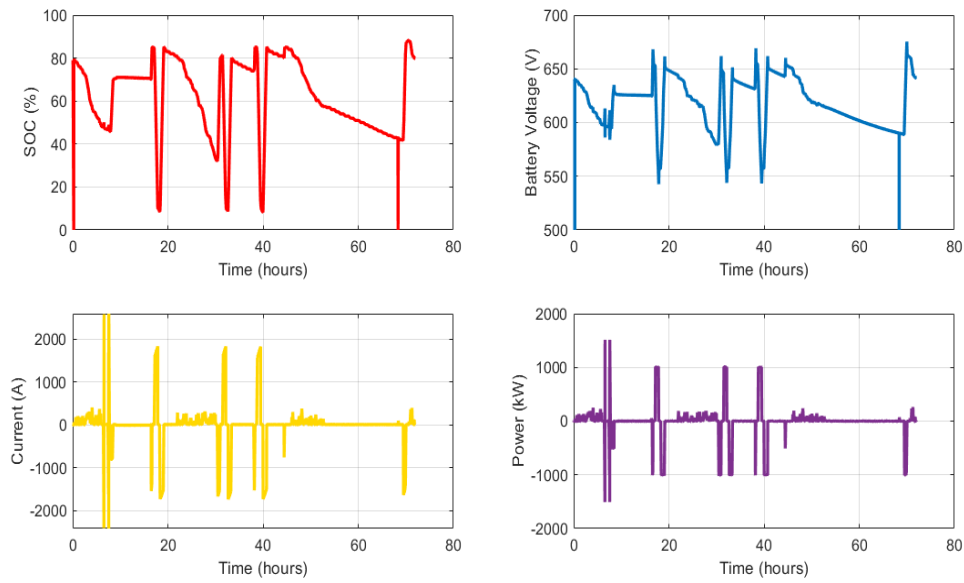
Figure 3.7 shows 2 NMC cells of different brands, JGNE (Shandong Goldencell Electronics Technology Co.,Ltd) and CHAM (ShenZhen Cham Battery Technology Co.,Ltd) respectively. Through cycling tests, the JGNE cell (right) have reached EOL and the CHAM cell (left) has also shown significant degradation. They are used in this thesis for investigating SOH algorithms.

The cell-level results that are shown in this thesis are also from an 20 Ah LTO cell, which is the same as the cells in the WESS, as shown in Figure 3.2b.

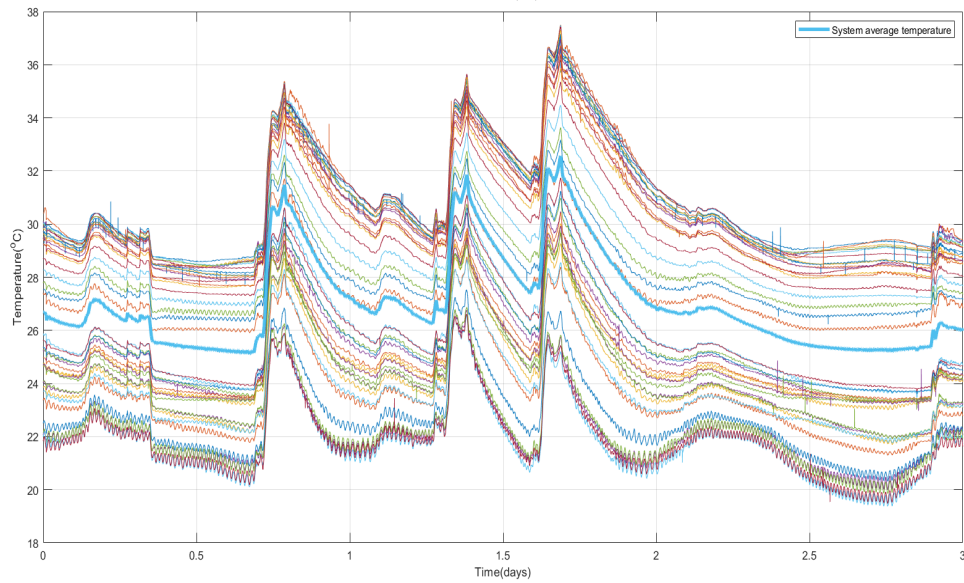
The specifications of the cells are shown in table 3.2.

3.3.2 GS Yuasa rack

The DSPKF has also been implemented on a GS Yuasa battery rack, which can be seen as a small battery system. In the rack, there are 14 GS Yuasa modules (datasheet see appendix) in series and inside each module there are



(a)

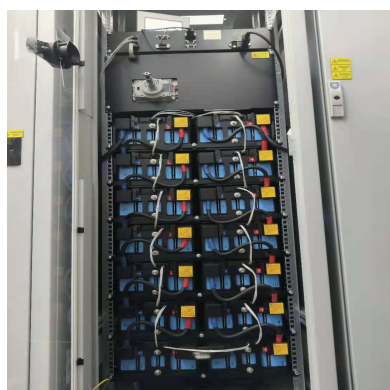


(b)

Figure 3.6: WESS operation data in 3 days (a) system-level current, voltage, BMS SOC and power and (b) temperature of each string and system average temperature.



Figure 3.7: NMC cells: the CHAM cell on the left and the JGNE cell on the right.



(a)



(b)



(c)

Figure 3.8: Photographs of (a) GS Yuasa LIM50ER rack, (b) GS Yuasa LIM50E module and (c) GS Yuasa cell inside the modules.

Table 3.2: Cell specifications

Manufacture	Toshiba	CHAM	JGNE
Model	SCiB 20Ah	CMICR 18650F8	HTCNR 18650
Chemistry	LTO	NMC	NMC
Nominal capacity (Ah)	20	2.6	
Nominal voltage (V)	2.3	3.6	3.6
Min voltage (V)	1.5	2.75	2.75
Max voltage (V)	2.7	4.2	4.2
Standard Charge C-rate	-	0.5	0.5
Max Charge C-rate	10	0.5	1
Max Discharge C-rate	10	2	3
Datasheet Impedance at 1kHz (m Ω)	0.53	35	40
Min Discharge Temperature ($^{\circ}$ C)	-30	-20	-20
Max Discharge Temperature ($^{\circ}$ C)	55	60	50
Min Charge Temperature ($^{\circ}$ C)	-30	0	0
Max Charge Temperature ($^{\circ}$ C)	55	55	45
Specific Energy (Wh/kg)	90	-	-
Energy Density (Wh/L)	177	-	-

12 47.5 Ah GS Yuasa cells in series, as shown in Figure 3.8. The rack has an internal BMS, and methods similar to the WESS are used to estimate the rack-level SOC. However, through experiments it has been found that the internal BMS does not have a capacity estimation of itself and the correction of SOC according to the OCV-SOC relationship has significant time lags.

3.3.3 GS Yuasa battery system

The algorithms have also been implemented on a larger GS Yuasa battery system named ADEPT, which is the world’s first container dual chemistry BESS [114]. A photograph of the system is shown in Figure 3.9. This system has 3 GS Yuasa battery racks in parallel and a lead-acid battery system, but only the Li-ion data is used in this thesis. Inside the Li-ion racks, the modules and the cells are exactly the same as the above mentioned rack, but having 12 GS Yuasa modules in series, which is 2 less. This battery system is also integrated with an internal BMS. However, the BMS system is proprietary and its SOC operation is commercial sensitive and therefore unavailable for scrutiny.



Figure 3.9: Photograph of the ADEPT BESS.

3.4 Cell-level battery test equipment

There are three main test equipment used to obtain cell-level results, namely EIS tests and cycling tests. The EIS test is undertaken by the EIS machine, Bio-Logic SP-300, as shown in Figure 3.10a. The cycling test is done by the Maccor Series 4000 battery tester, as shown in Figure 3.10b. Both the EIS machine and the Maccor battery tester work with a PHCbi environmental chamber with -10 to 60°C temperature range, as shown in Figure 3.10c to maintain the test temperature and ensure safety. The specifications of the EIS machine and the Maccor battery tester are shown in tables 3.3 and 3.4 ([115, 116]).

3.5 Data profiles

3.5.1 A DFR data profile

An example of DFR service is shown in Figure 3.11. Figure 3.11a shows the relationship between power and frequency, while Figure 3.11b illustrates the response of the WESS by simulation, with not only power and frequency profiles, but also the SOC profile.



(a)

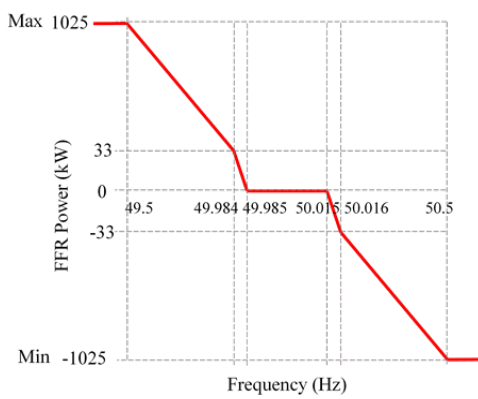


(b)

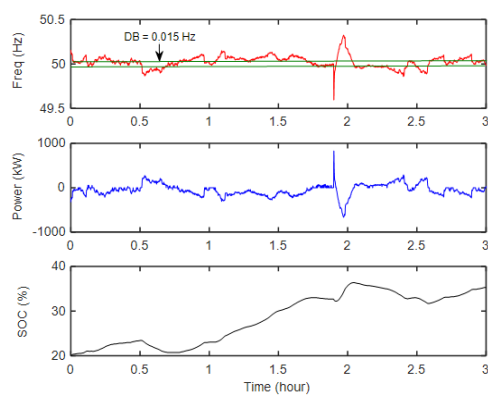


(c)

Figure 3.10: Pictures of cell-level battery test equipment (a) EIS tester (b) Maccor battery tester and (c) an environmental chamber.



(a)



(b)

Figure 3.11: Dynamic frequency response (a) power vs. frequency envelope and (b) example of BESS power response.

Table 3.3: Maccor S4000 specifications

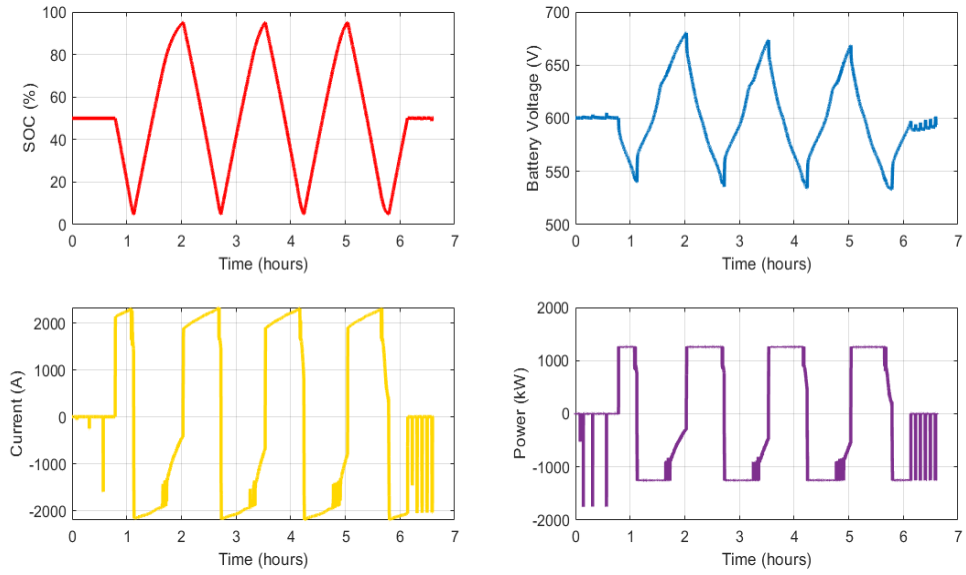
Number of Test Channels:	1 to 192 per system
Voltage Ranges:	available up to 180 V maximum
Voltage Accuracy:	0.02% of full scale voltage
Voltage Resolution:	16 bit
Current Ranges:	Single Current Range 1 mA to 2000 A; Four Current Ranges: 150 μ A, 5 mA, 150 mA, 5 A
Current Accuracy:	0.02% of full scale current on 5 Amp Multi-range channels
Current Accuracy:	0.05% of full scale current on all other channels
Current Resolution:	16 bit
Time Resolution:	10 mS standard, with 5 mS and 1 mS as an option
Minimum Pulse width:	100 μ S
Rise Time:	<500 μ S standard in constant current modes, 100 μ S or 20 μ S optional
Data Recording Rate:	200 data points per second per system standard
Data Recording Interval:	Δ Time(minimum 10 mS standard, 5 mS and 1 mS as an option), Δ V, Δ I, Δ Ah, Δ Wh, Δ T, Δ P
Operating Modes:	Constant Current, Constant Voltage, Constant Power, Constant Resistance, Voltage Scan (Cyclic Voltametry)
Number of Steps per Test:	127 standard plus subroutines
Step End Conditions:	Voltage, Current, Time, -dV, dV/dT, dV/dt, Ah, Wh, HCAh, HC Wh, LHC Ah, LHC Wh, Auxiliary Voltage, Reference Electrode Voltage, Temperature, dT/dt, dT/dt, pH, Pressure

Table 3.4: BioLogic SP-300 specifications

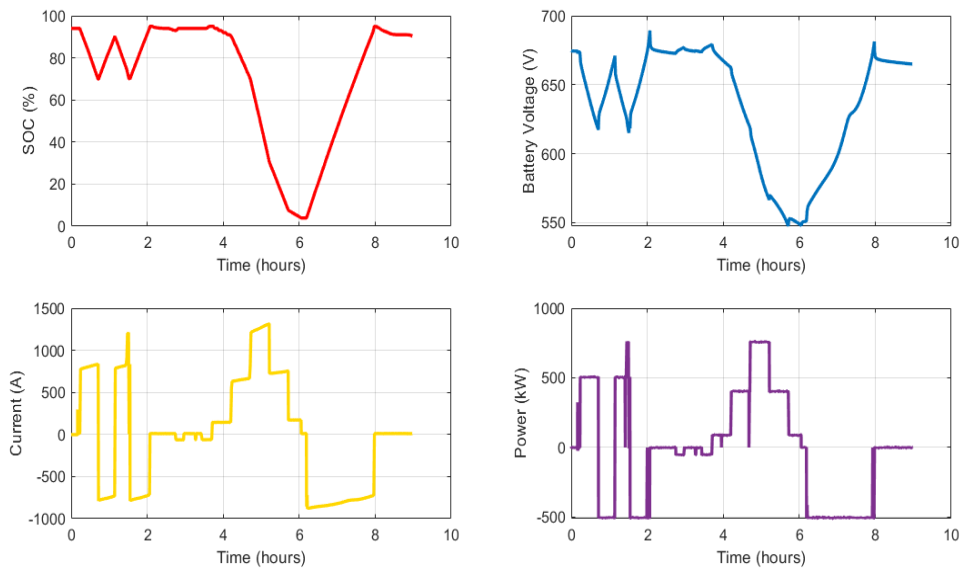
Voltage	Compliance: ± 12 V; ± 49 V with 1A/48 V booster Control voltage: ± 10 V ± 48 V with 1 A/48 V booster Voltage resolution: 1 μ V on 60 mV range
Current	Current ranges: 500 mA to 10 nA (standard); down to 1 pA (Ultra Low Current) Maximum current: ± 500 mA (standard); up to 120 A with four HCV-3048 Current resolution: 760 fA (standard) Low current: 6 ranges from 100 nA to 1 pA with resolution to 76 aA
EIS	Frequency range: 7 MHz (3%, 3°) down to 10 μ Hz; 3 MHz (1%, 1°) EIS quality indicators
Advanced	Up to 2 channels Connection 2,3,4,5 terminal lead 12 μ s with EC-Lab Express; 1 μ s with ARG option Floating mode Analog filtering Calibration board Full stability control mode (9 bandwidths)

3.5.2 WESS data profiles commonly used in chapters

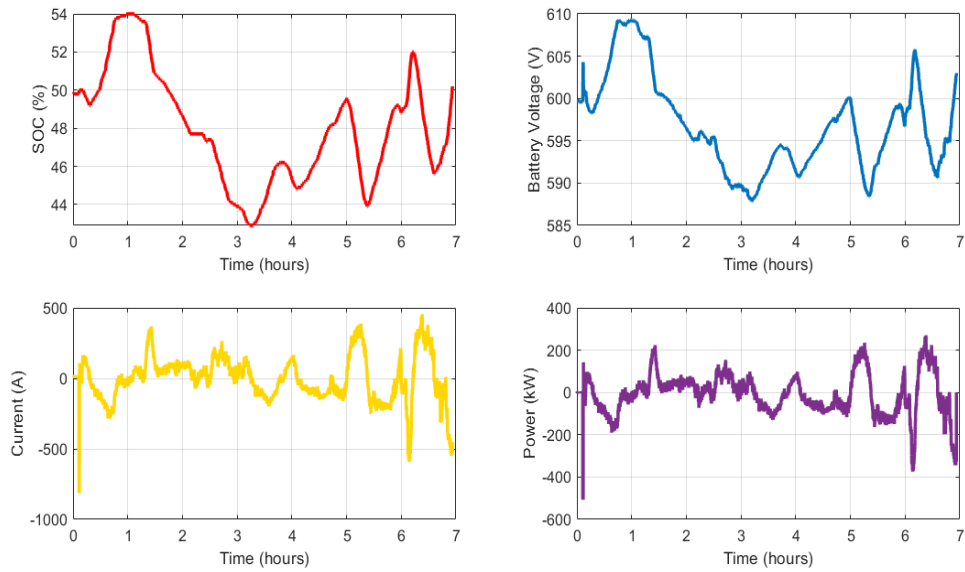
The profiles in Figure 3.12 are WESS's operation data: constant cycling, a mixed profile and grid frequency response service (DFR). The constant cycling profile contains 3 cycles of the battery at 1.25C, from 5% to 95% SOC. The mixed profile consists of 2 small cycles followed by an almost full cycle. The DFR profile has much smaller current than the previous profiles, so the SOC variation is much smaller.



(a)



(b)



(c)

Figure 3.12: Data profiles of the WESS (a) Constant cycling, (b) a mixed profile and (c) DFR.

3.5.3 OCV data profiles

OCV-SOC relationships are essential in this research for WESS state and parameter estimation, so both the cell-level (LTO) and the system-level OCV-SOC relationship tests were conducted and the data profiles of them are shown in Figure 3.13 and Figure 3.14.

At the cell-level (Figure 3.13), the full discharge capacity (constant current, 1C) is measured first, after a full charge using the CC-CV technique. Then the cell is fully charged again, followed by 10% discharge (as of the measured capacity) each time, until the cut-off voltage is reached. After each step discharge, the battery is rested for an hour to measure the OCV. In terms of the system-level OCV-SOC measurements (Figure 3.14), the BMS SOC is used for the step discharges. The limits of the SOC range 100% and 0% of WESS are not tested due to operating restrictions. These have been established by the research team operating the WESS. For example, operating at 0% SOC is to be avoided as the batteries are operating very close to the minimum voltage of the inverter, if they were to discharge further

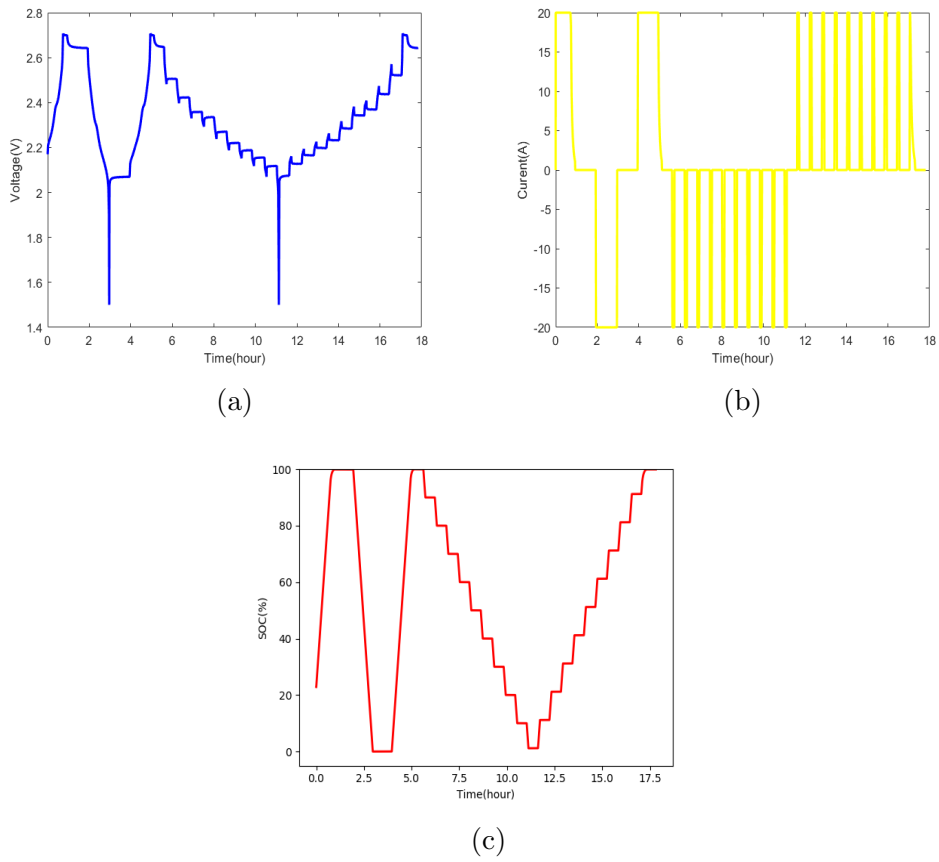


Figure 3.13: LTO cell SOC estimation results with an OCV profile (a) cell voltage, (b) cell current and (c) SOC estimation results using Coulomb counting.

then manual intervention is necessary to bring the system back online. The C-rate and the rest periods are the same for both cell-level and system-level experiments.

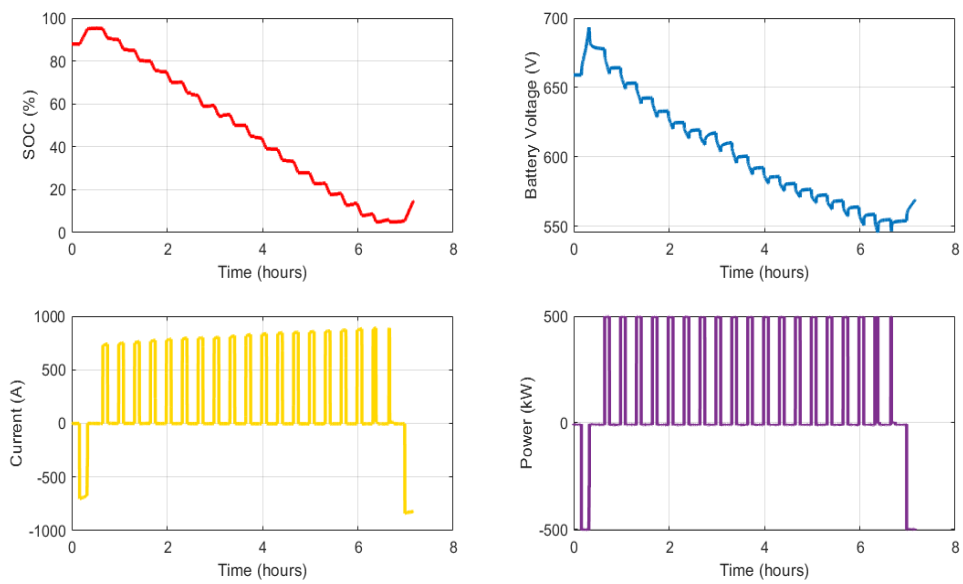


Figure 3.14: OCV-SOC test data profile of the WESS.

Chapter 4

SOC estimation of large-scale battery systems

4.1 Introduction

SOC is the most noticeable battery state in daily life. One's daily routine could be seriously affected by a low-charged phone battery. For a battery system, the SOC affects whether it can deliver the amount of energy needed for a service. Besides, accurate SOC estimation avoids over-charge or over-discharge, for safety and battery health. Among various battery states, SOC is not the most complicated to be estimated, so the SOC estimation of large-scale battery systems is demonstrated in this chapter.

As reviewed in chapter 2, Kalman filter (KF) methodologies are possibly the best candidates for system-level estimation. Thus, KF methods are chosen for the SOC estimation in this work. SPKF, as the state-of-art in the KF family, is preferred and implemented for the most results.

EKF, SPKF, DEKF or DSPKF implementations, have only been demonstrated on the cell-level, so this chapter mainly demonstrate the utilisation of them on the system-level. However, to show the advantage of the algorithms developed in this work, the algorithms are first implemented on the cell-level, followed by the battery rack, a small battery system (GS Yuasa) and finally a large-scale battery system (WESS). The cell-level SOC estimation uses the

LTO cell inside the WESS and the rack-level estimation uses the GS Yuasa rack, and both of them are introduced in section 3.3. The system-level estimation is mainly demonstrated on the WESS, apart from a short profile of the GS Yuasa battery system.

The cell-level SOC results are compared with the Coulomb counting ones produced by the Maccor battery tester. The rack-level and system-level SOC results are compared with the BMS's that the manufactures provided. Both results of DEKF and DSPKF for WESS SOC estimation are shown and compared.

To make the algorithms applicable for all battery systems, the genetic algorithm (GA) is utilised to tune the KF in this chapter. The details of choosing GA parameters, and the process of GA converging are demonstrated.

OCV-SOC relationship is essential for SOC estimation using KF methods. This work provides two ways of obtaining system-level OCV-SOC relationship.

The SOC is fast-changing while equivalent-circuit parameters are not, so multi-scale KFs are utilised for reducing the complexity of KF algorithms.

Online SOC tracking of the WESS has been achieved using the proposed DEKF and DSPKF, using data from the time series data database, influxDB.

4.2 DEKF and DSPKF implementation on large-scale battery systems

4.2.1 Equations and battery models

Table 4.1 shows the equations for a multi-scale DSPKF implementation [49, 52]. They describe the whole procedure of initialisation, time update (prediction) and measurement update (correction) for both state and weight filters. k is the sample rate of the system data, and m is the macro scale, which is a quantity of samples. The parameters in the first order equivalent circuit model and the battery capacity are slowly time-varying so using a macro scale to estimate them is deemed efficient. The SOC is estimated ev-

ery sample while the parameters including capacity are estimated each time there are m new data samples.

In the table below, forms of X are for the states estimation (SOC), forms of θ battery equivalent circuit parameters, forms of L the Kalman gains, forms of P the error covariance and noise covariance matrices, and E represents the expectation. u_k and y_k are the measured current and voltage respectively. w_k and v_k are the process and observation noises. For the calculations of $\alpha_i^{(m)}$, $\alpha_i^{(c)}$ and lower triangular matrix see [49]. The state vector is augmented to include the noise effects so that the new vector length is p . $f(\bullet)$ and $h(\bullet)$ are the non-linear state transition and observation models' functions, respectively. They are derived from the equivalent circuit models and will be discussed below.

Table 4.1: Multi-scale DSPKF implementation

Definitions:

$$x_k^a = [x_k^T, \omega_k^T, v_k^T]^T, \quad X_k^a = [(X_k^x)^T, (X_k^\omega)^T, (X_k^v)^T]^T$$

$$p = 2 \times \dim(x_k^a)$$

Initialisation: for $k=0$, set

$$\hat{\theta}_0^+ = E[\theta_0], \quad P_{\hat{\theta},0}^+ = E[(\theta_0 - \hat{\theta}_0^+)(\theta_0 - \hat{\theta}_0^+)^T]$$

$$\hat{x}_0^+ = E[x_0], \quad \hat{x}_0^{a,+} = E[x_0^a] = [(\hat{x}_0^+)^T, \bar{\omega}, \bar{v}]^T$$

$$P_{x,0}^+ = E[(x - \hat{x}_0^+)(x - \hat{x}_0^+)^T]$$

$$P_{x,0}^{a,+} = E[(x_0^a - \hat{x}_0^{a,+})(x_0^a - \hat{x}_0^{a,+})^T] = \text{diag}(P_{x,0}^+, P_\omega, P_v)$$

State filter equations, for $k=1,2,\dots$ compute:

Time-update equations for state filter

$$X_{k-1}^{a,+} = \{\hat{x}_{k-1}^{a,+}, \hat{x}_{k-1}^{a,+} + \sqrt{P_{\bar{x},k-1}^{a,+}}, \hat{x}_{k-1}^{a,+} - \sqrt{P_{\bar{x},k-1}^{a,+}}\}$$

$$X_{k,i}^{x,-} = f(X_{k-1,i}^{x,+}, u_{k-1}, X_{k-1,i}^{\omega,+}, \hat{\theta}_k^-, k-1) \quad \hat{x}_k^- = \sum_{i=0}^p \alpha_i^{(m)} X_{k,i}^{x,-}$$

$$P_{\bar{x},k}^- = \sum_{i=0}^p \alpha_i^{(c)} (X_{k,i}^{x,-} - \hat{x}_k^-)(X_{k,i}^{x,-} - \hat{x}_k^-)^T$$

Output estimate, state filter

$$Y_{k,i} = h(X_{k,i}^{x,-}, u_k, X_{k-1,i}^{v,+}, \hat{\theta}_k^-, k) \quad \hat{y}_k = \sum_{i=0}^p \alpha_i^{(m)} Y_{k,i}$$

State filter gain matrix

$$P_{\hat{y},k} = \sum_{i=0}^p \alpha_i^{(c)} (Y_{k,i} - \hat{y}_k)(Y_{k,i} - \hat{y}_k)^T$$

$$P_{\hat{x}\hat{y},k}^- = \sum_{i=0}^p \alpha_i^{(c)} (X_{k,i}^{x,-} - \hat{x}_k)(Y_{k,i} - \hat{y}_k)^T$$

$$L_k^x = P_{\hat{x}\hat{y},k}^- P_{\hat{y},k}^{-1}$$

Measurement-update equations for state filter

$$\hat{x}_k^+ = \hat{x}_k^- + L_k^x (y_k - \hat{y}_k) \quad P_{\hat{x},k}^+ = P_{\hat{x},k}^- - L_k^x P_{\hat{y},k} (L_k^x)^T$$

Weight filter equations, for $k \bmod m = 0$ compute:

Time-update equations for weight filter

$$\hat{\theta}_k^- = \hat{\theta}_{k-1}^+ \quad P_{\hat{\theta},k}^- = P_{\hat{\theta},k-1}^+ + P_r$$

Output estimate, weight filter

$$W_k = \{\hat{\theta}_k^-, \hat{\theta}_k^- + \sqrt{P_{\hat{\theta},k}^-}, \hat{\theta}_k^- - \sqrt{P_{\hat{\theta},k}^-}\}$$

$$D_{k,i} = h(f(\hat{x}_{k-1}^+, u_{k-1}, \bar{\omega}_{k-1}, W_{k,i}, k-1), u_k, \bar{v}_k, W_{k,i}, k)$$

$$\hat{d}_k = \sum_{i=0}^p \alpha_i^{(m)} D_{k,i}$$

Parameter filter gain matrix

$$P_{\hat{d},k} = \sum_{i=0}^p \alpha_i^{(c)} (D_{k,i} - \hat{d}_k)(D_{k,i} - \hat{d}_k)^T$$

$$P_{\hat{\theta}\hat{d},k}^- = \sum_{i=0}^p \alpha_i^{(c)} (W_{k,i} - \hat{\theta}_k^-)(D_{k,i} - \hat{d}_k)^T$$

$$L_k^\theta = P_{\hat{\theta}\hat{d},k}^- P_{\hat{d},k}^{-1}$$

Measurement-update equations for weight filter

$$\hat{\theta}_k^+ = \hat{\theta}_k^- + L_k^\theta (y_k - \hat{d}_k) \quad P_{\hat{\theta},k}^+ = P_{\hat{\theta},k}^- - L_k^\theta P_{\hat{d},k} (L_k^\theta)^T$$

Sharing the symbols with the table above, table 4.2 shows the equations

for DEKF implementation [50].

Table 4.2: DEKF implementation

Initialisation: for $k=0$, set

$$\begin{aligned}\hat{\theta}_0^+ &= E[\theta_0], & P_{\theta,0}^+ &= E[(\theta_0 - \hat{\theta}_0^+)(\theta_0 - \hat{\theta}_0^+)^T] \\ \hat{x}_0^+ &= E[x_0], & P_{x,0}^+ &= E[(x - \hat{x}_0^+)(x - \hat{x}_0^+)^T]\end{aligned}$$

For $k=1,2,\dots$ compute:

Time-update equations for weight filter

$$\hat{\theta}_k^- = \hat{\theta}_{k-1}^+ \qquad P_{\hat{\theta},k}^- = P_{\hat{\theta},k-1}^+ + Q_k^\theta$$

Time-update equations for state filter

$$\hat{x}_k^- = f(\hat{x}_{k-1}^+, u_{k-1}, \hat{\theta}_k^-) \qquad P_{\tilde{x},k}^- = F_{k-1} P_{\tilde{x},k-1}^+ F_{k-1}^T + Q_k^x$$

Measurement-update equations for state filter

$$\begin{aligned}L_k^x &= P_{\tilde{x},k}^- (H_k^x)^T [H_k^x P_{\tilde{x},k}^- (H_k^x)^T + R_k^x]^{-1} \\ \hat{x}_k^+ &= \hat{x}_k^- + L_k^x [y_k - h(\hat{x}_k^-, u_k, \hat{\theta}_k^-)] \\ P_{\tilde{x},k}^+ &= (I - L_k^x H_k^x) P_{\tilde{x},k}^- (I - L_k^x H_k^x)^T + L_k^x R_k^x (L_k^x)^T\end{aligned}$$

Measurement-update equations for weight filter

$$\begin{aligned}L_k^\theta &= P_{\hat{\theta},k}^- (H_k^\theta)^T [H_k^\theta P_{\hat{\theta},k}^- (H_k^\theta)^T + R_k^{\theta}]^{-1} \\ \hat{\theta}_k^+ &= \hat{\theta}_k^- + L_k^\theta [d_k - h(\hat{x}_k^-, u_k, \hat{\theta}_k^-)] \\ P_{\hat{\theta},k}^+ &= (I - L_k^\theta H_k^\theta) P_{\hat{\theta},k}^- (I - L_k^\theta H_k^\theta)^T + L_k^\theta R_k^\theta (L_k^\theta)^T\end{aligned}$$

where,

$$\begin{aligned}F_{k-1} &= \left. \frac{\partial f(x_{k-1}, u_{k-1}, \hat{\theta}_k^-)}{\partial x_{k-1}} \right|_{x_{k-1}=\hat{x}_{k-1}^+} & H_k^x &= \left. \frac{\partial h(x_k, u_k, \hat{\theta}_k^-)}{\partial x_k} \right|_{x_k=\hat{x}_k^-} \\ H_k^\theta &= \left. \frac{\partial h(\hat{x}_k^-, u_k, \theta_k)}{\partial \theta_k} \right|_{\theta_k=\hat{\theta}_k^-}\end{aligned}$$

There could be n RC branches, and the model accuracy is higher with more branches, but it increases calculation burdens. The model with only one RC branch is chosen in this work for LTO batteries, because of the dom-

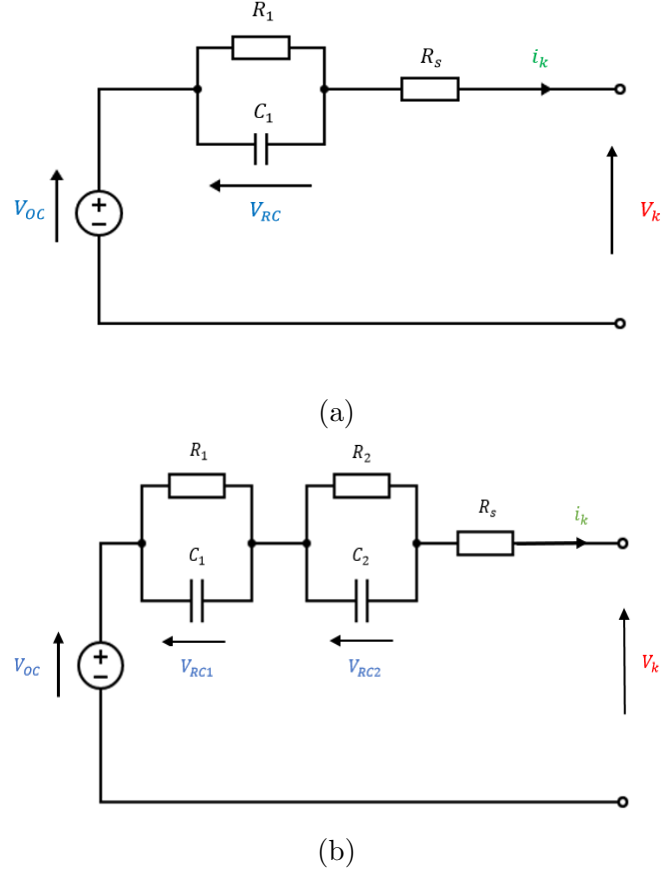


Figure 4.1: Equivalent circuit models of (a) first-order for the LTO cell and the WESS and (b) second-order for other batteries.

inant diffusion impedance effects in LTO cells [117], which is considered as having sufficient accuracy at low computational complexity. Comparison and discussion of using one or two RC branches for the WESS will be conducted in detail in the result section (4.4). For other batteries in this thesis, the model with two RC branches is chosen.

$$f(\bullet) = \begin{bmatrix} x_1 \\ x_2 \end{bmatrix} = \begin{bmatrix} SOC_{k+1} \\ V_{RC_{k+1}} \end{bmatrix} = \begin{bmatrix} 1 & 0 \\ 0 & e^{-\frac{\Delta t}{\tau_1}} \end{bmatrix} \begin{bmatrix} SOC_k \\ V_{RC_k} \end{bmatrix} + \begin{bmatrix} -\frac{\eta \Delta t}{Q_{actual}} & 0 \\ 0 & R_1(1 - e^{-\frac{\Delta t}{\tau_1}}) \end{bmatrix} I_k \quad (4.1)$$

$$\theta_k = [R_s, R_1, \tau_1]^T \quad (4.2)$$

$$h(\bullet) = V_k = V_{OC}(SOC_k) - V_{RC1_k} - I_k R_s \quad (4.3)$$

$$f(\bullet) = \begin{bmatrix} x_1 \\ x_2 \\ x_3 \end{bmatrix} = \begin{bmatrix} SOC_{k+1} \\ V_{RC1_{k+1}} \\ V_{RC2_{k+1}} \end{bmatrix} = \begin{bmatrix} 1 & 0 & 0 \\ 0 & e^{-\frac{\Delta t}{\tau_1}} & 0 \\ 0 & 0 & e^{-\frac{\Delta t}{\tau_2}} \end{bmatrix} \begin{bmatrix} SOC_k \\ V_{RC1_k} \\ V_{RC2_k} \end{bmatrix} + \begin{bmatrix} -\frac{\eta \Delta t}{Q_{actual}} & 0 & 0 \\ 0 & R_1(1 - e^{-\frac{\Delta t}{\tau_1}}) & 0 \\ 0 & 0 & R_2(1 - e^{-\frac{\Delta t}{\tau_2}}) \end{bmatrix} I_k \quad (4.4)$$

$$\theta_k = [R_s, R_1, \tau_1, R_2, \tau_2]^T \quad (4.5)$$

$$h(\bullet) = V_k = V_{OC}(SOC_k) - V_{RC1_k} - V_{RC2_k} - I_k R_s \quad (4.6)$$

Equations 4.1 to 4.3 [118] are used for the DSPKF or DEKF implementation on the WESS (and the LTO cell) based on the chosen first-order model. Likewise, Equations 4.4 to 4.6 are for the DSPKF implementation on other batteries that studied in this thesis. η is the battery Coulombic efficiency and Δt is the sample period of data. In the RC branch, the changes in C_1 are suitable indicators of the changes in SOH [119], R_1 the self-discharge resistance, and $\tau_1 = C_1 R_1$ is the time constant of the RC branch, similar for R_2 and τ_2 . The last equivalent circuit parameter R_s represents the resistance of the battery's terminals and inter-cell connections. Q_{actual} is the actual capacity in Coulombs and V_{OC} (SOC) is the OCV-SOC relationship which is obtained by experiments. The value of Δt depends on the sample rate of the system which for the WESS is nominally 1Hz but in reality this varies.

The input parameters of the DSPKF or the DEKF algorithm are sampled current and voltage data, the OCV-SOC relationship, battery Coulombic efficiency, measured capacity of the battery system, initial state and estimated equivalent circuit parameter values. The outputs of the algorithm are the system SOC and updated estimates of the equivalent circuit parameters.

The KF algorithms are implemented in Python, using packages numpy, math, time and pandas. The Python code consists of the data processing

part, the KF tuning part, and the KF equations. The KF equations include the equations Equations 4.1 to 4.3 (or Equations 4.4 to 4.6). Data processing is essential, which is importing the voltage and current data into the python code. Applying $f(\bullet)$ and $h(\bullet)$ and equations in table 4.1 or table 4.2 recursively, with the system parameters and the KF parameters stated above, the DSPKF or the DEKF can converge to provide an estimated battery SOC and ECM parameters.

4.2.2 From cell-level to system-level

In terms of the implementations of KF methods for SOC estimation, the difference between the cell-level and the system-level is mainly the OCV-SOC relationship and the values of ECM parameters, which can be very different. However, by understanding the internal structures of a battery system (the series-parallel relationships), the system-level (or rack-level) OCV-SOC relationship and ECM parameters can be calculated. The latter may not be accurate but it is only a reasonable initialisation and to be estimated by the weight filter.

Most results shown in this work use the scaled (as mentioned, according to the topology of the cells connected to form the battery) OCV-SOC relationship experimentally measured of a single LTO cell (shown in Figure 3.13). The system-level OCV-SOC relationship of the WESS was also experimentally captured as shown in Figure 3.14, and compared with the scaled one in Figure 4.2.

Cell-level ECM parameters are measured first for system level estimations at the end of each rest period, by conducting an EIS test. After obtaining the EIS results, curve fitting techniques are used to calculate values of the cell-level ECM parameters. Similar to the OCV-SOC relationship, system-level ECM parameters are calculated using the series-parallel relationships of the BESS (or the rack).

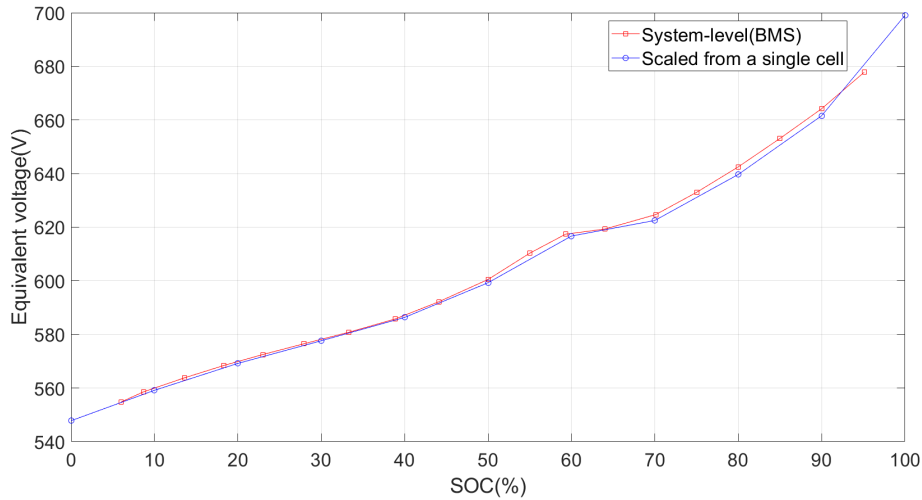


Figure 4.2: WESS OCV-SOC relationships: scaled from cell-level vs system-level.

Table 4.3: GA settings

Parameter	Value
Number of generations	10
No. individuals in a population	200
Selection operator	NSGAI
Independent probability for each attribute to be mutated	0.05
Crossover probability	0.5
Mutating probability	0.1
Fitness function 1	ABS(BMS SOC - DSPKF estimated SOC)
Fitness function 2	ABS(scaled R_s - DSPKF estimated R_s)

4.3 Genetic algorithm

The error covariance matrices for process noise (Q) and sensor noise (R) are an important selection for successful implementation of a DSPKF or DEKF [46]. Genetic Algorithms (GA) are excellent for solving searching and optimisation problems [120] and are viewed as a “universal optimiser”. The simplicity and ease of implementation allow, with careful selection of parameters, a good balance of exploration and exploitation of the search space. Whilst other heuristic techniques could be applied to this problem, finding the most efficient heuristic is out of scope of this thesis as the optimisation is only run once. Thus, in this work the DSPKF or DEKF parameters are automatically tuned by a GA using the Distributed Evolutionary Algorithm

in Python (DEAP) library.

The parameters include elements of process noise matrices in both state and weight filters, sensor noise, elements in error covariance matrices of both filters. The GA is multi-objective with two fitness functions defined and the non-dominated sorting genetic algorithm (NSGA-II)[121] is applied to select the Pareto front as candidates of the optimums. The first fitness function is designed to minimise the mean average error (MAE) between the DSPKF (or DEKF) SOC estimation and BMS SOC data known to be of acceptable accuracy (cycles that are known by experience of using the BESS not to cause large SOC discrepancies). The second fitness function is defined to minimise the error of the DPKF estimated R_s equivalent circuit parameter against the calculated value. Additional fitness functions to include other equivalent circuit parameters were investigated but no significant improvements beyond optimising for R_s were found.

The GA settings are shown in table 4.3. Note that these settings are not only for the GA of the WESS, but also for other batteries in this work. Besides, the values in the table are not unique and were discovered through trial and error using the experience of the users and tracking progress through generations. Specifically, the first 2 parameters, i.e., “Number of generations” and “No. of individuals in a population” are more significant and could be tuned based on the experience of the user. For example, for generating the process noise matrices of the weight filter, one with some knowledge of KF methods would not expect the values to be relatively large numbers: larger or close to 1. However other users without experience could extend the search space, in which case more individuals and generations are needed. Other parameters in the settings are also tunable and they mainly control the way the GA searches.

Because every time there are random numbers generated to be tried in a KF method, the GA results would not be the same. After running the GA, there are likely more than one set of optimal parameters for the KF method are obtained because this is a multi-objective optimisation problem. In these sets of parameters, a trade-off between the accuracy of SOC and R_s estimations is shown. Therefore, if SOC estimation accuracy is more

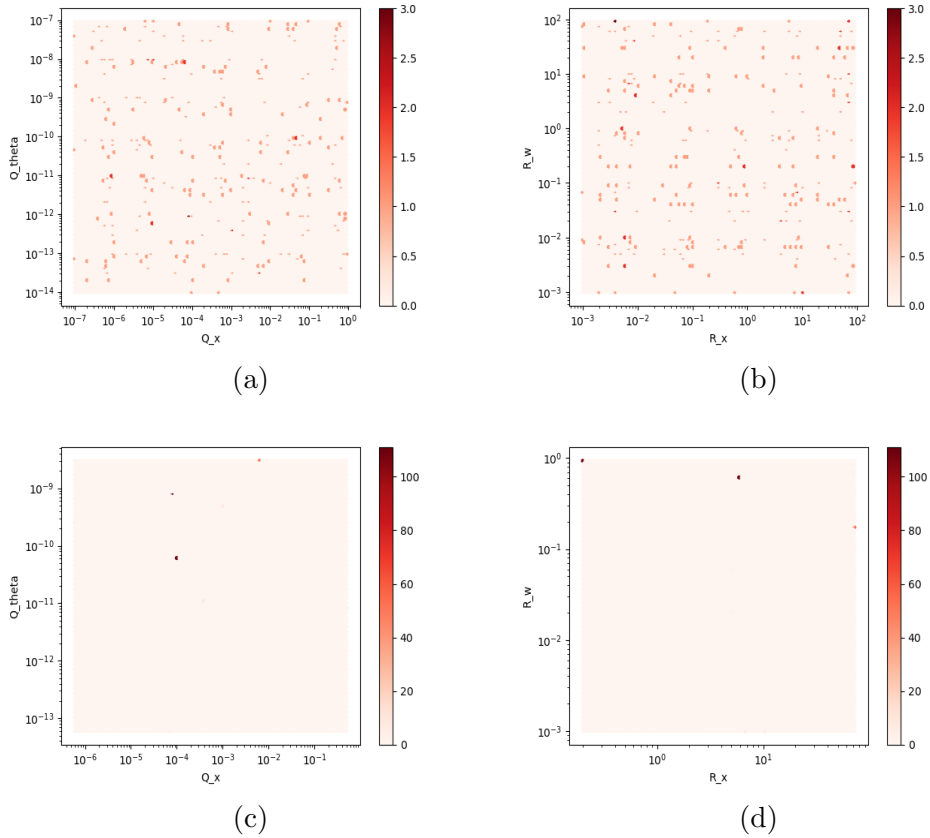


Figure 4.3: The evolution of GA for DSPKF: (a) Q values at the first generation, (b) R values at the first generation, (c) Q values at the 10th generation and (d) R values at the 10th generation.

important, the accuracy of R_s can be sacrificed to an acceptable extent, vice versa.

To avoid too large a population and too many generations, a combination of using GA tuned parameters and experiences, i.e., manually tuning are used. That is, after approximate values are obtained by GA, empirical knowledge can be used to decide the final parameters for the filters. Again, for a user with less experience, larger population and more generations can mitigate this problem.

Figure 4.3 illustrates how the GA converges in 10 generations for generating parameters of the DSPKF. Q_x and R_x are the parameters for the state

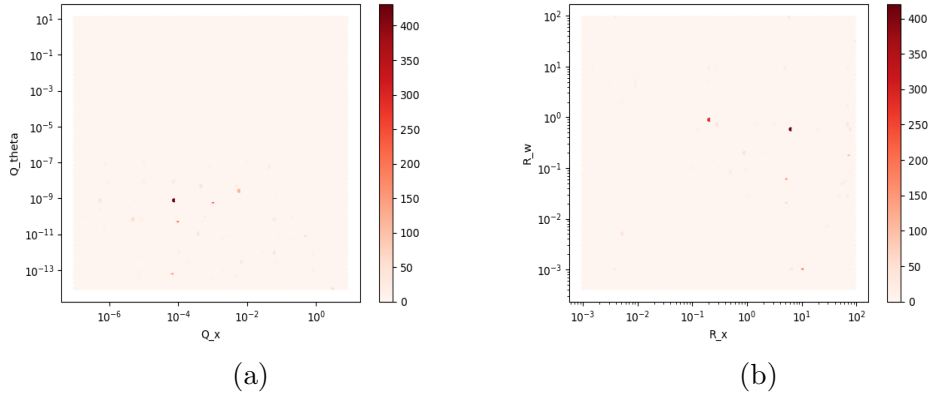


Figure 4.4: The evolution of GA for DSPKF: all generations together (a) Q values and (b) R values.

filter and the rest two are for the weight filter. It can be seen that the individuals are widely spread in the first generation while in the last generation there are only a few values that stand up, for both Q and R . The overall distribution is shown in Figure 4.4.

4.4 SOC estimation results

In this section, SOC results using KF methods are shown. This section starts with results of cell-level and rack-level, using the DSPKF. Most importantly, it shows the system-level results of KF algorithms, using both DEKF and DSPKF. Note that as discussed in section 4.2.1, KF SOC results are from the 1-RC ECM model for the LTO batteries and the 2-RC ECM model for other batteries.

4.4.1 Cell-level results

Cell-level SOC results are shown in Figure 4.5 and Figure 4.6 with two different profiles: OCV (data profiles shown in section 3.5.3) and EFR low (the EFR service applied when the grid frequency is lower than 50Hz). The data profiles of EFR low is also included in Figure 4.6. The SOC calculated by Coulomb counting is used as the reference to compare with the DSPKF

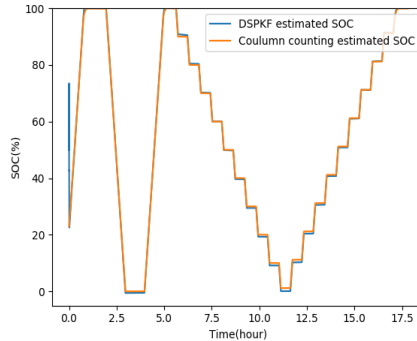


Figure 4.5: LTO cell SOC estimation results using the OCV data profile.

SOC. The Maccor battery tester has very accurate current sensors so the SOC calculated by Coulomb counting is considered to be ideal.

In Figure 4.5 and Figure 4.6, it can be seen that the DSPKF has very small errors with RMSEs of 0.88%, and 0.96% respectively. However, this thesis does not focus on cell-level state estimations, because as discussed above (section 2.5), cell-level SOC estimation has been achieved accurately by a range of methods. The accurate cell-level SOC estimation here is a verification of the DSPKF SOC algorithm since the equations and implementation are very similar between KF SOC algorithms at both cell and system levels.

4.4.2 Rack-level and a small battery system results

The SOC results of the GS Yuasa rack and the GS Yuasa battery system are shown here together because they share the same cells and modules. The latter is just about 3 times larger (section 3.3). The data profile used for the GS Yuasa rack is for OCV estimation, but it is different from the method introduced in this thesis. The idea is to use a very small current ($C/20$) cycle the battery so that the voltage at corresponding SOC is seen as the OCV [122]. The data profile used for the GS Yuasa system is shown in Figure 4.7. The DSPKF parameters are tuned by the GA and are the same for both the rack and the GS Yuasa system. ECM parameters, and the system-level OCV-SOC relationship are scaled from the cell-level experimental results of

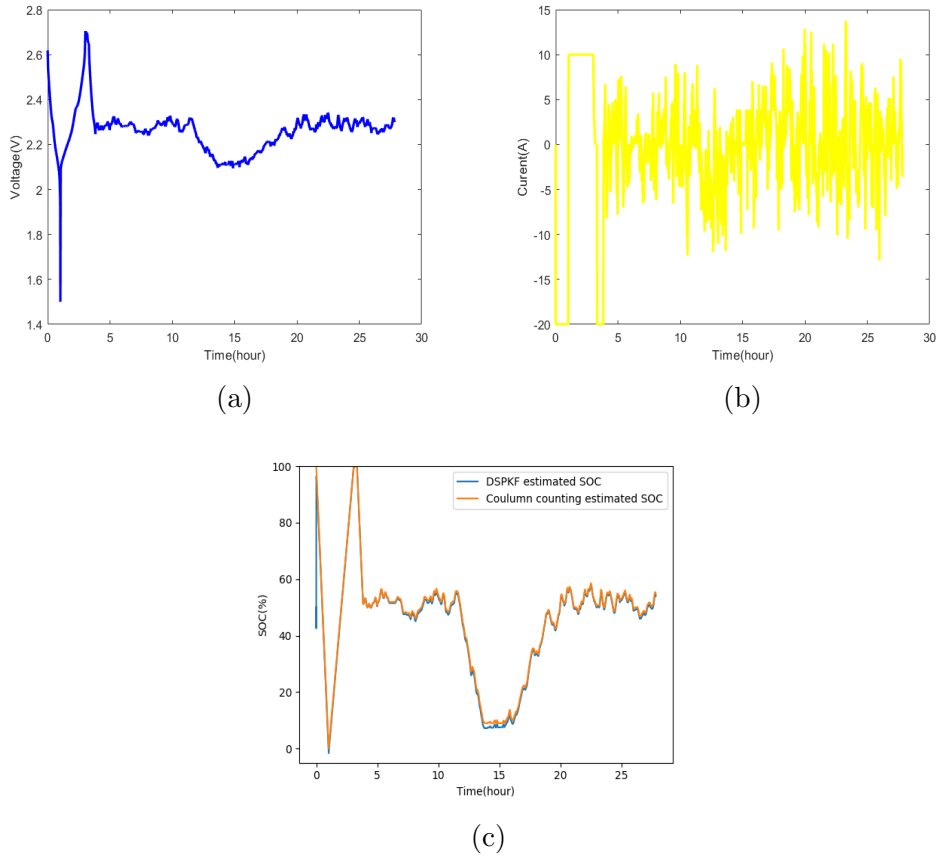


Figure 4.6: LTO cell SOC estimation results with an EFR low profile (a) cell voltage, (b) cell current and (c) SOC estimation results.

a GS Yuasa cell inside them.

The results in Figure 4.8a of rack-level SOC estimation show that implementing cell-level techniques to the system-level is promising. The RMSE between the DSPKF SOC and the BMS SOC is 4.06%. The RMSE is larger than the cell-level's but as discussed above (section 3.3), the BMS SOC has limitations. Besides, the test was conducted with constant current so the DSPKF SOC is preferred for the rack-level SOC estimations. Although the rack used here has all cells in series, it still can be considered to be a small battery system and has a more complex structure than a single cell.

In Figure 4.8b, the DSPKF estimated SOC is compared with the BMS SOC in the ADEPT BESS, with a RMSE of 1.51%. Therefore as a larger

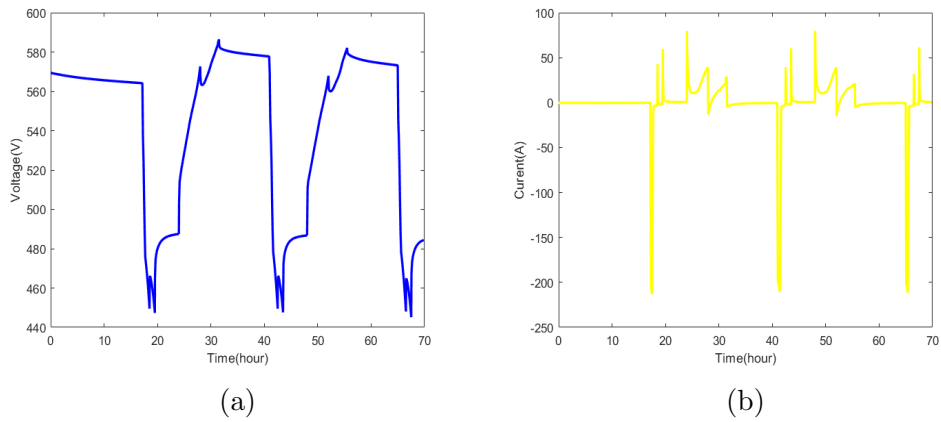


Figure 4.7: GS Yuasa BESS short data profile (a) voltage and (b) current.

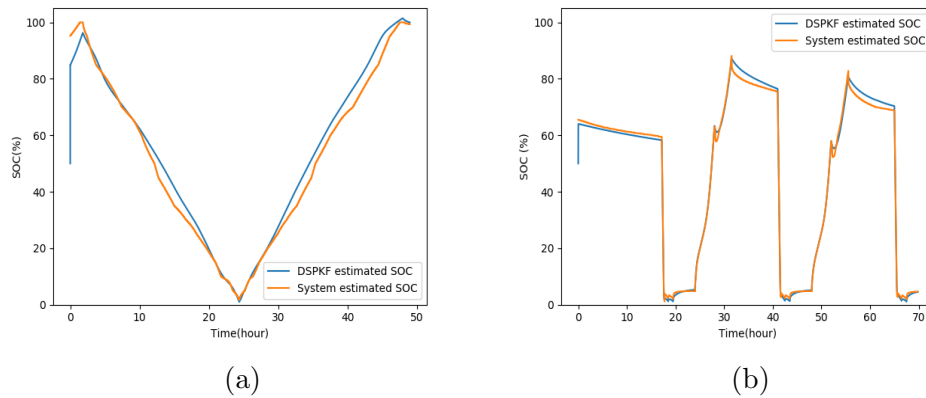


Figure 4.8: DSPKF SOC results of (a) a GS Yuasa rack and (b) a GS Yuasa battery system.

system the match between the two are even closer than the Yuasa rack and the DSPKF, supposing there is a better BMS SOC. For the GS Yuasa battery system, further comparison of the two SOC estimations through capacity estimation results will be discussed in the next chapter.

4.4.3 System-level results

Figure 4.9 shows the WESS SOC estimation results of constant cycling, the mixed profile and grid frequency response service (profile shown in section 3.5). The DSPKF and BMS results are a good match with the RMSEs

calculated to be 1.38%, 1.36% and 0.44% respectively. In Figure 4.9a and Figure 4.9b, the DSPKF and BMS estimated SOC are very close because the two datasets are with almost constant current. In Figure 4.9c the differences are larger because the BESS is delivering DFR (fluctuating load), with various and fast-changing current values, so the BMS fails to provide accurate estimations (demonstrated chapter 5). The SOH of the system will affect the SOC estimation accuracy significantly (equation 2.2). For the shown SOC results, η is assumed to be 100% [123], and the SOH is set to 100% since the WESS's SOH is currently still very high and the degradation is too small to measure (detailed in chapter 5).

In Figure 4.10, the results of the DEKF are compared with the BMS SOC with the same data profiles, and the RMSEs are 3.33%, 2.01% and 0.81% respectively. It can be seen that the DSPKF is closer to the BMS SOC. Further comparison between the BMS SOC and DSPKF SOC is presented in section 4.5 and chapter 5.

The DSPKF SOC results with constant cycling data of using the system-level experimental OCV-SOC relationship (illustrated in Figure 4.2), are shown in Figure 4.11. It can be seen that these DSPKF results are very close to the BMS SOC ones with a RMSE of 0.84%, closer than the DSPKF SOC using the OCV-SOC relationship scaled from the cell-level. This is because the system-level relationship is measured according to the BMS SOC. This is the reason why most DSPKF SOC results shown in this work are from the cell-level OCV-SOC relationship, which can be obtained accurately. However, these results have shown that both ways for the system-level OCV-SOC are possible.

The DSPKF SOC results with constant cycling data of using an ECM model with two RC-branches are shown in Figure 4.11a. It can be seen that the results are very similar to the ones using only one RC-branch, with an RMSE of 1.34%. Therefore, there is no significant improvement on SOC results using two RC-branches for LTO batteries, which validates the assumption that has been made above (section 4.2.1).

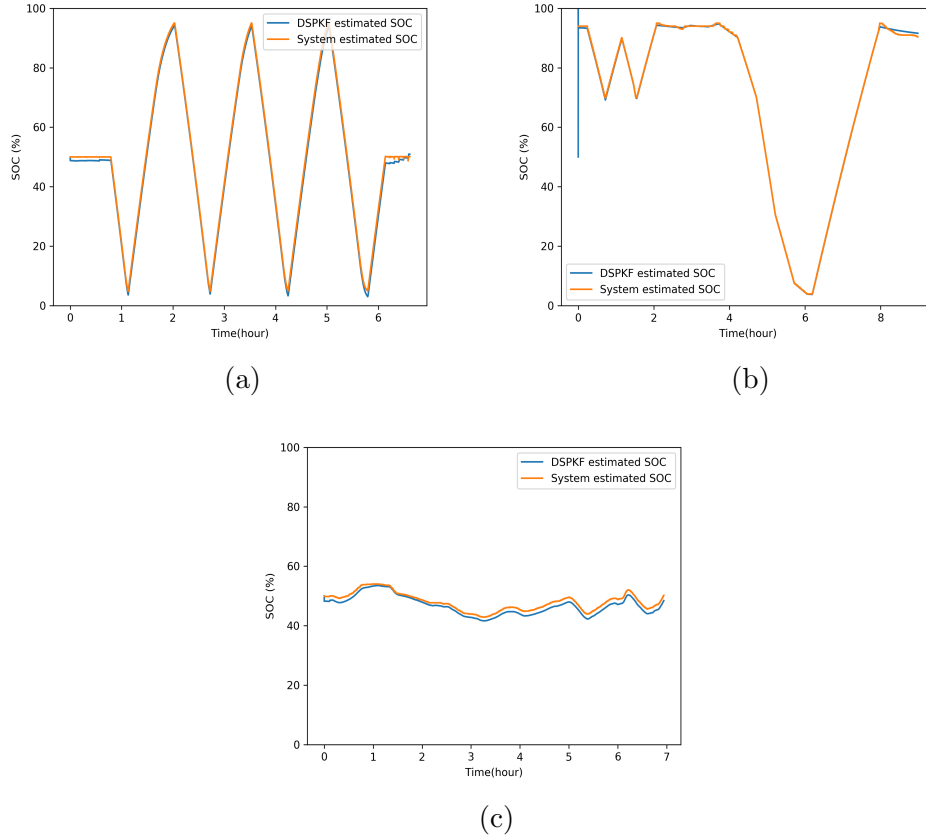
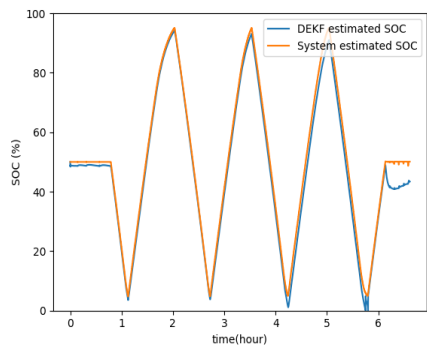


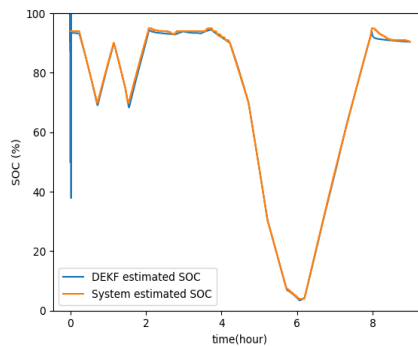
Figure 4.9: WESS DSPKF SOC estimation results of (a) constant cycling, (b) mixed profile and (c) dynamic frequency response.

4.5 Comparison of WESS efficiency calculation using DSPKF SOC and BMS SOC

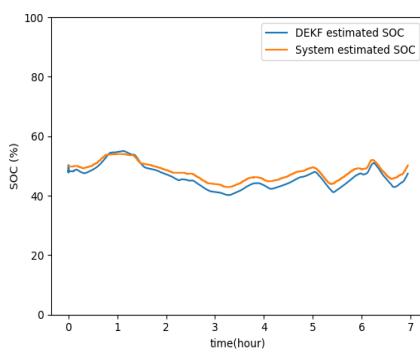
The round trip efficiency (RTE) of a battery system is one of the essential characteristics the owner of a BESS would like to know. RTE is closely related to the operating cost of the system so that the system operation can be optimised to avoid inefficient operation. For example, if the actual RTE of a BESS is 94%, while the owner thought it was 97%, the owner may make wrong decisions during energy trading because some extra cost due to actually lower RTE is not considered. In this section, round trip efficiency of the WESS is calculated using system-level current, voltage and SOC estimations.



(a)

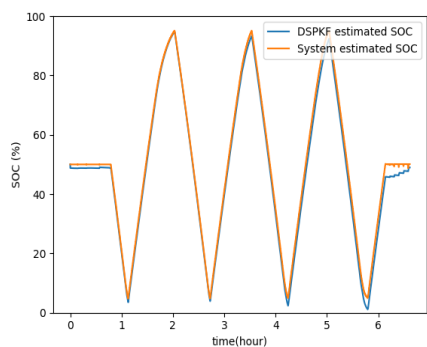


(b)

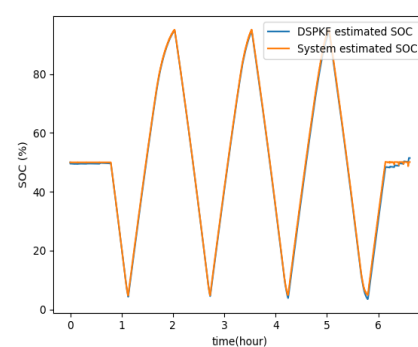


(c)

Figure 4.10: WESS DEKF SOC estimation results of (a) constant cycling, (b) mixed profile and (c) dynamic frequency response.



(a)



(b)

Figure 4.11: WESS DSPKF SOC estimation results of using (a) an ECM with 2-RC branches and (b) system-level OCV-SOC relationship.

Different sources of SOC estimations, i.e., BMS SOC and DSPKF SOC are compared with RTE results. Also, the effects of C-rate and SOC on battery system efficiency are investigated. Battery efficiency, inverter efficiency and the efficiency of the whole system are calculated and discussed. It is shown how the DSPKF SOC as an input with increase accuracy compared with the BMS SOC, can improve the RTE estimation results of both the battery and the whole system.

4.5.1 Methodology

The round trip efficiency, η_{RT} of a system is the quotient of the exported energy, E_{out} , and the imported energy, E_{in} , as shown below:

$$\eta_{RT} = \frac{E_{out}}{E_{in}} \times 100\% \quad (4.7)$$

Energy is calculated by integrating power, as shown below:

$$W = \int_a^b P dt \equiv P \Delta t \quad (4.8)$$

where W is the the transferred instantaneous energy in Joules, P the instantaneous power, and a and b are the adjacent timestamps. For the WESS, P is obtained from the product of dc-link voltage and current for the battery, the product of inverter voltage and dc-link current for the inverters, while for the whole system it is measured directly by the power metres. The RTE is calculated for each cycle, where the battery is discharged from an SOC value and charged back to the same SOC, or vice versa. Therefore, SOC data is needed and the BMS SOC is used in [124].

The E_{out} and E_{in} in equation 4.7 are calculated by summing energy values in each cycle, as shown in equation 4.9,

$$E_{out/in} = \sum_{n=1}^m W_n \quad (4.9)$$

where W_n is the number of instantaneous energy value.

The final efficiency calculations of the battery, the whole system and the inverters are shown below:

$$\eta_{battery} = \frac{E_{battery_out}}{E_{battery_in}} \times 100\% \quad (4.10)$$

$$\eta_{system} = \frac{E_{system_out}}{E_{system_in}} \times 100\% \quad (4.11)$$

$$\eta_{inverter_in} = \frac{E_{inverter_in}}{E_{system_in}} \times 100\% \quad (4.12)$$

$$\eta_{inverter_out} = \frac{E_{system_out}}{E_{inverter_out}} \times 100\% \quad (4.13)$$

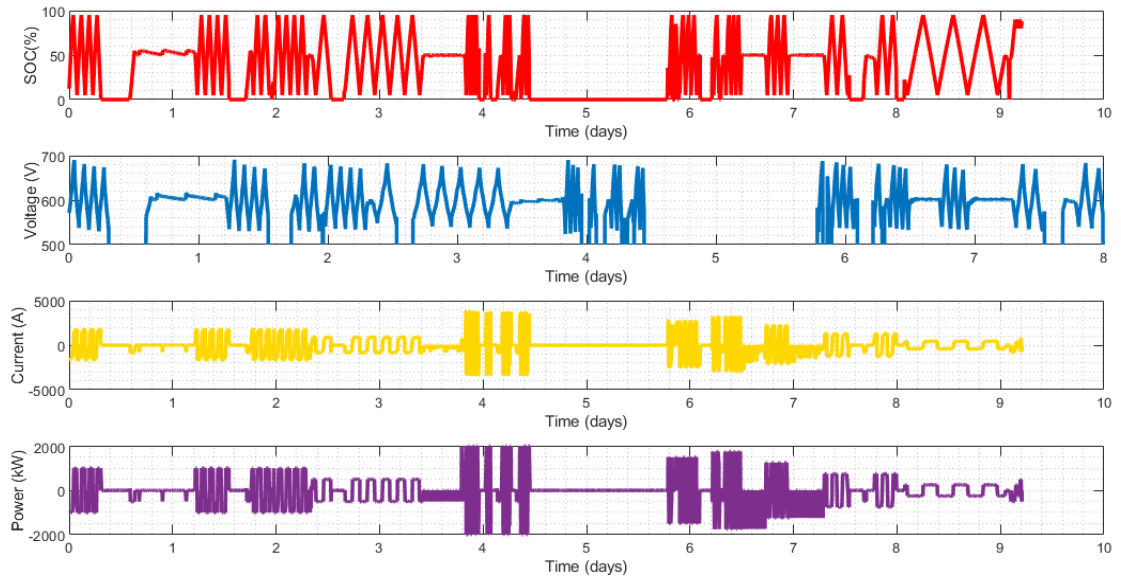
where “out” stands for discharging and “in” for charging. Note that there is no “round trip efficiency” for inverters since they are not storage devices, so there are 2 parts of inverter efficiencies.

In [124] and this work, the efficiencies of the battery, the inverters and the whole system of the WESS are calculated based on experimental data.

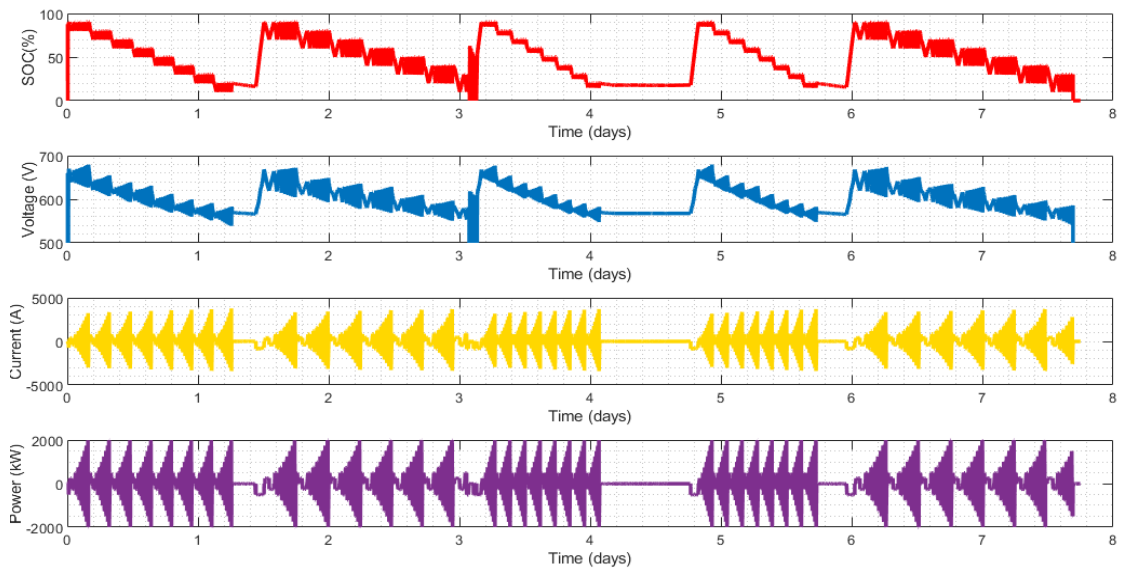
The efficiency data are shown in Figure 4.12. Test 1 is cycles from 5% SOC to 95% SOC at different C-rates, from 0.25C to 2C, with an interval of 0.25C, and at each C-rate the system was tested at least 3 cycles. Test 2 investigated the effects of different DoDs, namely 5%, 10% and 20% at different SOC, from 20% to 90% on system RTE. At each SOC value, a cycle started with a discharge, followed by a charge back to the SOC value, with one of the DoDs carried out, and repeated for 8 times. Evidently at 90% SOC, the 20% DoD test cannot be carried out so only 5% and 10% DoDs were conducted.

To ensure the quality of the data that are used for calculation, some data cleansing techniques are used in this thesis [124]. Firstly, the data for calculation are chosen when the battery is not idle to make sure there is energy transferred. Secondly, transient parts are discarded to avoid inaccurate data.

In this work, as the DSPKF SOC is available to be used, the RTE results using DSPKF SOC and BMS SOC are compared. This is not only to obtain more accurate efficiency estimation results, but also to compare the accuracy



(a)



(b)

Figure 4.12: WESS tests for round trip efficiency calculations (a) test 1 and (b) test 2.

of DSPKF SOC and BMS SOC.

4.5.2 Efficiency results

From Figure 4.13 to Figure 4.20, RTE results using DSPKF SOC is shown first, followed by results using BMS SOC.

In Figure 4.13 and Figure 4.14, the RTE results of the battery show the trend that the RTE is in close relationship with C-rate, but not DoD or SOC, i.e., larger C-rate is less efficient. In Figure 4.13b and Figure 4.14b the results using the BMS SOC can show the trend between RTE and C-rate, but they show significant fluctuations. For example, in Figure 4.13b, a number of points make the trend inconsistent, especially the peak at 0.5C & 10% DoD. In Figure 4.14b, the fluctuations are more evident, one needs to spend more time to find the effects of C-rate and SOC on RTE results. While in the results of using the DSPKF SOC, the relationship between the RTE and C-rate is more clear, and the results at the same DoD and SOC are more consistent compared with the counterparts using the BMS SOC. Moreover, in both figures, the values of RTE using BMS SOC sometimes are larger than 100%, which is not reasonable. More specifically, in Figure 4.13b, the results at 0.5C & 10% DoD and 0.25C & 5% DoD are over 100%. In Figure 4.14b, there are 3 points at 0.5C are over 100%. However, in the results of using the DSPKF SOC, the values of RTE are all below 100%.

In Figure 4.15 to Figure 4.18, it can be seen that the inverter efficiency is again in close relationship with the C-rate but not the DoD or SOC. Also, the choice of DSPKF SOC or BMS SOC does not make a difference to the accuracy of inverter efficiency calculations as the results are very similar. Using DSPKF SOC cannot solve the problem that some efficiency results are higher than 100%, as shown in the inverter export efficiency results (Figure 4.17 and Figure 4.18).

As for the results of the efficiency of the whole system, as per Figure 4.19 and Figure 4.20, again the C-rate dominates the trends of RTE results, while not starting SOC or DoD. Affected by inverter efficiencies, the system RTE peaks at 0.75C. For the improvements of accuracy by using DSPKF SOC,

they are similar to the counterparts in the battery RTE results: the trend of the effect of C-rates is more clear and consistent, and the values are more reasonable since in Figure 4.20b some results from BMS SOC are close to 100%.

4.5.3 Summary

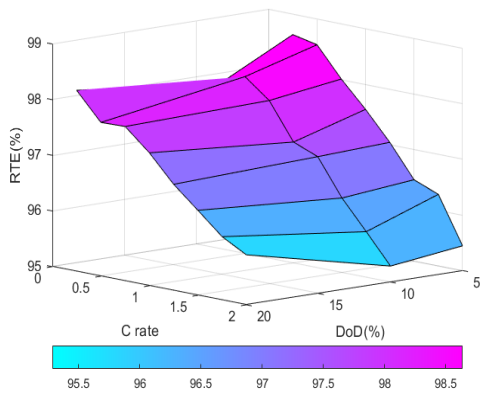
This section demonstrates how to calculate the efficiency of the battery, inverters and the whole system of the WESS. The DSPKF SOC as one of the essential inputs for the algorithm, compared with the efficiency results using the BMS SOC in a previous work. The first finding is that according to efficiency results the DSPKF SOC seems to outperform the BMS SOC, which will be discussed more in the next chapter. Secondly, using the DSPKF SOC can improve the accuracy of efficiency calculations. Besides, it further proves that the C-rates are the main factor that affects the efficiency of the battery system.

4.6 Dealing with invalid data for BESS SOC estimation

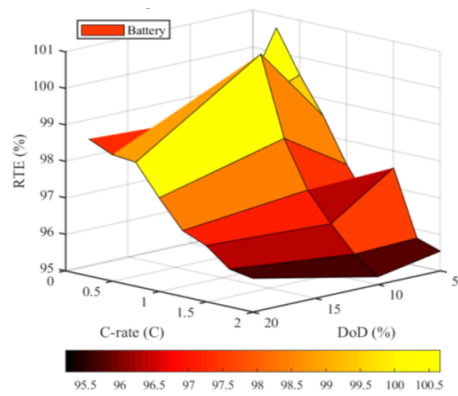
The data of the WESS is sometimes invalid, meaning that during these periods the current, voltage and BMS SOC are each shown as zeros. This can cause a problem where the KF that is estimating SOC or SOH diverges when the voltage and current values each read as zero and continue for a sustained period. The reasons for invalid data are as follows:

- A problem of data connection but the battery is still operating.
- The data connection is working but the battery is offline.
- Both the data connection and the battery are offline.

During the invalid data periods, the EKF and DSPKF algorithms' accuracy is impacted from when the invalid data periods start, as shown in

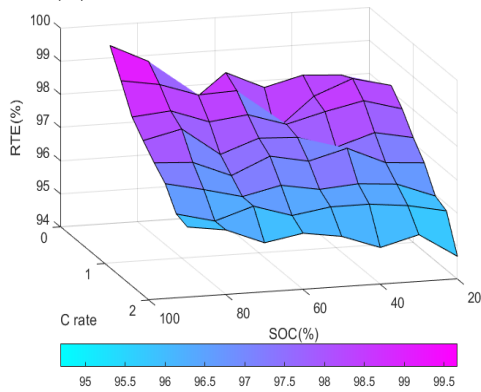


(a)

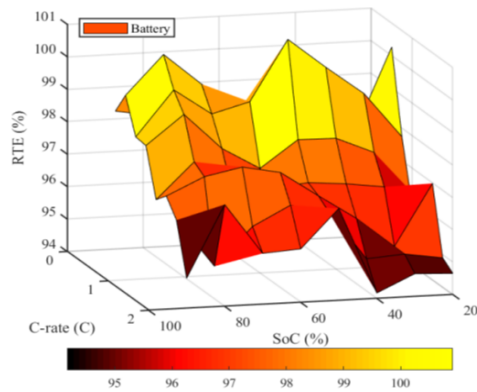


(b)

Figure 4.13: Battery RTE against C-rate and DoD, using (a) DSPKF SOC and (b) BMS SOC.

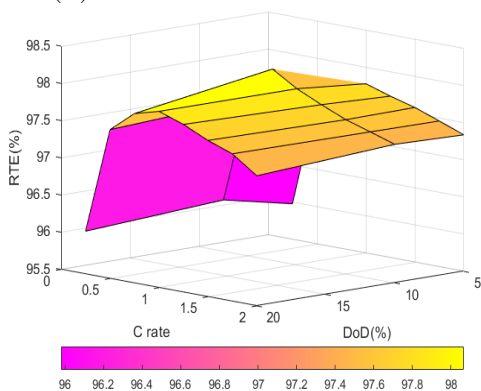


(a)

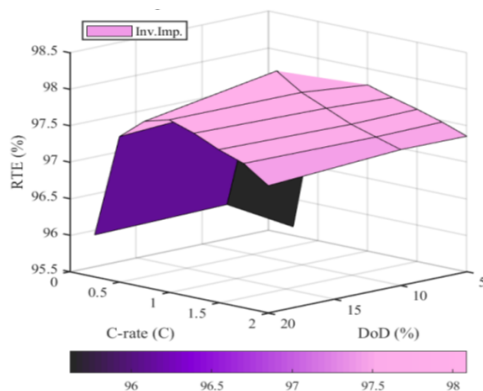


(b)

Figure 4.14: Battery RTE against C-rate and SoC, using (a) DSPKF SOC and (b) BMS SOC.

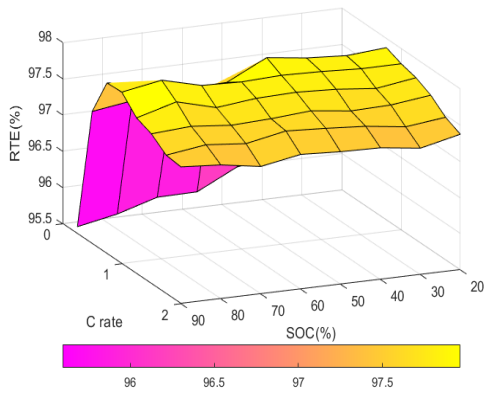


(a)

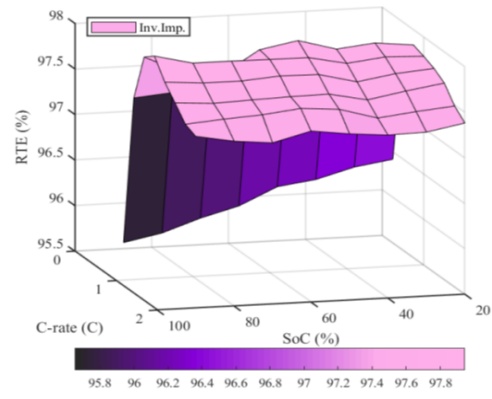


(b)

Figure 4.15: Inverter import efficiency against C-rate and DoD, using (a) DSPKF SOC and (b) BMS SOC.

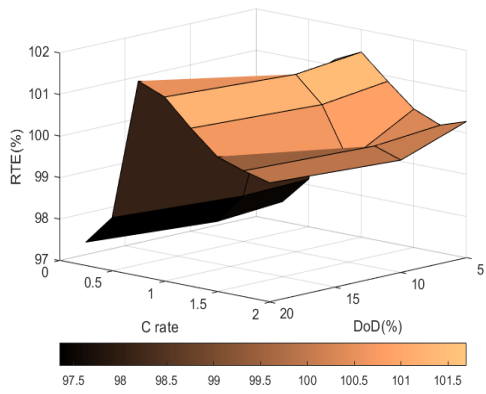


(a)

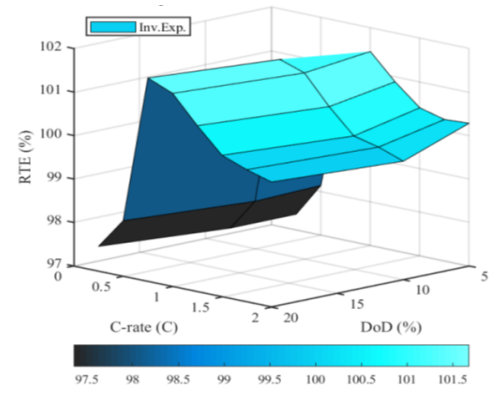


(b)

Figure 4.16: Inverter import efficiency against C-rate and SOC, using (a) DSPKF SOC and (b) BMS SOC.

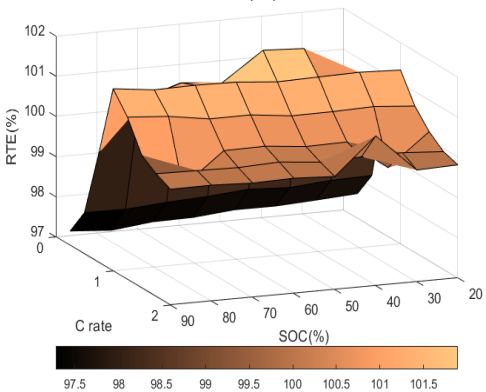


(a)

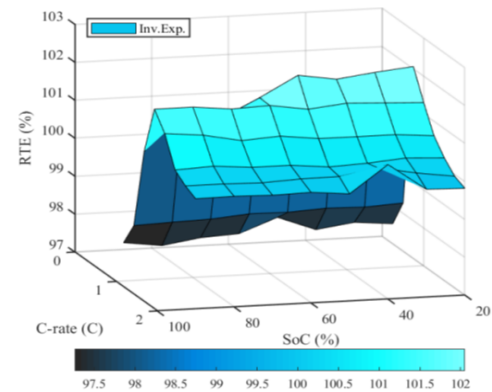


(b)

Figure 4.17: Inverter export efficiency against C-rate and DoD, using (a) DSPKF SOC and (b) BMS SOC.

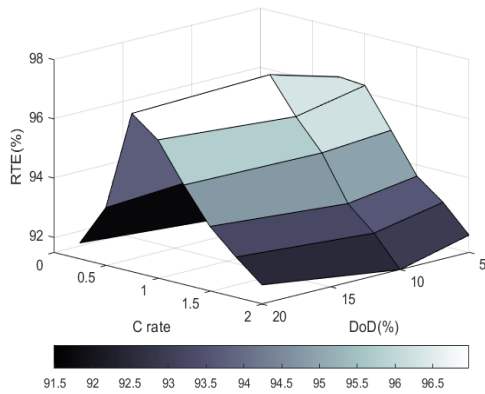


(a)

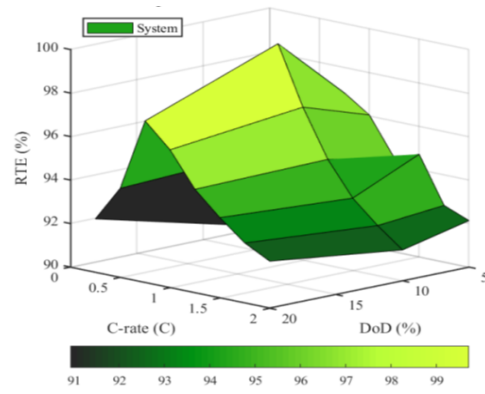


(b)

Figure 4.18: Inverter export efficiency against C-rate and SOC, using (a) DSPKF SOC and (b) BMS SOC.

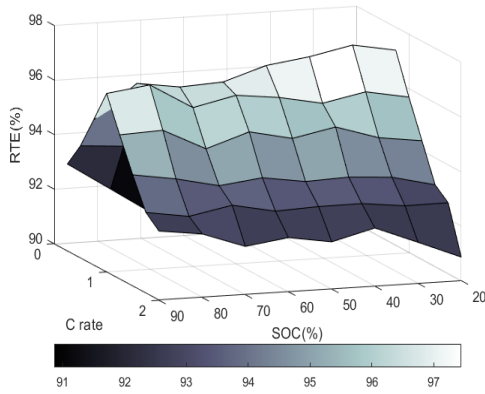


(a)

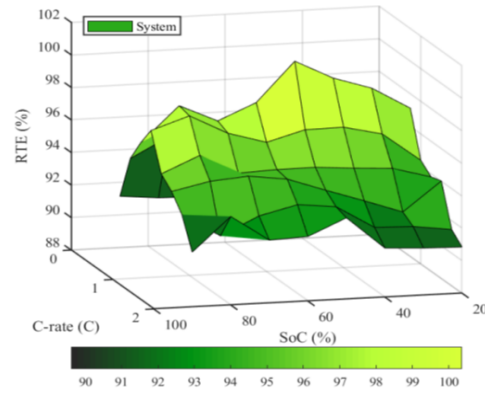


(b)

Figure 4.19: System RTE against C-rate and DoD, using (a) DSPKF SOC and (b) BMS SOC.



(a)



(b)

Figure 4.20: System RTE against C-rate and SOC, using (a) DSPKF SOC and (b) BMS SOC.

Figure 4.22 and Figure 4.23. Therefore, making sure the algorithm is able to converge after invalid data is the aim of this section.

4.6.1 Methodology

The methods in the literature [125] for when invalid data is the input to a KF mostly concern control and communication, and they often treat the invalid data as a Bernoulli process (i.e., a finite or infinite sequence of binary random variables). As it is evident that the data of the WESS does not follow a

Bernoulli process, methods should be tried using empirical knowledge. There are several methods that could solve this problem:

- Use the previous sample point to fill the invalid sample points;
- Pause the KF algorithm, use the last estimation and resume estimating once valid data is received again;
- Limit the estimated SOC values, as the actual SOC values must be between 0% and 100%, to avoid divergence;
- Apply curve fitting using previous sample points to predict the SOC values during the invalid data period.

The first step is to detect the invalid data periods. When the voltage drops to 0, an invalid data period starts. Likewise, when it returns to within normal operating bounds the invalid data period ends. The voltage differential, dV/dt , which is set to be ± 400 for the WESS is used in the algorithm to detect these periods. It is only a number large enough to detect the beginning and the end (rising and falling edges) of an invalid data period.

Using previous sample points means that during an invalid data period, all the invalid data are replaced by the last data point (voltage and current) before the invalid data period. This makes the KF algorithm continue working without divergence, based on the fact that although the data used during this period are not actual data, the actual data are not known, and the KF algorithm can fast converge once the actual data are fed in once the invalid data period finishes. Pausing the KF algorithm is to make the KF algorithm skip the invalid data, once the start of an invalid data period is detected, and allow data to be used in the KF algorithm once the end of an invalid data period is detected. As for the third method, limiting the estimated SOC values, any SOC estimations during an invalid data period that may be smaller than 0% or larger than 100% are forced to be 0% and 100% respectively. This method may be combined with the first two methods since when the estimations reach the boundaries, i.e., 0% or 100%, divergence already occurs. The last method is to use the last 20 data points before the invalid

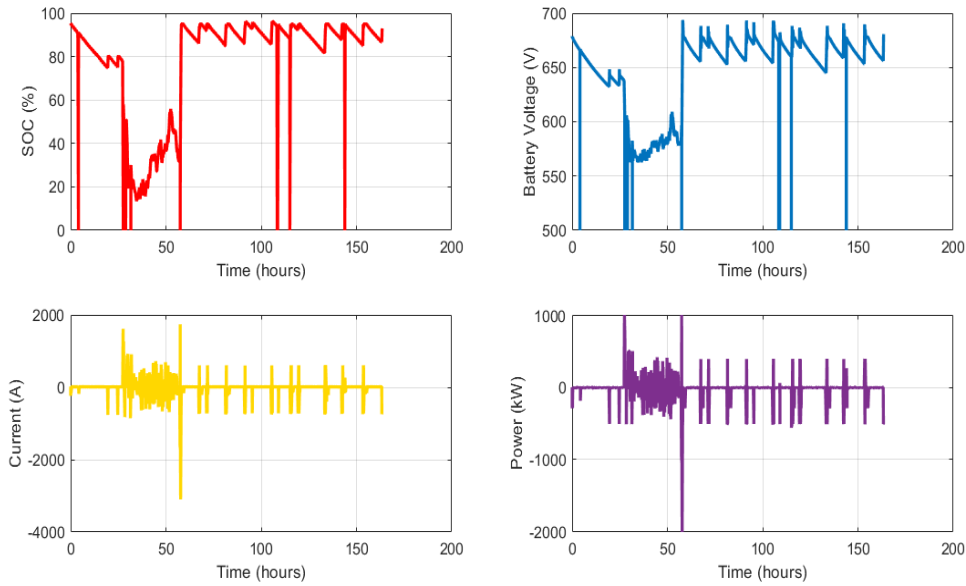


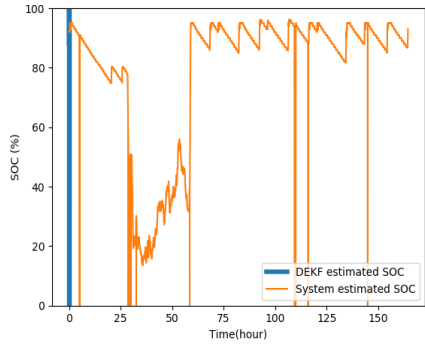
Figure 4.21: WESS operation data profile for investigating invalid data.

data period, to predict the data points during this period. It is done with a moving window, i.e., the predicted data points replace the data point at the beginning of the 20 data points that are used for curve fitting.

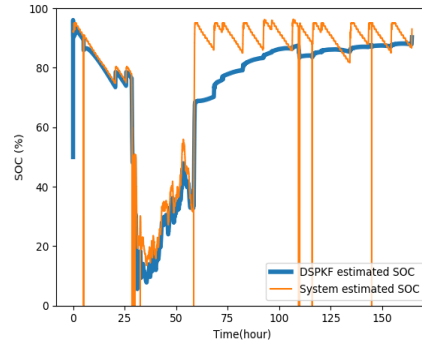
4.6.2 Results

SOC estimation results with the impact of invalid data and the effectiveness of invalid data techniques are shown in Figure 4.22 and Figure 4.23, using data shown in Figure 4.21. In Figure 4.21, it can be seen that there are several invalid data periods in this profile. In Figure 4.22a, the DEKF diverged since the first invalid data period as the estimation started to be minus, and it did not converge again after that as there are no estimates on the figure (which means the estimates of SOC are not within the range of 0% and 100%). In Figure 4.22b, it can be seen that the effects of invalid data are smaller for the DSPKF, but still result in some divergence, and the SOC estimation did not converge after invalid data periods because the weight filter that estimates parameters diverged.

In Figure 4.23a and Figure 4.23b, and Figure 4.24a, the SOC estimation results match well with the BMS SOC, without the effects of invalid data.

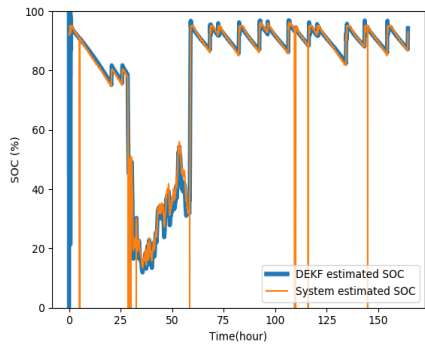


(a)

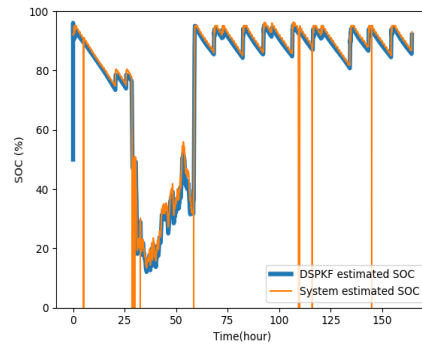


(b)

Figure 4.22: SOC estimation results affected by invalid data (a) DEKF SOC and (b) DSPKF SOC.

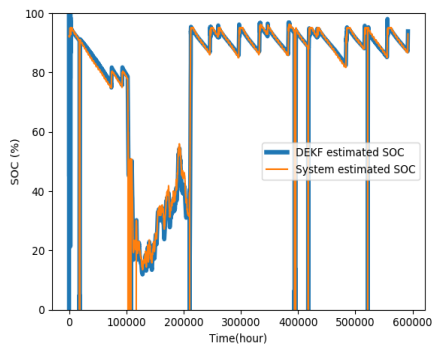


(a)

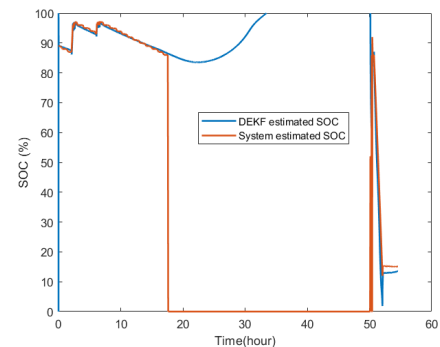


(b)

Figure 4.23: SOC estimation results after using previous data during invalid data periods (a) DEKF SOC and (b) DSPKF SOC.



(a)



(b)

Figure 4.24: DEKF invalid data results with other methods (a) pause the algorithm and (b) curve fitting.

The RMSEs are 2.36% (DEKF using the first method), 1.51% (DSPKF using the first method) and 4.41% (DEKF using the second method) respectively. This is because one of the first two methods is used, together with method three (limiting the SOC). The reason of using one of the first two methods is that they have the same effects to the filter and it can be seen that results in Figure 4.23a and Figure 4.24a are similar. If the data starts with invalid data, the SOC estimation should be set as an arbitrary value between 0% and 100% because neither previous estimation or previous data points are available. Using method three (limit SOC range) only is effective but it needs more time to converge after invalid data periods than the previous methods. This also applies to other circumstances when the calculated SOC is not in this range, which may be due to some very rare erroneous data where there is a time jump after restarting the BESS, the SOC value should be forced back to the reasonable range stated above to avoid further divergence.

The curve fitting method was tried too with SOC limitation using DEKF. The results in Figure 4.24b show that the filter still diverges and will exceed the boundaries without SOC limitation. The reason it can converge after the very long time of invalid data is because the SOC is bounded so that any values that larger than 100% are forced to be 100%. The computation time of the algorithm using the curve fitting method is longer than the first two methods due to increased number of calculations. This is exaggerated when there is a very long period of invalid data.

4.6.3 Summary

The main problem to solve is that the KF diverges when invalid data happens (both voltage and current values received are 0) if no methods are used, and it may not be able to converge again after the invalid data. It has been shown that Kalman filtering can converge well after the invalid data using the simplest methods. In addition, the length and frequency of the invalid data period do not affect the results of the simple methods. These methods can eliminate the effects of invalid data easily because of the excellent convergence ability of the KF, as long as the previous SOC estimation is forced to be

within the reasonable range, i.e., not being negative or larger than 100%.

In conclusion, there are two effective steps to make sure the KF remains converged 1) using the previous data simply when the data is invalid, or maintain the last SOC estimation before invalid data occurs 2) bounding the SOC. The DEKF and DSPKF SOC estimation algorithms are running online (in real-time) for the WESS and have shown robust results against invalid data.

4.7 Conclusion

In this chapter, SOC estimation of large-scale BESS has been discussed using KF methods. The SOC estimation results are shown from cell-level, rack-level, to system-level. As the state of art of KF family, most results shown are from a DSPKF algorithm and WESS SOC results of the DEKF algorithm are also shown. The algorithm takes the system-level current and voltage data while using a cell-level ECM model. It also takes the results of a cell-level EIS test to initialise the weight filter. As for the OCV-SOC relationship, either a system-level measured or the one that scaled from the cell-level experiment works. The KF algorithms are tuned by a GA algorithm automatically to achieve repeatable results for other BESSs. To show the successful implementation of the DSPKF algorithm, the DSPKF SOC results are first compared with the BMS SOC. The measured SOC has been imported into an algorithm of WESS efficiency calculation. Because the RTE results of using DSPKF SOC outperform the ones using BMS SOC, it indirectly proves the DSPKF SOC outperforms the BMS SOC. To obtain such reliable KF SOC estimations, several techniques have to be used to deal with the invalid data problem.

Chapter 5

Capacity and SOH estimation of large-scale battery systems

5.1 Introduction

Apart from SOC, battery capacity / SOH is another essential state that one needs to know to best utilise the battery. As an example, for an electric car, as the battery degrades the distance it can travel on one charge decreases. In time, the distance capability will no longer be acceptable to the driver and therefore, it should be the time to either replace the battery or the whole car. For a large-scale battery system, degradation will result in reduced profits under arbitrage and possible performance penalties when providing frequency response services as the battery will be unavailable more often due to reaching SOC limits.

As an example of battery degradation, the degradation of the CHAM cell is illustrated in Figure 5.1. In Figure 5.1a the ageing of the cell is shown with discharge capacity while in Figure 5.1b it is shown as nominal capacity (discharge capacity of the first cycle is the reference). The cell is cycling within a voltage range between 3V and 4.12 V (for better cycling life [126]), at a temperature of 35 °C. After every 200 cycles the test is paused, and this is the reason there are some capacity fluctuations in the results.

TLS implementation on large-scale systems is introduced in this chapter,

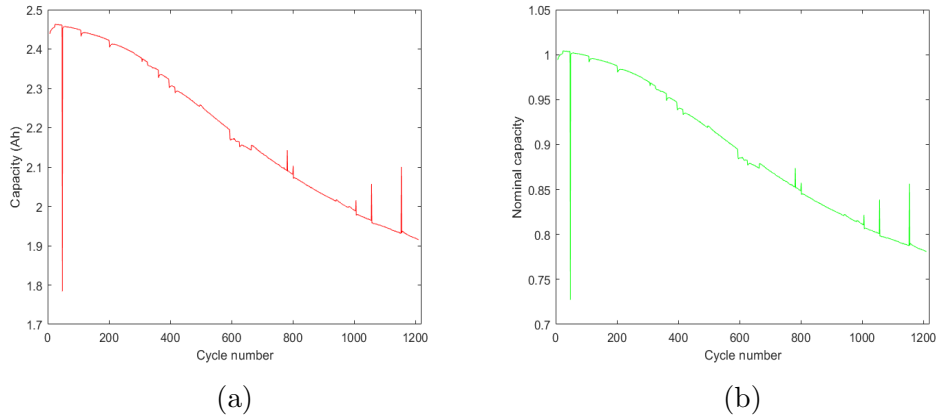


Figure 5.1: Degradation of the CHAM cell (a) degradation shown as discharge capacity and (b) degradation shown as nominal capacity.

and the algorithm is again tested starting at the cell-level, then rack-level and finally at the system-level. A variant of the TLS algorithm is also introduced using the system-level power data, instead of the current data. An almost full capacity test using Coulomb counting is possible if the system is not providing any services. Thus, the TLS estimated capacity can be compared with the reference capacity from Coulomb counting.

Although SOC and capacity algorithms are introduced in separate parts, they are closely related and their estimation accuracy is significantly affected by each other. Specifically, in the basic equation of the TLS algorithm (equation 5.1), the change of SOC is the denominator, while in the KF SOC algorithms, the capacity is an essential parameter. At a specific SOC, a different amount of energy is stored in a brand new battery compared to an aged one.

In the TLS algorithm, current integration and SOC variation are the values that affect capacity estimation results. In this chapter, TLS capacity estimation results of using BMS SOC and DSPKF SOC are compared, using long-time data up to a year. Online capacity estimation is also achieved to monitor the battery system's health.

Compared with cell-level capacity estimations, system-level capacity estimations are challenging. This is mainly because the system-level data (current and voltage) are generally less accurate than that which can be obtained

for cell-level testing from laboratory-grade equipment. To mitigate this issue, data selection needs to be conducted to make sure the data provided for the TLS algorithm are of high quality. Unlike SOC, capacity is not fast-changing, which makes data-selection possible.

The data used in this chapter to demonstrate capacity estimation algorithms are from the NMC cells, the Yuasa rack, the GS Yuasa BESS, the WESS and they are introduced in chapter 3.

5.2 TLS implementation on large-scale battery systems

5.2.1 TLS algorithm

Battery capacity can be estimated by total least-square based methods [94] by using the relationship between the variation of SOC and current integration, as shown below:

$$\int_{t_1}^{t_2} \frac{-\eta I(\tau)}{3600} d\tau = Q(SOC(t_2) - SOC(t_1)) \quad (5.1)$$

where η is again the Coulombic efficiency and assumed to be 100%, I the charge or discharge current and Q is the capacity value that needs to be calculated. This equation is based on equation 2.6, the only difference is that it refers to the condition when a full discharge is not available.

For the simplicity of calculation:

$$y = \int_{t_1}^{t_2} \frac{-\eta I(\tau)}{3600} d\tau \quad \text{and} \quad x = SOC(t_2) - SOC(t_1) \quad (5.2)$$

The total least squares (TLS) method is used in this work, which assumes errors in both y and x data, but the error variances are proportional. Therefore, $\sigma_{y_n}^2 = k^2 \sigma_{x_n}^2$. The equations below show the iterative calculations of TLS. The data is divided into n segments to do the recursive calculations, $\sigma_{y_n}^2$ the error variance in y of every segment and $\sigma_{x_n}^2$ is the error variance in x of every interval. They are guesses of the errors on y and x respectively.

The equations below show the iterative calculations of the method [94].

$$\begin{aligned}
c_{1,n} &= c_{1,n-1} + \frac{x_n^2}{\sigma_{y_n}^2}; \\
c_{2,n} &= c_{2,n-1} + \frac{x_n y_n}{\sigma_{y_n}^2}; \\
c_{3,n} &= c_{3,n-1} + \frac{y_n^2}{\sigma_{y_n}^2};
\end{aligned} \tag{5.3}$$

$$\hat{Q}_n = \frac{-c_{1,n} + k^2 c_{3,n} + \sqrt{(c_{1,n} - k^2 c_{3,n})^2 + 4k^2 c_{2,n}^2}}{2k^2 c_{2,n}}; \tag{5.4}$$

where $c_{1,n}$, $c_{2,n}$ and $c_{3,n}$ are quantities to reduce the complexity of calculations.

5.2.2 TLS implementation from cell-level to system-level

The TLS for capacity estimation is much more simple to implement than DSPKF for SOC estimation. After accessing current and SOC data, the only parameter to be tuned is the m value, which is the size of the segments after dividing. The values of the variances can be calculated based on empirical knowledge. However, after trying various values of them in this research, it is found that the values of the variances do not dominate the results of the TLS algorithm. The system-level implementation is not any more complicated than at the cell-level, although essential data selection work (to be introduced later in section 5.4), has to be done to ensure the accuracy of the system-level implementation. One more factor to consider is the choice of SOC data: DSPKF SOC or BMS SOC, because in the previous chapter, it has been found that the DSPKF SOC is generally better.

5.3 TLS capacity estimation results

In this section, cell-level and rack-level capacity estimation results using TLS are shown first, similar to their counterparts in previous chapter. More results

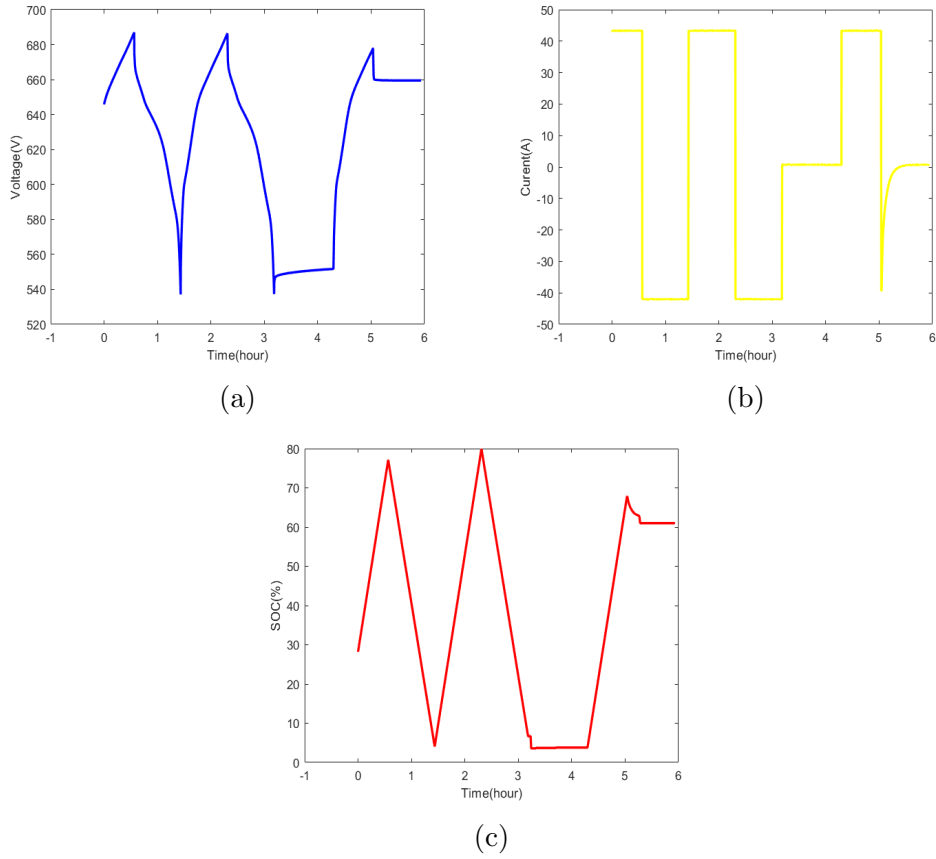


Figure 5.2: Yuasa rack data profile for capacity estimation (a) voltage, (b) current and (c) SOC.

are shown for the system-level, i.e., the results of the WESS.

5.3.1 Rack-level capacity estimation results

Figure 5.3 shows the capacity estimation results of the GS Yuasa Rack, which has been used in previous chapter to evaluate the DSPKF SOC estimation. The red dotted lines show $\pm 1\%$ error around the measured capacity. The current and SOC data used here are both from the internal BMS. The data profile used here is shown in Figure 5.2.

According to the experiments that were conducted on the GS Yuasa cells inside the rack, all of their capacities are currently larger than the nominal capacity (47.5 Ah) and the minimum cell capacity is 48.8 Ah. Because all the

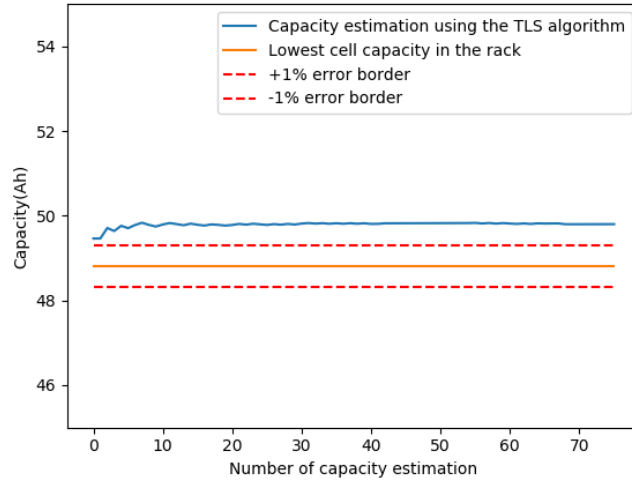


Figure 5.3: Capacity estimation results of a GS Yuasa NMC battery rack.

cells are in series, the rack-level capacity is limited by the weakest cell, which is also 48.8 Ah. It can be seen that the TLS results are slightly larger than the experimental results, and this may be due to the fact that at the end of the data profile used in this section the temperature has increased. This temperature is likely to be higher than the temperate where the experimental capacity tests were conducted (only one cycle), which increases the capacity of the cells/rack. The other reason may be the poor accuracy of the BMS SOC that is used for the TLS results here. The times of cell-level capacity test and the cycling test used for the TLS results are close so the degradation is ignored here. Further comparison between using the BMS SOC and the DSPKF for the TLS algorithm is not conducted here due to the fact that the rack can only be viewed as a very small battery system and it has not been tested for a long time.

Since the rack-level results are encouraging, more complicated implementation on a large-scale battery system, the WESS, looks promising.

Table 5.1: WESS Actual capacity calculations in May 2018

Results for 3 cycles	0.5C	1C	1.5C	2C
Average Capacity (Ah)	1600.21	1599	1600.76	1599.94
Standard deviation (Ah)	1.23	3.16	1.08	1.21
Relative standard deviation (%)	0.077	0.2	0.068	0.075

5.3.2 System-level capacity estimation results

In this section several datasets of measured current and BMS SOC from the WESS are used to estimate the system capacity and compare it with offline experimentally measured capacity using Coulomb counting.

The actual capacity estimation of the WESS

Tables 5.1, 5.2 and 5.3 show the actual capacity measurements of the WESS. Ideally full constant discharges are needed but the operational window of the system is limited to 95% - 5% SOC. Therefore, the capacity tests were done between 95% and 5% SOC in May 2018, between 90% and 10% SOC in Oct. 2019 and between 90% and 10% SOC in May 2021. The system was cycled with constant powers of 0.5MW($\sim 0.5C$), 1MW($\sim 1C$), 1.5MW($\sim 1.5C$, except in 2019) and 2MW($\sim 2C$, except in 2021), and tested 3 times for each power rate. Based on equation 5.1, the capacity was calculated by taking the integral of current and dividing this by 90% or 80%. To ensure the best accuracy, some cropping techniques have been used, i.e., the data when power curtailment is undertaken, which in this case are close to the end of the discharge, were discarded for calculation.

These results show that the capacity degradation of the system over 3 years is negligible and the variations seen are likely measurement noise. Some results are higher than 1600 Ah and this is because actual cell capacities from the manufacturer were higher than the nominal at installation.

Table 5.2: WESS Actual capacity calculations in Oct. 2019

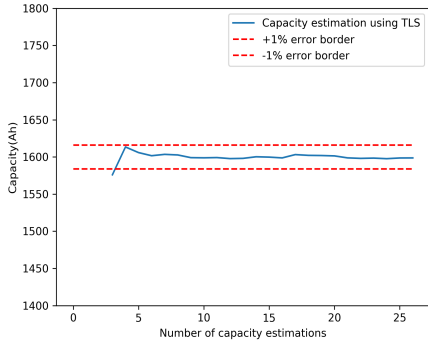
Results for 3 cycles	0.5C	1C	2C
Average Capacity (Ah)	1600.93	1604.44	1600.85
Standard deviation (Ah)	1.25	4.83	0.9
Relative standard deviation(%)	0.078	0.301	0.056

Table 5.3: WESS Actual capacity calculations in May 2021

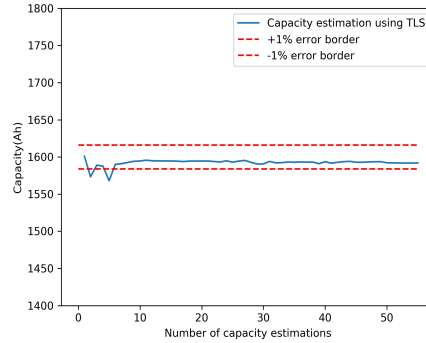
Results for 3 cycles	0.5C	1C	1.5C
Average Capacity (Ah)	1601.73	1600.74	1600.63
Standard deviation (Ah)	1.52	2.14	1.7
Relative standard deviation(%)	0.095	0.134	0.106

Capacity estimation results with different datasets

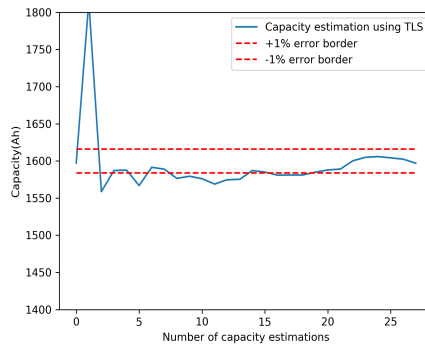
Figure 5.4 shows the capacity results of the same profiles in Figure 4.9. Note that for these results the number of data points for each interval is tuned and fixed, and the noise on the current measurement is estimated based on empirical knowledge. The assumed capacity is 1600 Ah and the error borders refer to this value. In Figure 5.4a and Figure 5.4b, the algorithm takes some time to converge because the estimated capacity was initialised as 0 (for worst-case demonstration), and the reason of no results at the beginning of Figure 5.4a is that the SOC values were maintained at 50%, so there were no SOC variations, which is the denominator for calculating Q using equation 5.1. After that, these results are stable and mostly within the error borders. This is because the first 2 datasets contain large SOC variations and the current values are mostly constant. In comparison, the results in Figure 5.4c show that the algorithm's performance is affected by the quality/type of data. The errors are significantly larger and the results fluctuate. There are several reasons for the worse results: a relatively flat SOC profile (a frequency response that causes small SOC variations), this is because the error is relatively significant with small SOC variation, according to equation 5.1; sharp and short spikes in current data, which leads to inaccurate current integration due to sampling rate.



(a)



(b)



(c)

Figure 5.4: Capacity estimation results of (a) constant cycling (~ 6.5 hours), (b) mixed profile (~ 9 hours) and (c) dynamic frequency response (~ 7 hours). The red dotted lines show $\pm 1\%$ error around the 1600 Ah assumed capacity.

5.4 Data selection for system-level estimation

The results in Figure 5.4 show that data should be selected before imported to the TLS algorithm for accurate system-level capacity estimation. This data selection is possible due to the fact that a battery's capacity is not fast changing and therefore the time between estimates can be large. In this section, more details, i.e., the essence and methodology of data selection for online battery system state estimation are shown.

The implementation of “online” capacity estimation algorithm is essential for monitoring the degradation of BESSs during long time operation. For

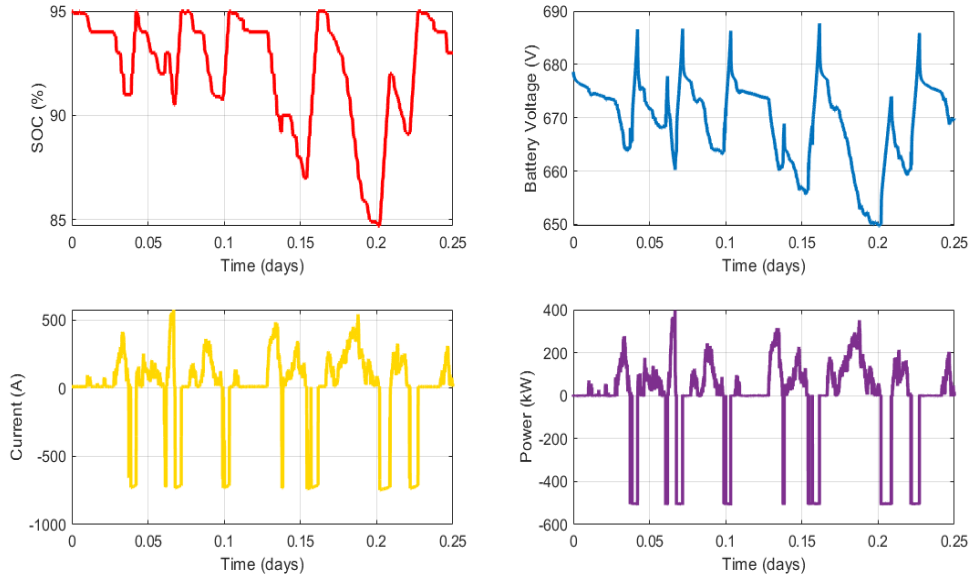


Figure 5.5: A WESS 6-hour data profile for investigating the value of m and data length.

online estimation of the WESS, the data is first obtained from a time-series database (InfluxDB), followed by the TLS capacity estimation algorithm.

5.4.1 Methodology

The length of the data and the value of m affect capacity estimation results using the TLS algorithm. In Figure 5.6, a short data profile (6 hours, shown in Figure 5.5) is used to investigate the relationship between the value of m and capacity estimation results. A range of m values are tried, from 100 to 1000. It can be seen that the choice of m value should avoid too large or too small values. Besides, according to the TLS results using this dataset (Figure 5.6b), the algorithm starts to provide accurate and stable estimations after 4 hours, so the data length cannot be too small to be sufficient for the algorithm.

According to the results shown in Figure 5.4 and above discussion, a series of criteria of data are shown below for accurate online capacity estimation [7]:

- Significant variations in SOC data are available continuously, as dis-

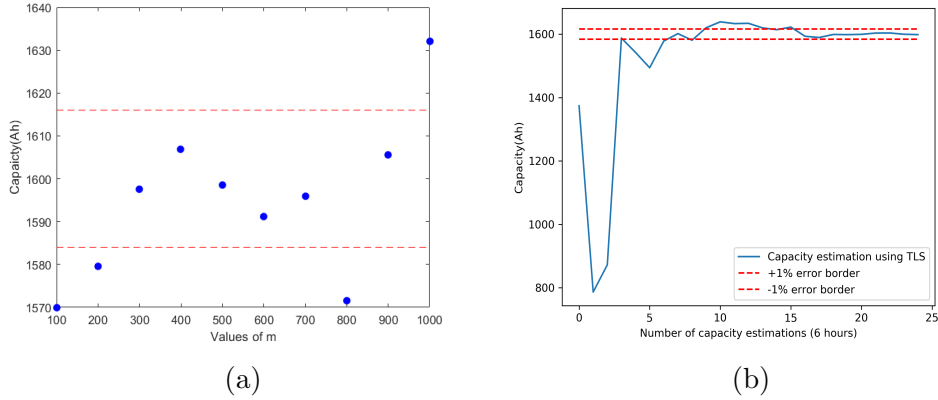


Figure 5.6: How the value of m and data length affect capacity estimation results (a) relationship between m and capacity estimation results and (b) Convergence time of the TLS algorithm.

cussed above.

- A large interval size for calculation: as the data is divided into a number of intervals with a size of m , its value should be large enough to make sure there are some SOC variations for every calculation. This value is set to 500 samples for the results shown in Figure 5.4.
- Sufficient data: the data points should be enough for the algorithm to converge, since it calculates the capacity recursively.
- No sharp, short spikes of current data: as discussed, to avoid errors in current integration.

For long-time capacity estimation, an algorithm for data-selection of the WESS has been developed to select the data that meet the aforementioned criteria, as shown in Figure 5.7. The data (system-level current and SOC) is first divided into chunks representing approximately a week of operation. Next, within each chunk, invalid data is checked by calculating the change in voltage (section 4.6). The data chunk is then divided further into several even shorter datasets by deleting the invalid data periods. The length of the first data segment is checked, if it is shorter than the predefined criterion, it is discarded. This criterion is set as 30000 data points in the long time

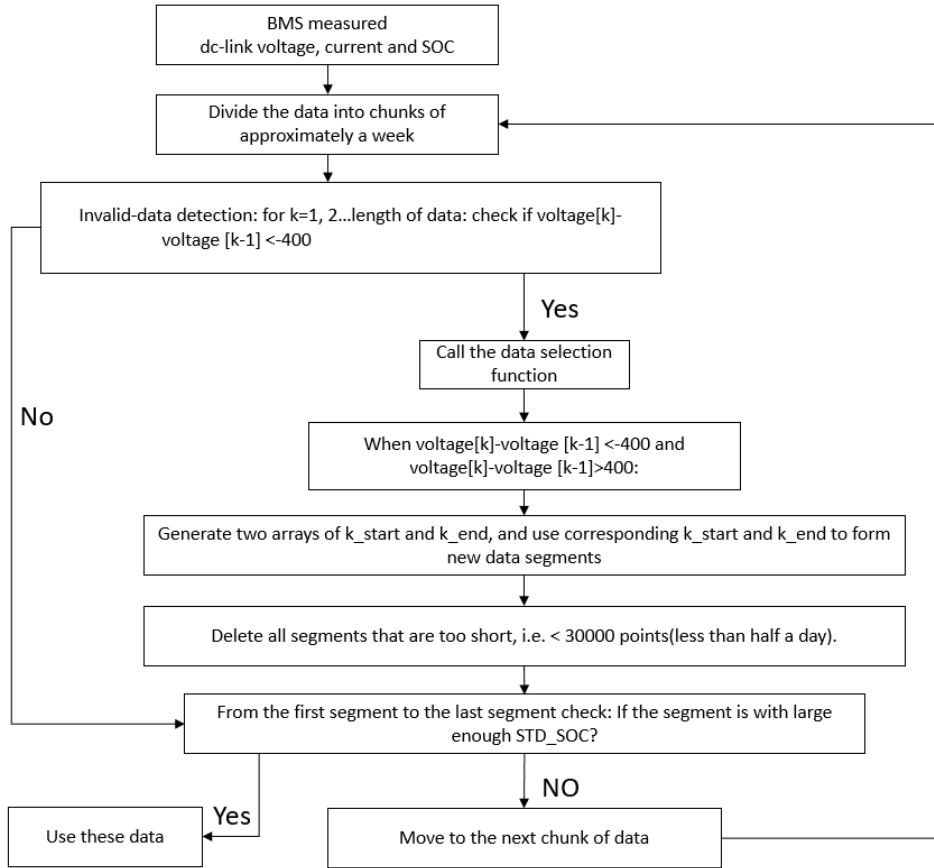
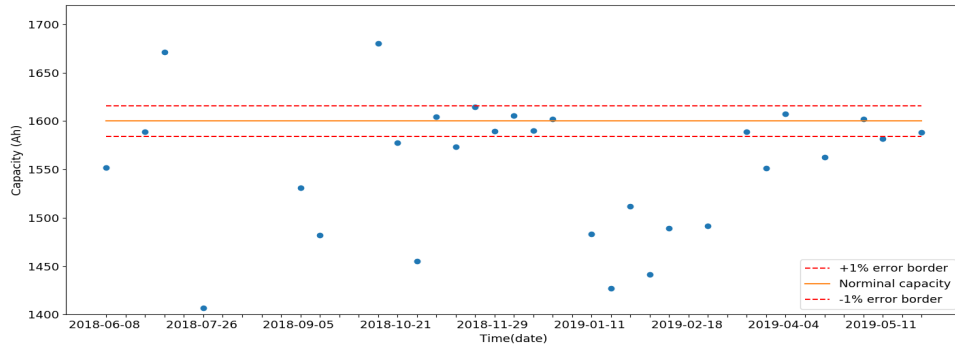


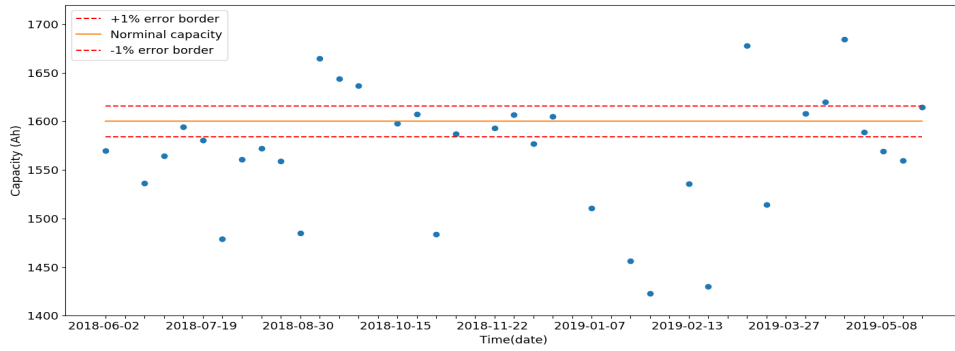
Figure 5.7: Diagram of data-selection for BESS capacity estimation

capacity estimation results shown in this thesis, which is around the number of data points of half a day. If the dataset is long enough, the algorithm then moves to check whether the SOC variations are large enough, i.e., the standard deviation (STD) is larger than the predefined value. If this criterion is not met, the script moves to the next data segment, until it finds the data to represent this week. Therefore, it is possible that no data is chosen in a week and no capacity estimation results are updated.

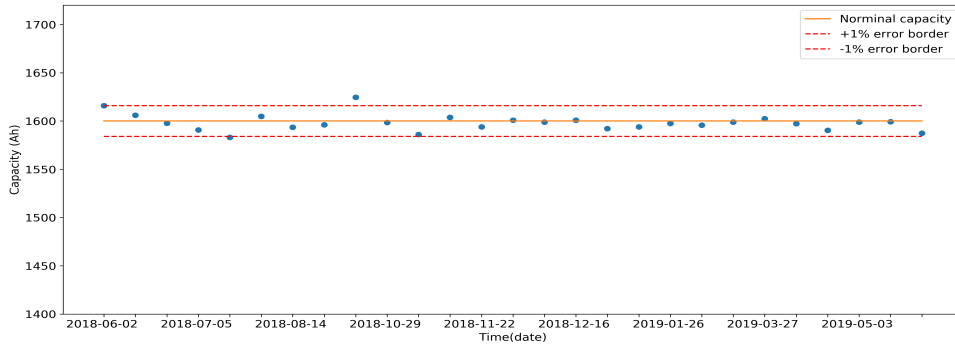
By running the algorithm like this, the capacity estimation results are updated every week if there are data that meet the criteria.



(a)



(b)



(c)

Figure 5.8: Capacity estimation result comparison using a whole year data (a) use raw data, (b) only deal with invalid data and (c) with data-selection techniques.

5.4.2 Results and discussion

Figure 5.8 compares capacity estimation results to show how data-selection improves the accuracy, using a whole year's data of the WESS. DSPKF SOC, which is often more accurate than the BMS SOC, is chosen as the input in these results. The nominal capacity, 1600 Ah is again considered as the actual capacity for reference.

It can be seen that if no data-selection applied at all, only a small fraction of results are within the 1% error borders as shown in Figure 5.8a. Note that extremely large or small results (errors larger than 10%) are not shown in the figures. After removing invalid data periods, the results are improved and more are within the error borders and shown in the figure of Figure 5.8b. After applying the data-selection algorithm, the capacity estimation results are mostly within the error borders as shown in Figure 5.8c. To sum up, data-selection techniques ensure the accuracy of TLS algorithms for capacity estimation of the WESS.

The variation of SOC, as discussed, also affects the accuracy of the TLS algorithm. Using the BMS SOC or the DSPKF SOC and system-level current of the WESS, with data-selection techniques, long-time capacity estimation of can be achieved. Figure 5.9 illustrates the effects of SOC variation on one-year's capacity estimation results, using system-level current and the BMS SOC. The mean capacity estimation error is calculated as the quotient of average capacity errors in the year and the actual capacity. In these results, only SOC variation is different, and for comparison, other factors (m and data length) are fixed. It can be seen that generally larger SOC variation improves capacity estimation accuracy, but it provides less capacity estimation results.

5.4.3 Summary

This section demonstrates how to evaluate the quality of current and SOC for capacity estimation using TLS. The results using the data selection techniques are with significant improvements of accuracy compared with using the data in its raw form. A diagram of dealing with invalid data and data-selection for capacity estimation is shown in Figure 5.7: combining the TLS

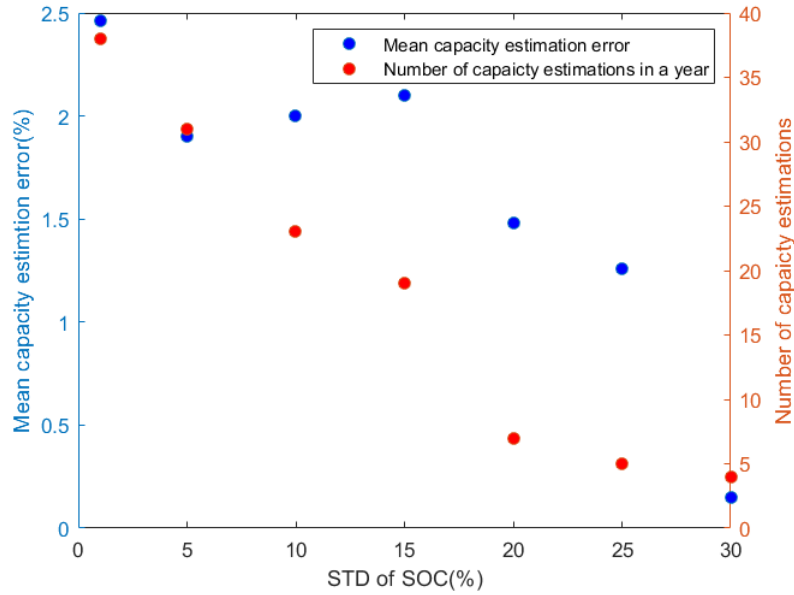


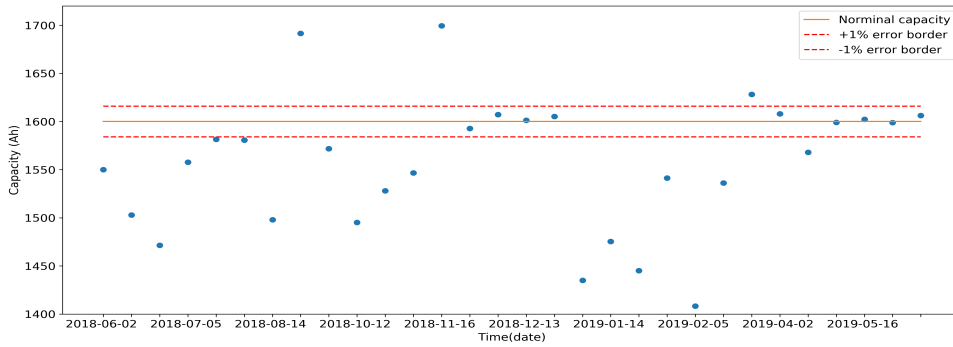
Figure 5.9: Investigate the effects of SOC variation using data of a year.

algorithm with data-selection techniques, capacity estimation of BESSs with improved accuracy using system-level data can be realised.

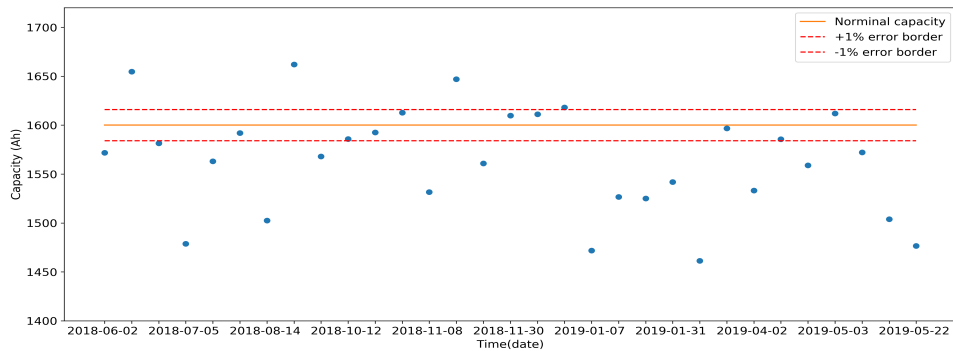
5.5 Comparison of capacity estimation using BMS SOC and DSPKF SOC

This section compares the accuracy of the TLS capacity estimation algorithm, using the BMS SOC and the DSPKF SOC as an input. Figure 5.10 shows the capacity estimation results using WESS operational data from 01/06/2018 to 01/06/2019, using the BMS SOC and the DEKF SOC respectively. The results using the DSPKF SOC has already been shown in Figure 5.8c. The dataset (current, BMS SOC, voltage and time) is again processed according to Figure 5.7, for data-selection. The DSPKF algorithm is run on these sets of data to provide an estimate of SOC with the capacity parameter set to the nominal capacity (1600 Ah) of the system.

It can be seen that the errors of TLS capacity estimation results using



(a)



(b)

Figure 5.10: Capacity results of one year using (a) BMS SOC and (b) DEKF SOC.

the DSPKF SOC are mostly within the 1% error bounds of the measured capacity, but the errors of using BMS SOC are much higher. Most capacity estimations errors using the BMS SOC over the year are less than 10% but only around 10 estimations (about 1/3) are within the 1% error borders. Results using the DEKF SOC are slightly better than using BMS SOC but not significant. Therefore, this verifies that the DSPKF is a more advanced method over the DEKF, which is the reason why in this work most SOC results are from the DSPKF. Besides, it could be concluded that replacing the BMS SOC with the DSPKF SOC can significantly improve the accuracy of capacity estimation. However, it can be argued that this result is achieved when the system is relatively healthy using the nominal capacity as an initial capacity for SOC estimation, whereas for a degraded system there would be significant error according to equation 2.2. When the battery system is

degraded, the Q_{actual} in the equation will be larger than it actually is, this affects the accuracy of the DSPKF SOC algorithm, thereafter decreasing the accuracy of TLS capacity estimation algorithm.

The practical and simple way to account for degradation is to use the Coulomb counting method. Despite stating that this is not good enough for accurate SOC estimation, accurate capacity information for DSPKF is not needed, since only a crude estimation is enough to ensure the SOC converges to a good enough value [94].

The multi-scale DSPKF algorithm introduced above makes the capacity correction based on SOC prediction possible. After every macro time duration, the SOC can be predicted using Coulomb counting with the estimated capacity. Then the predicted SOC is compared with the micro time scale estimated DSPKF SOC or the BMS SOC (reference SOC). Equation 5.5 shows the calculation of predicted SOC [52].

$$SOC_{k,L} = SOC_{k,0} + \frac{T}{C_k^-} \sum_{j=0}^{L-1} -I_{k,j} \quad (5.5)$$

where $SOC_{k,0}$ is the SOC estimation at the beginning of a macro scale, k the number of micro SPKF estimations, T the sample rate in the micro SPKF, C_k^- the initialised or last estimated capacity, L the number of samples in every macro scale estimation and $SOC_{k,L}$ is the projected SOC. The correction of capacity is shown in the equation below:

$$C_k^+ = C_k^- + K(SOC_{k,L} - SOC_k) \quad (5.6)$$

where K is a gain, SOC_k the reference SOC, and C_k^+ is the corrected SOC. The purpose of using K is to accelerate the convergence since the SOC is a value between 0 and 1. The value of K is tuned to control the correction speed, and is positive when the system is charging and negative when the system is discharging. For example, assuming the last estimated capacity is larger than the actual one when the system is charging, according to equation 5.5, the projected SOC would be smaller than the micro SPKF estimated SOC or BMS SOC. Thus, the SOC difference in the bracket in the equation

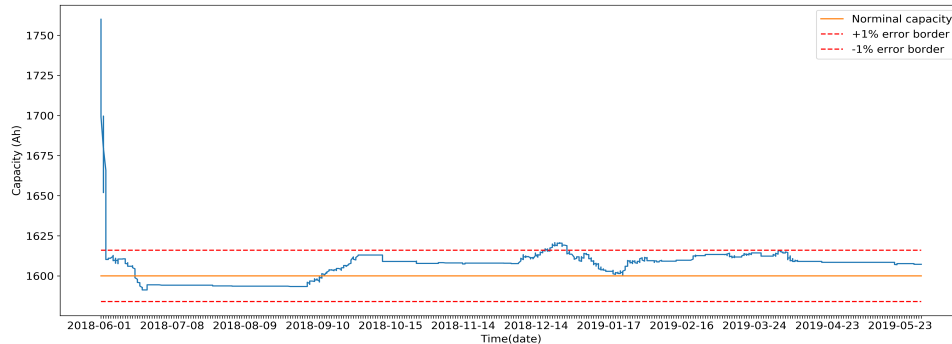


Figure 5.11: Capacity tracking using capacity correction technique over one year of data.

above is a negative value, which multiplies a positive K . As a result, the last estimated capacity value will be decreased toward the actual capacity.

The results of capacity tracking over the year are illustrated in Figure 5.11. The initial capacity was set as 1760 Ah, which is 10% higher than the actual capacity to simulate degradation. The errors are mostly within the 1% error bounds again for the year from 01/06/2018 to 01/06/2019. These capacity results can be provided regularly to update the DSPKF algorithm, creating a reliable input for the TLS algorithm; more accurate capacity estimation can then be obtained. Long-time results of this method are generally acceptable but the disadvantage is that the gain (K) is difficult to tune and it relies on the quality of the data. For example, if K is too large, the capacity could be over-corrected without good quality data, and if K is too small, this method requires a long time to converge to be within an acceptable range (the 1% error bounds).

5.6 Battery capacity tracking using DSPKF and TLS

As discussed above, the WESS does not show degradation, but one of the objectives of this work is to achieve capacity tracking on other batteries to show that the algorithms are effective for all battery systems.

In this section, the capacity tracking algorithm is first implemented on the

JGNE NMC cell, followed by the implementation on the GS Yuasa battery system.

5.6.1 Capacity tracking of an NMC cell

Through cycling tests, the JGNE NMC 2.6 Ah cell, as shown in Figure 3.7 reached EOL after 800 cycles. The test temperature was 35°C and the cell was kept in the environmental chamber as shown in Figure 3.10c. The cell's cut-off voltages are 4.2/2.75V but they were not reached in the cycling tests. Instead, cut-off voltages, 4.12/3V were used to increase the cycle life [126] in a high temperature environment. In the results shown below, SOC range is adapted, i.e., charge process (CC/CV) ends at 4.12V as 100% SOC and 3V is the cut-off voltage of discharge, as 0% SOC. The OCV-SOC relationship is within this smaller range and the ECM parameters are measured by the EIS machine. The actual capacities of the cell are obtained from the Maccor cell tester, which can be seen as an ideal reference for the capacity estimation algorithms, because the Maccor has highly accurate current sensors (table 3.3).

Figure 5.12 shows the capacity tracking results of the JNGE cell over the whole battery life. The figure on the left shows the results of using the simple capacity correction method and the other one shows TLS results using DSPKF SOC, which updated together with the corrected capacity. The RMSEs of the capacity results using capacity correction and TLS are 0.07 and 0.045 Ah respectively. It can be argued that the results are acceptable but the errors are not minimal, although after using TLS the results have been improved. The not ideal performance of the DSPKF algorithm is because of the variable OCV-SOC relationship of the cell during its cycling life. Through the cycling, it has been noted that the relaxation voltage, which has been used to calculate the OCV-SOC relationship is not constant and sometimes they disagree with each other quite significantly. Further work to improve results using this NMC cell could focus on improving the OCV-SOC relationship used in the DSPKF algorithm [127]. However, it is not the objective to investigate how to accurately track an NMC cell's degradation, so in this

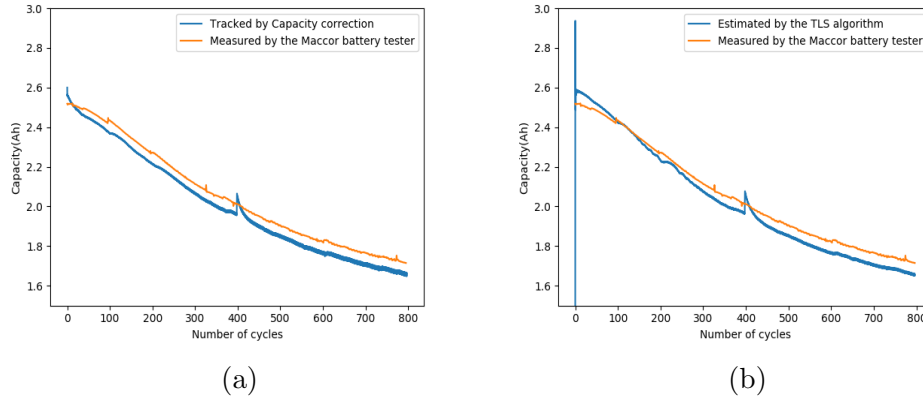


Figure 5.12: Capacity tracking results of a JGNE NMC cell (a) tracking by the capacity correction algorithm and (b) tracking by the TLS algorithm.

work the discussion will be back to the implementation of the algorithms on BESSs.

5.6.2 Capacity tracking results of GS Yuasa battery energy storage system

With the 3-year operating data of the GS Yuasa BESS, as shown in Figure 5.13, capacity tracking using the DSPKF and TLS algorithms is possible because the chemistry of this system, NMC, is different from the WESS, LTO, which has much better performance regarding degradation. The white spaces in the data profile figures are where invalid data occurs, which is shown as “NaN” in the ADEPT data.

For the results shown in Figure 5.14, the DSPKF SOC is from a similar algorithm to the one used for the capacity tracking of the JGNE cell, but the invalid data and the data-selection techniques introduced in section 4.6 and section 5.4 are used. The DSPKF parameters, ECM parameters, and the system-level OCV-SOC relationship are the same as the implementation in section 4.4.2.

For actual capacity of the ADPFT Li-ion battery, there has been a range of tests for cycling the battery between 100% and 5% SOC. Therefore, there are data that are ideal for capacity estimation but other information like test

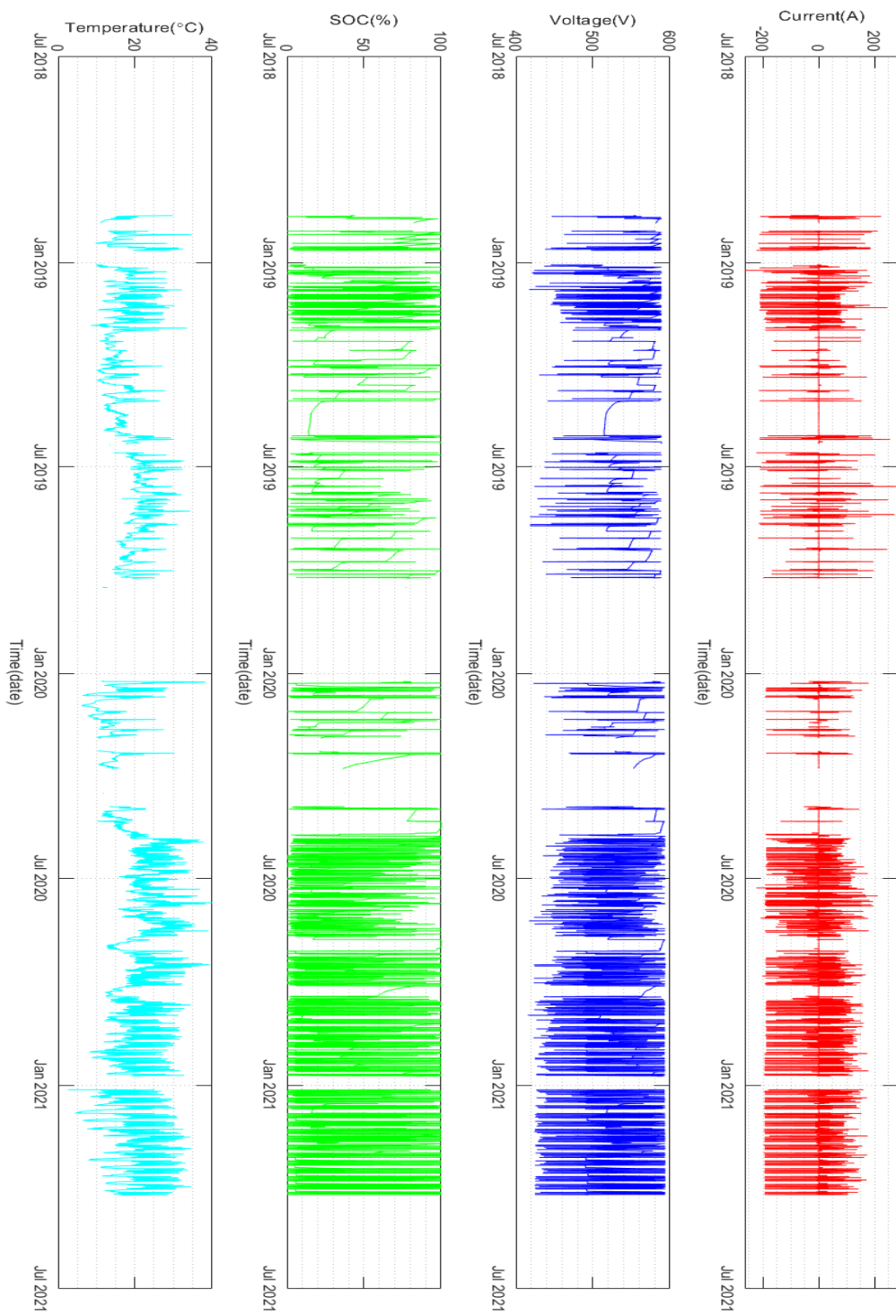
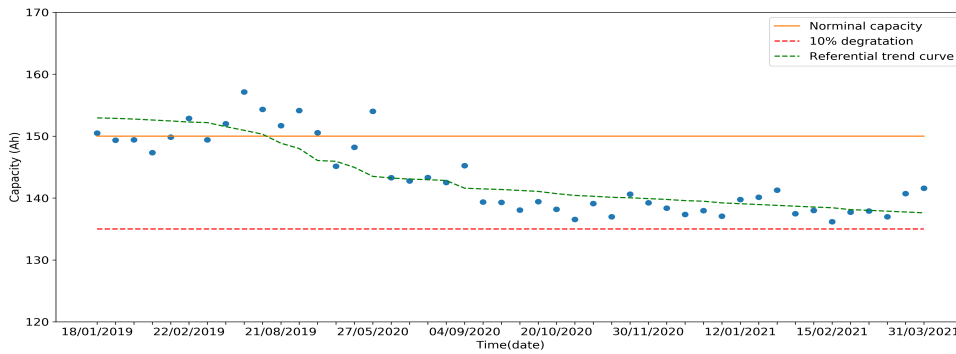
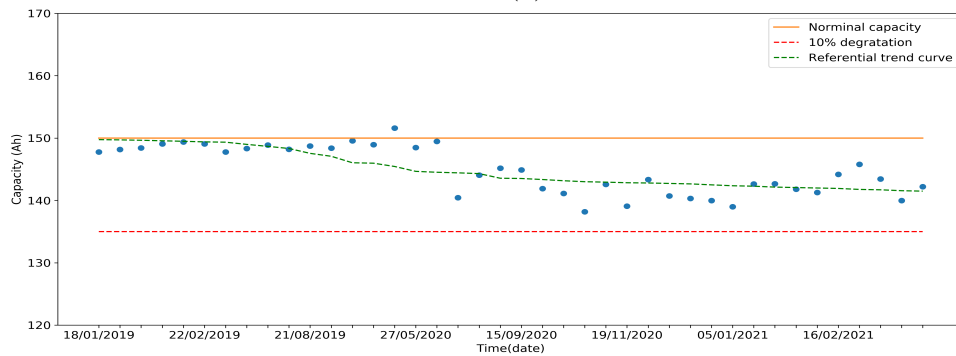


Figure 5.13: 3-year operating data of the GS Yuasa BESS.



(a)



(b)

Figure 5.14: Capacity results of 3 years of GS Yuasa BESS using (a) DSPKF SOC and (b) BMS SOC.

time and C-rate has not been obtained, so there is no reference capacity as ideal as in tables 5.1 to 5.3 . However, the capacity estimation results using the BMS SOC are still considered to be a reasonable reference for validating the DSPKF and the TLS algorithms.

In both results, the green dotted line is a trend curve obtained by curve fitting for reference. The start time of these results is not the same as the actual data because the data at the beginning are invalid. It can be seen that in both results, the capacity results are mostly within the 10% degradation border, which means the system is still healthy and the results of using the DSPKF SOC are not far from the reference. Both results show a reasonable degrading trend but between Jan. 2019 and June 2020 the results from using the BMS SOC are more stable. It is difficult to compare the accuracy of both results but the intention of showing these results using the GS YUasa BESS

data is to show that the algorithms introduced in this work are applicable to other BESSs.

5.7 BESS capacity estimation using power and SOC

There are two scenarios where dc-link current and voltage may be unavailable, these are 1) where the lower levels of the system data structure are unavailable to the asset owner/operator through the “customer” interface, 2) where the BESS is connected to an aggregators platform, the communication of data is usually limited to available power, power and SOC and lower level data streams are not commonly exchanged. In the latter case the capacity estimation algorithm is processed remotely and therefore cannot use the dc-link data. This section investigates whether it is practical to estimate BESS capacity/SOH using power, instead of current, and SOC data.

5.7.1 Methodology

The method introduced below is based on the existing TLS capacity estimation algorithm. For the WESS, the power data are in kW, so the calculated capacity is not in Ah, but in kWh. Equation 5.7 and equation 5.8 show how to calculate the capacity of a BESS in kWh.

$$\int_{t_1}^{t_2} \frac{-\eta P(\tau)}{3600} d\tau = Q(SOC(t_2) - SOC(t_1)) \quad (5.7)$$

Again, for the simplicity of calculation:

$$y = \int_{t_1}^{t_2} \frac{-\eta P(\tau)}{3600} d\tau \quad \text{and} \quad x = SOC(t_2) - SOC(t_1) \quad (5.8)$$

where P is the power data that are needed for the capacity calculation and the rest of the equations are exactly the same to equations 5.1 and 5.2.

By combining equations 5.7 and 5.8, with equations 5.3 and 5.4, the capacity calculation with power data can be realised.

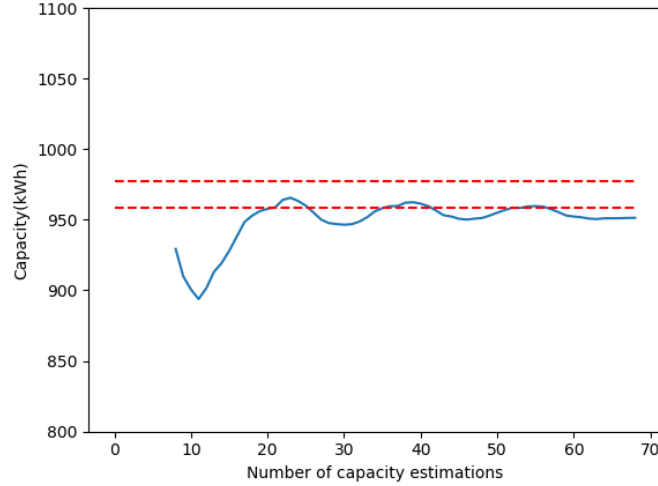


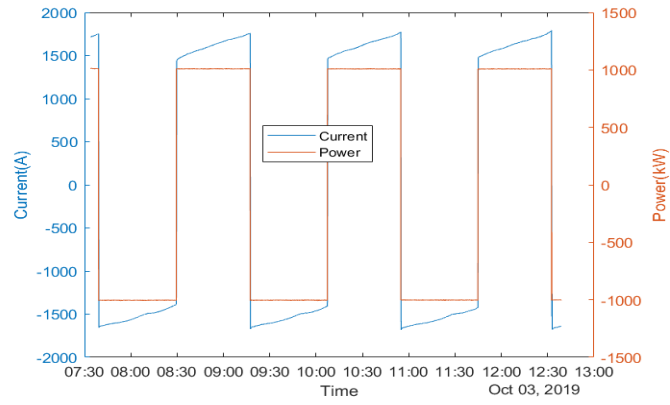
Figure 5.15: Capacity estimation using power and SOC of constant cycling.

5.7.2 Results and discussion

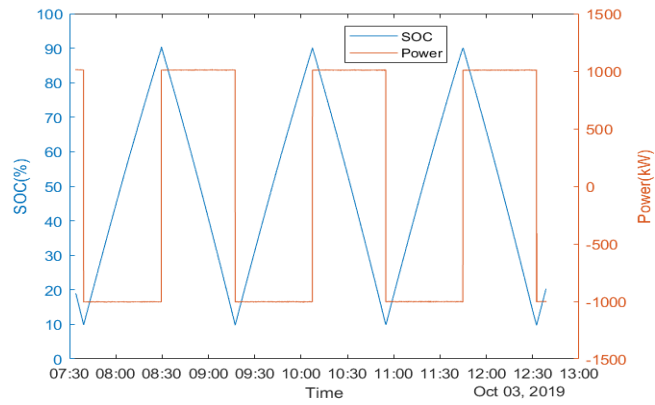
In the WESS, LTO cells cut off at 1.8V rather than 1.5V, so the operational capacity of the WESS is lower than 1MWh, and is measured at 968kWh. Figure 5.15 illustrates the capacity estimation results using power with the same WESS operation profile as is used in Figure 4.9a. It can be seen that the estimations are mostly not within the error borders. For long time estimation, larger errors are shown in Figure 5.17 compared with the ones in Figure 5.10. By using the DSPKF SOC, the results are not improved significantly than using the BMS SOC. Therefore, the power data that have been used is the reason for worse results.

Figure 5.16 compares power data with current data, SOC data and dc-link power data respectively. The dc-link power is calculated by multiplying dc-link current and voltage. In Figure 5.16a and Figure 5.16b, it can be seen that the power data are basically synchronised with current and SOC data, while Figure 5.16c shows that the power data generally have a larger magnitude than the calculated dc-link power. Note that in this section, for the investigation below only the preferred DSPKF SOC is used.

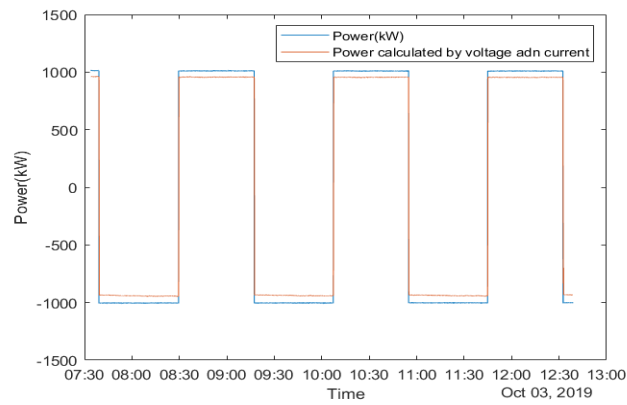
In Figure 5.18, results using dc-link power are shown. It can be seen that



(a)

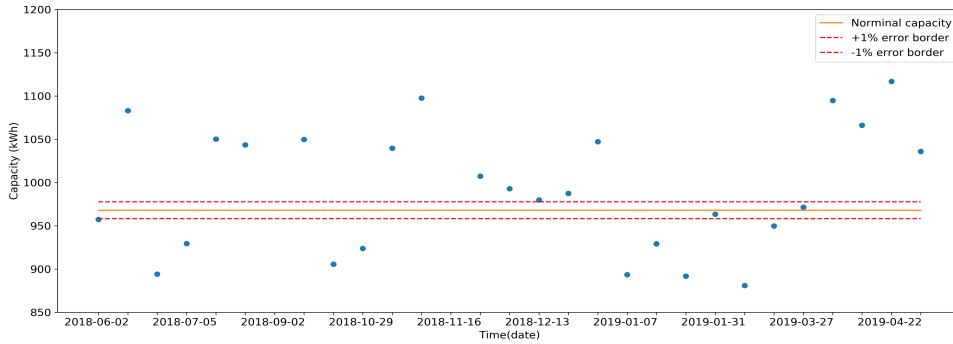


(b)

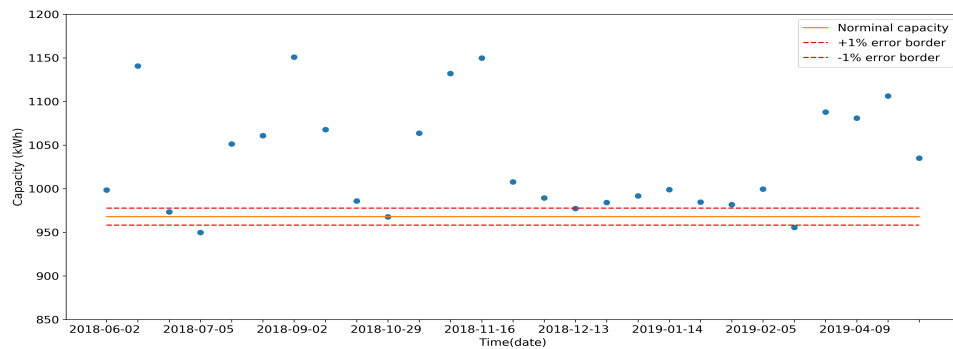


(c)

Figure 5.16: WESS data at 1C in Oct. 2019 (a) power and current, (b) power and SOC and (C) power and dc-link power.



(a)



(b)

Figure 5.17: Capacity results of one year using (a) power and BMS SOC and (b) power and DSPKF SOC.

the results using dc-link power outperforms the counterparts of using power data. However, the results of using dc-link power are just to compare with using power data, since the calculation of dc-link power needs current and voltage data. If these data are available one will just use the original method shown in previous sections, rather than calculating dc-link power. Therefore, the practical approach is still to use the power data provided.

After Jan. 2019, not all the inverters have been working in the WESS, so at least half of the data used in Figure 5.17 are affected. To investigate how the number of inverters working affect capacity estimation results, the power data in 2019 are scaled according to the number of inverters assumed working, which are 22 out of 24 most of the time. Figure 5.19 compares the capacity estimation results in 2019 between using raw power data and the scaled power data. The mean errors in Figure 5.19a and Figure 5.19b are

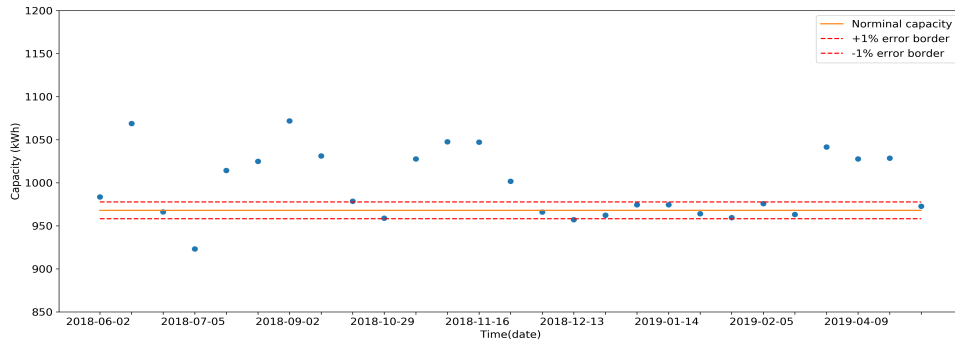


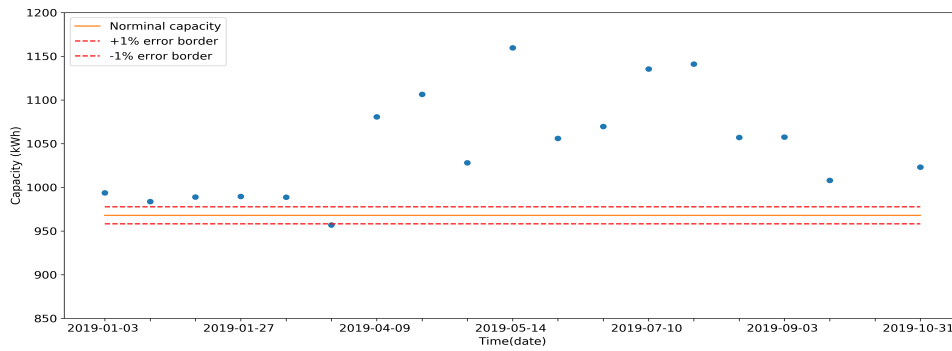
Figure 5.18: Capacity estimation using dc-link power and DSPKF SOC.

86.5 and 48.1 kWh respectively. It can be seen that the actual number of inverters working affects the results, but by considering this the errors are still significantly larger with respect to using current.

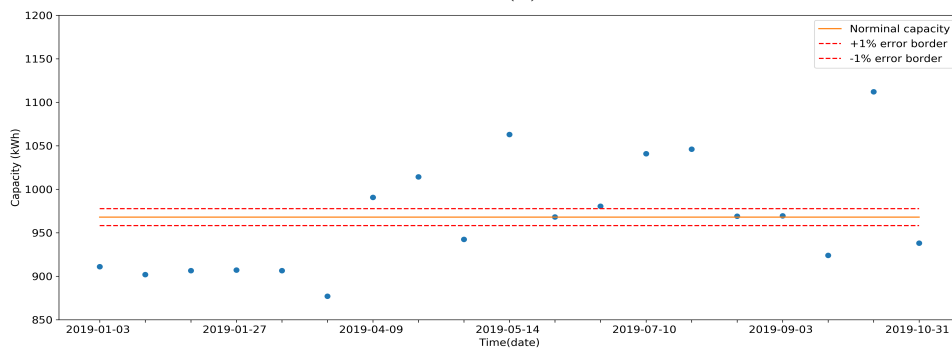
From here, more essentially, inverter efficiency will be considered, to investigate how it affects the capacity estimation results using power and SOC.

Figure 5.20 compares the capacity estimation results of 2018 (to avoid the number of inverters working issue) between using raw power data and the scaled power data assuming the inverter efficiency is fixed at 94%. The mean errors in Figure 5.20a and Figure 5.20b are 46.6 and 27.5 kWh respectively. The much improved results in the latter show that inverter efficiency has an essential role when replacing current data with power data.

To investigate further, a relationship between efficiency and power is used, as shown in Figure 5.21a. For results in Figure 5.21b, scaled power data are used according to the relationship. This measured relationship is not proved to be accurate especially when the power is larger than 250 kW but it is still used here because the WESS normally operates with low power. These results are with a much smaller mean error compared with previous results, which is only 24.9 kWh (2.6% with respect to the actual capacity). The results further suggest the necessity of considering inverter efficiency when using power data for capacity estimation. Based on the discussion above in section 5.4, increasing the criteria of data selection can improve the estimation accuracy, sacrificing the number of estimations. The results shown in Figure 5.21c are from an updated data-selection algorithm that increases



(a)



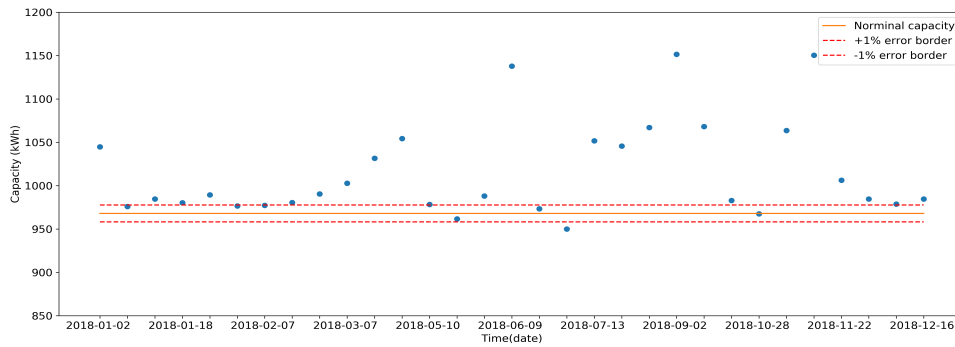
(b)

Figure 5.19: Capacity results of 2019 (a) using power and DSPKF SOC directly and (b) assuming only 22 inverters out of 24 worked in the whole year.

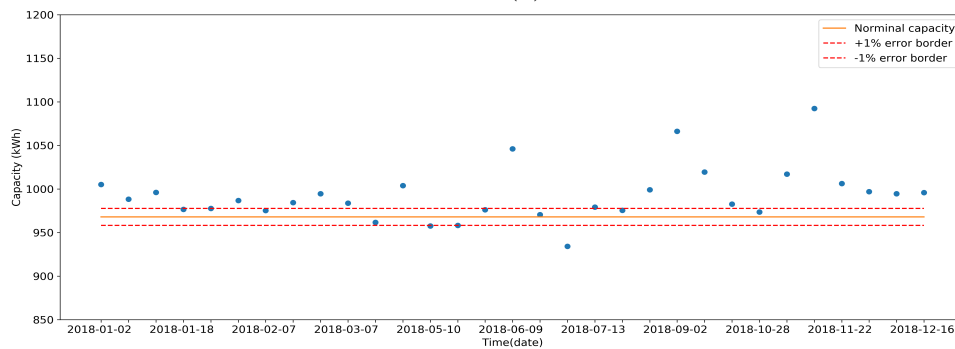
the criterion of SOC variation to an STD of 15% from 5% (the value for most long-time capacity estimation results in this thesis). The mean error is as low as 11.7 kWh (1.2% with respect to the actual capacity) and the number of estimations drops to 24 from 31. An error of 1.2% is not much higher than the results of using current data, which shows the promising future implementation of using power data instead of current data on other BESSs.

5.7.3 Summary

It can be concluded that using power data instead of current data for the TLS capacity estimation is practical and promising. The errors using power



(a)

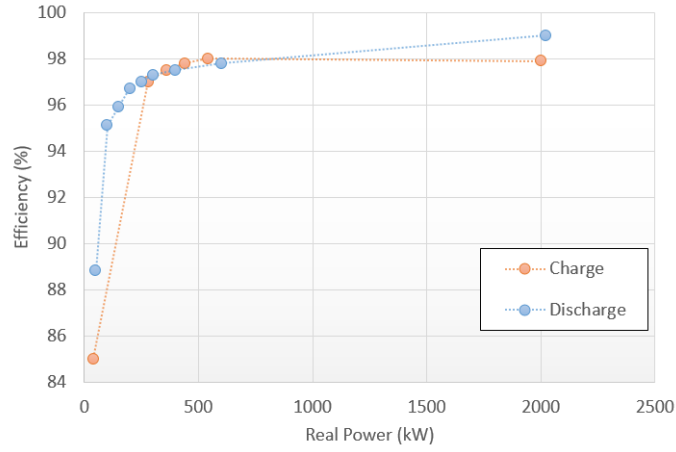


(b)

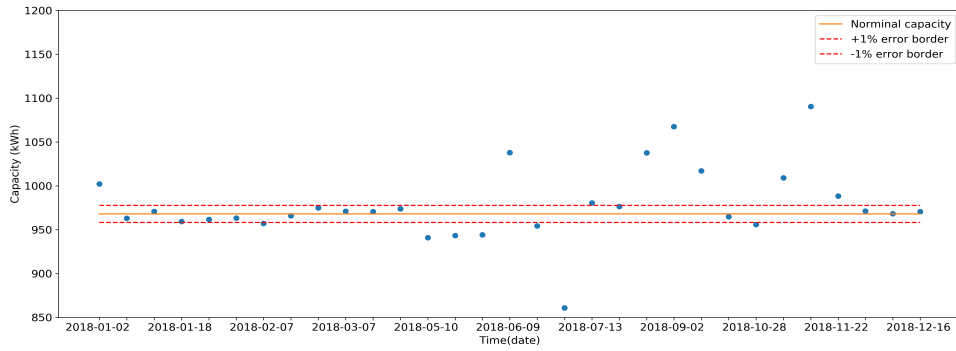
Figure 5.20: Considering inverter efficiency using one year data of 2018 (a) using power and DSPKF SOC directly and (b) assuming the inverter efficiency is fixed at 94%.

data are significantly larger than the counterparts of using current data if the factors of inverters, especially inverter efficiency are not considered.

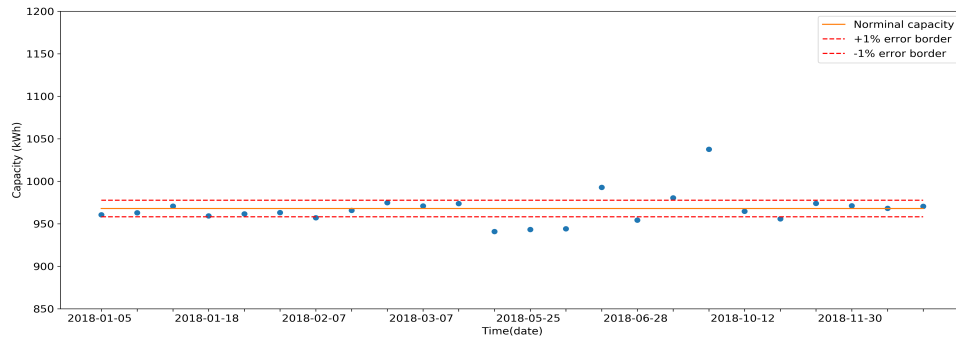
By comparing different results, including using the raw power data, a fixed inverter efficiency value and the efficiency and power relationship, the importance of inverter efficiency for capacity estimation is shown. Especially by using the relationship between inverter efficiency and power, the estimation error can be significantly decreased to be close to the errors using current.



(a)



(b)



(c)

Figure 5.21: Considering inverter efficiency using the relationship between efficiency and power, capacity estimation results of 2018 (a) the relationship between inverter efficiency and power, (b) using the mapping and (c) using the mapping with a higher criterion of SOC variation.

5.8 Conclusion

This chapter shows capacity estimation results of using the TLS algorithm, Coulomb counting and KFs on the cell-level, rack-level and system-level. At the cell-level, capacity tracking of an NMC cell has been shown to demonstrate the algorithm for system-level estimations. At the rack-level, the capacity estimation results of a Yuasa rack are shown as the demonstration of the algorithm on a small battery system. Most importantly, the capacity estimation of a large-scale battery system is discussed. Provided with system-level current and SOC, system capacity can be estimated by a TLS algorithm. For improved accuracy, the DSPKF SOC should be provided to replace the BMS SOC. This shows that the DSPKF SOC outperforms the BMS counterpart, together with the better RTE results. A data-selection algorithm has also been developed based on the fact that the system-level data often do not match the quality of the cell-level data and the capacity is not fast-changing so does not necessarily need to be estimated constantly. To support the application of the algorithms on other BESSs, the implementation on another BESS, GS Yuasa, has also been demonstrated and the results are promising, although more discussion and better results could be made with more information of the BESS in the future. In the end, a modified TLS algorithm is proposed for the case where current data are not available, with the consideration of inverter efficiency to obtain acceptable accuracy.

Chapter 6

Parameter estimation of large-scale battery systems

6.1 Introduction

The parameter estimation from the weight filter of DSPKF can not only increase the accuracy of SOC estimation, but also track the change of the values of the resistors in the equivalent circuit model. The series resistor (R_s) in the model has been attractive in the literature since it can be seen as a health indicator of SOH, as discussed above in section 2.6.2. As the battery ages, the series resistor is expected to be larger than the initial value. Therefore, the estimation of R_s can be essential for degradation modelling and EOL prediction.

In this chapter, parameter estimation and tracking results are shown, again from the cell-level to the system-level. The cells and the systems are the same as the ones used in the previous chapters (chapter 4 and chapter 5).

Through EIS tests, a cell's series resistor can be obtained, as it usually corresponds to the intersection on the real axis of an impedance spectrum [72]. Thus, the DSPKF estimated R_s can be validated by the experimental results. While for the DSPKF algorithm for system-level estimations introduced in chapter 4, initial equivalent-circuit parameters are calculated by

scaling cell-level EIS results, as it is unlikely to conduct a system-level EIS test. Therefore, the system-level estimated parameters could not be validated directly. In this chapter another method, voltage simulation, is used to validate the results of system-level parameter estimation, by comparing the simulated terminal voltage with the actual terminal voltage.

6.2 Parameter estimation results from cell-level to system-level

In the same way as in previous chapters, parameter estimation results are shown first for the cell-level and then the system-level. Although R_1 and τ_1 are estimated simultaneously with R_s in the DSPKF, these results are not shown in this thesis. The reasons are because they are much less interested than R_s and their estimations are difficult to be experimentally verified. Unlike R_s , the variations of these parameters are not relevant to the degradation of the battery, instead of showing the short-time changes inside the battery. Also, the values of them are determined according to the complexity of the ECM, so more difficult to be used as references than the R_s values. Besides, the system-level results of them are not as good as the results of R_s . Their estimated values are used below in section 6.3 although they do not affect the results significantly. The calculation of these parameters is to use the same equations for the DSPKF in table 4.1 and equations 4.4 to 4.6.

6.2.1 Parameter estimation results: cell-level

Figure 6.1 and Figure 6.2 show the R_s estimation results of the LTO cell. The data profiles are the same as in section 4.4.1. It can be seen that the estimated R_s can converge with different initial values, to around $0.5 \text{ m}\Omega$, which is the value of R_s obtained experimentally.

Figure 6.3 shows the R_s tracking of the whole battery life of the JGNE NMC cell. Because R_s values of a cell are different at different SOCs, Figure 6.3b shows the R_s values at the fixed SOC (50%) over the whole battery life. The results match the test results from the EIS machine, which starts

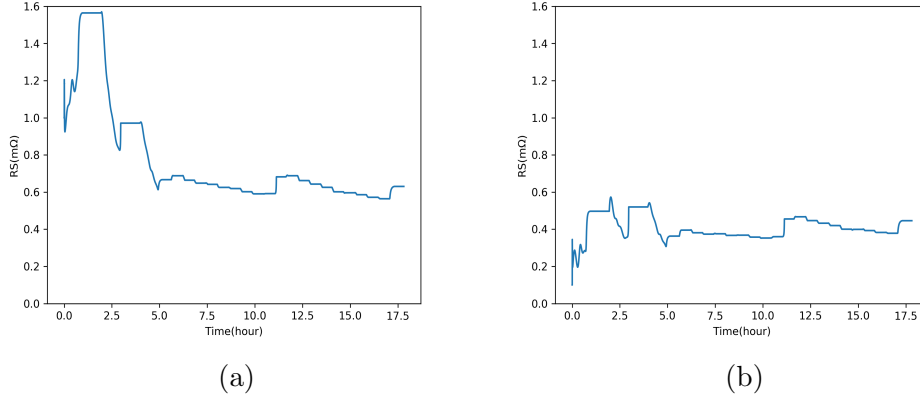


Figure 6.1: LTO cell parameter estimation results of the OCV profile (a) initialise with a value much larger than the experimental value and (b) initialise with value much smaller than the experimental value.

with just over 40 $m\Omega$ and ends with 50 $m\Omega$, as shown in Figure 6.4. The initial R_s value imported to the algorithm is intentionally larger than the expected value to test the robustness of the KF. It can be seen that after approximately 20 cycles the estimated value starts to coincide with the experimental data. This can be faster by further tuning the filter but can cause more fluctuations in the results. Note that both the DSPKF and the EIS machine could over-estimate the R_s value, since the EIS machine’s cable has some impedance and the DSPKF may suffer from the changing OCV-SOC relationship during cycling. Nevertheless, similar to the cell-level SOC and SOH results shown in previous chapters, these cell-level R_s results show the potential of system-level R_s estimation.

6.2.2 Parameter estimation results: WESS

As discussed in chapter 4, the system-level R_s could be 3.3 times larger (about 1.7 $m\Omega$) than the one at the cell-level, based on the topology of how the cells connect in the WESS only (scaled from the cell-level experimental results). However, there is resistance of cables and connections, so the value of system-level R_s is expected to be larger than the calculated value.

Figure 6.5 and Figure 6.6 illustrate R_s estimation of the WESS with

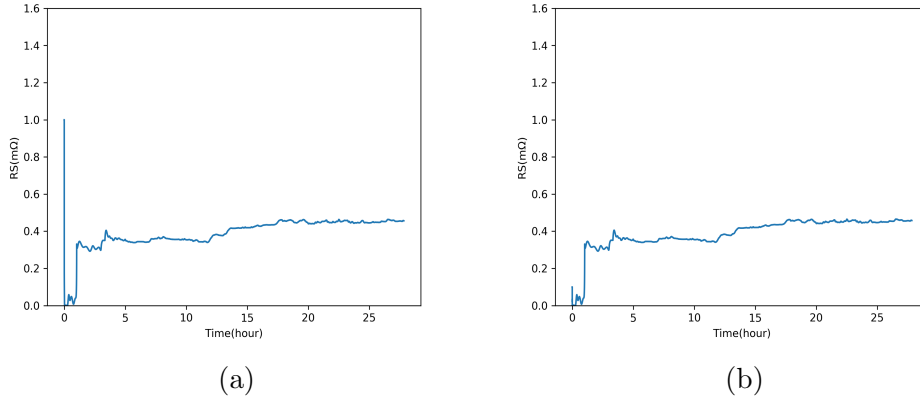
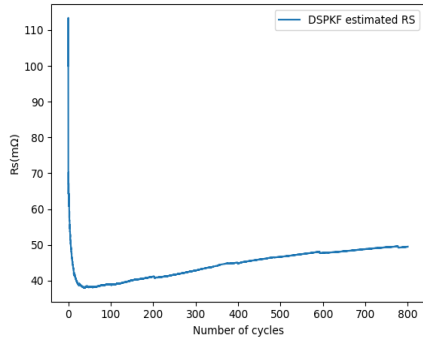


Figure 6.2: LTO cell parameter estimation results of the EFR low profile (a) initialise with a value much larger than the experimental value and (b) initialise with value much smaller than the experimental value.

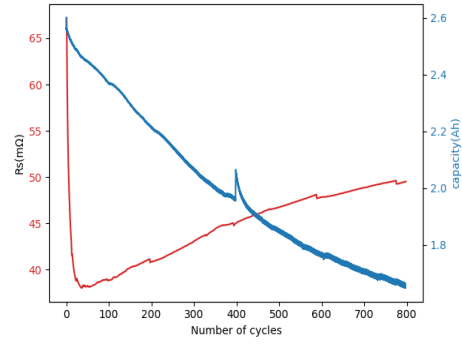
constant cycling and a new profile that has a longer operation time that is shown in Figure 6.7. Both the DSPKF SOC and the BMS SOC, are shown in Figure 6.6a. It can be seen that in both figures the estimated R_s can converge to a value between 2 m Ω and 3 m Ω , which is slightly larger than the calculated value. These results show that R_s estimation of large-scale battery systems is promising.

6.2.3 Parameter estimation results: GS Yuasa BESS

Figure 6.8 shows the R_s tracking of the GS Yuasa BESS, corresponding to the capacity tracking results shown in section 5.6.2. Again according to the topology of this system, the initial R_s for DSPKF initialisation is calculated at 30 m Ω . Both the overall R_s results and the R_s results at the fixed SOC, clearly show an increasing trend, from the calculated initial value, which is expected.

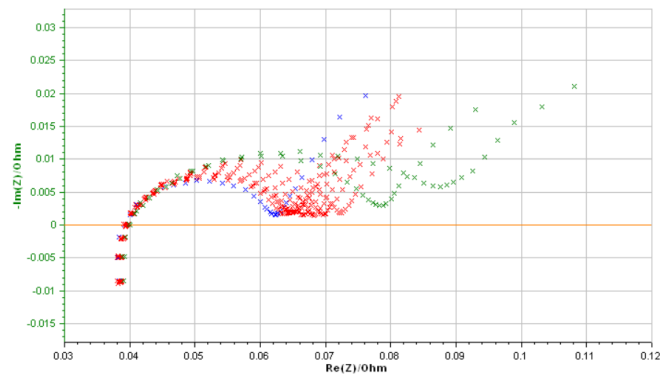


(a)

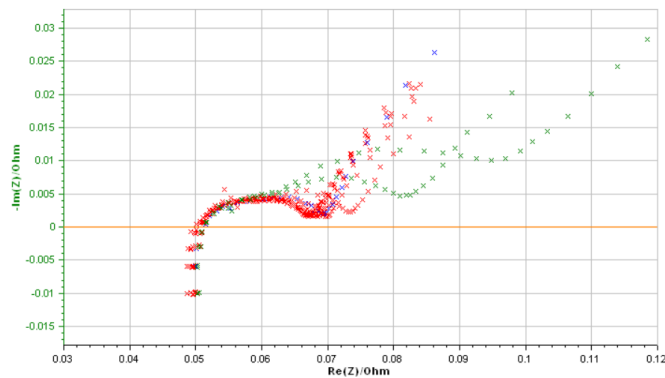


(b)

Figure 6.3: NMC cell R_s tracking (a) of the whole battery life and (b) of the whole battery life at fixed SOC.



(a)



(b)

Figure 6.4: EIS results of (a) a new JGNE NMC cell and (b) a JGNE NMC cell that reached EOL.

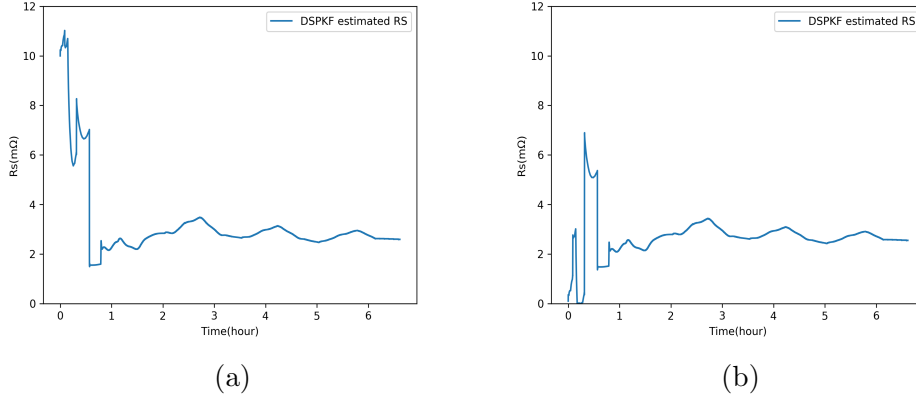


Figure 6.5: WESS parameter estimation with constant cycling (a) initialise with a value much larger than the calculated value and (b) initialise with value much smaller than the calculated value.

6.3 Voltage simulation to validate parameter estimation results

Since the actual values of equivalent circuit model parameters for a large-scale battery system are much harder to obtain than in the cell-level by experiments, the validation of the DSPKF results has to be different. The method introduced in this chapter to validate parameter estimation is to compare simulated terminal voltage that uses estimated ECM parameters against the actual terminal voltage.

6.3.1 Simulation model

The relationship between ECM parameters, SOC, current and terminal voltage is shown in equation 6.1 and equation 6.2, which are derived from equation 4.1 and equation 4.3. For the JGNE cell used in this section, another RC pair is added into equations 6.1 and 6.2. With current data, OCV-SOC relationship, DSPKF estimated ECM parameters and SOC, simulated terminal voltage can be obtained as a comparison with actual values.

$$V_{RC1_k} = V_{RC1_{k-1}} \times e^{\frac{-\Delta t}{\tau_1}} + R_1(1 - e^{\frac{-\Delta t}{\tau_1}}) \quad (6.1)$$

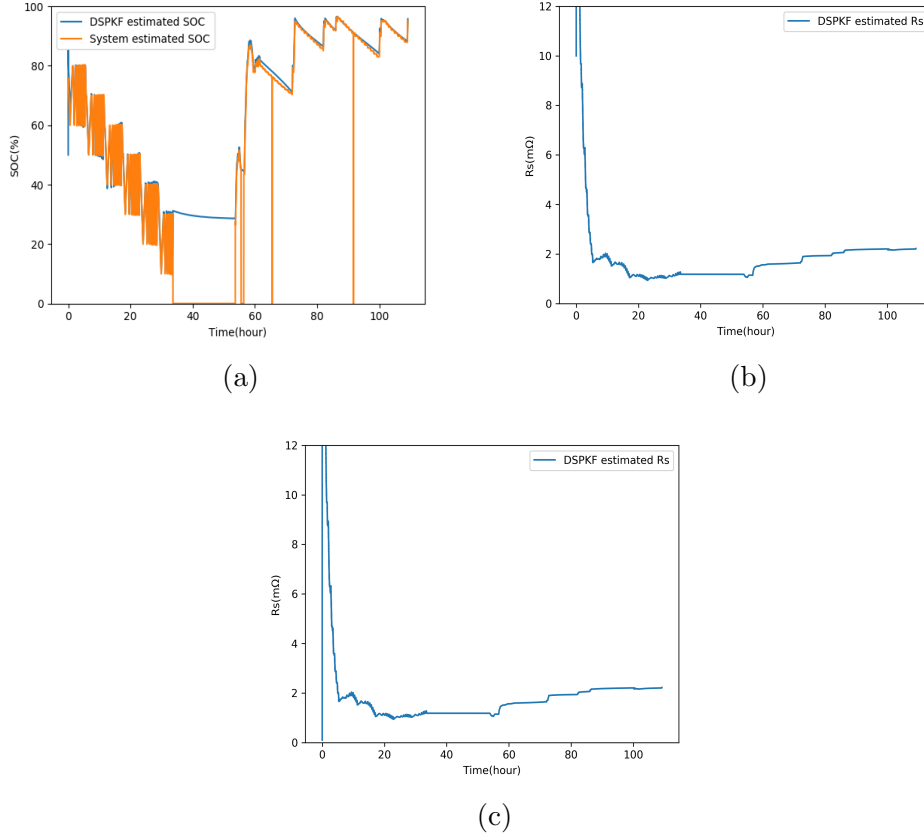


Figure 6.6: WESS parameter estimation with another profile (a) DSPKF and BMS SOC estimations of this profile, (b) initialise with a value much larger than the calculated value and (c) initialise with value much smaller than the calculated value.

$$V_{k_s} = V_{OC}(SOC_k) - R_{1k}I_k - V_{RC1k} \quad (6.2)$$

where V_{k_s} is the simulated terminal voltage to be compared with V_k , the actual terminal voltage, recursively.

6.3.2 Simulation results

The voltage simulation results are shown in this section. Cell-level results are shown first, with the data of the LTO cell and the JGNE NMC cell, after which, voltage simulation results of the WESS are shown. For error

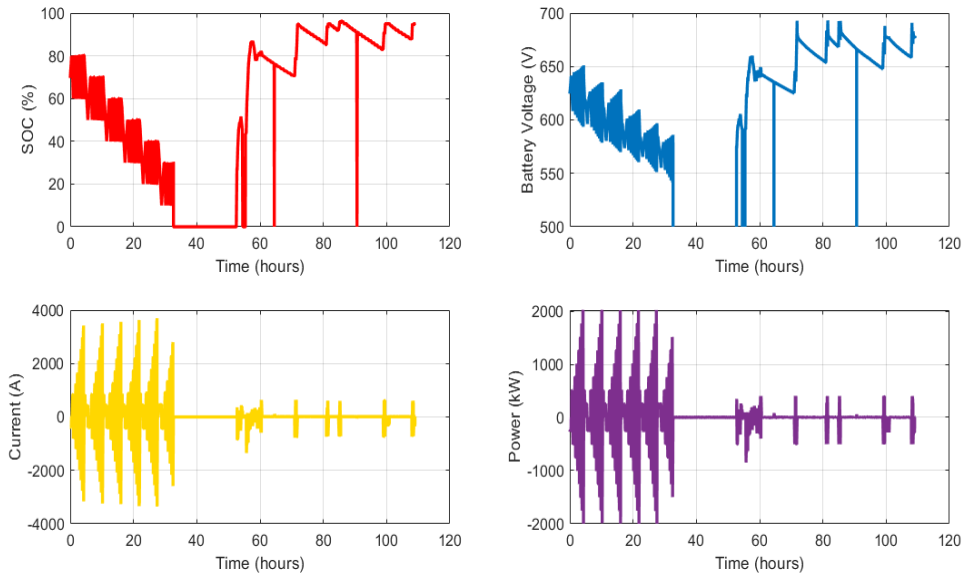
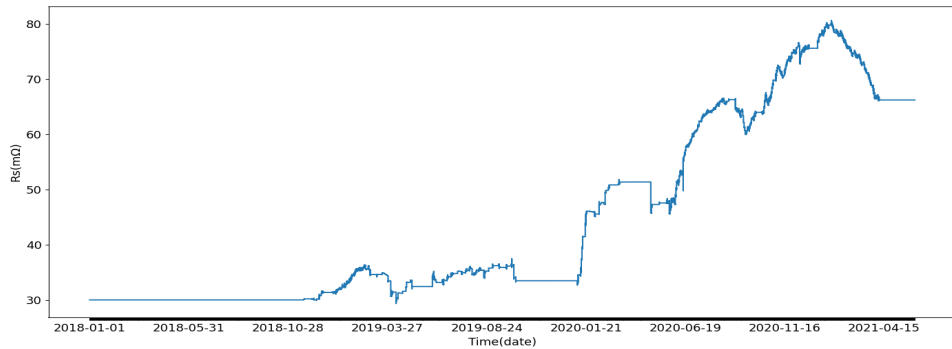
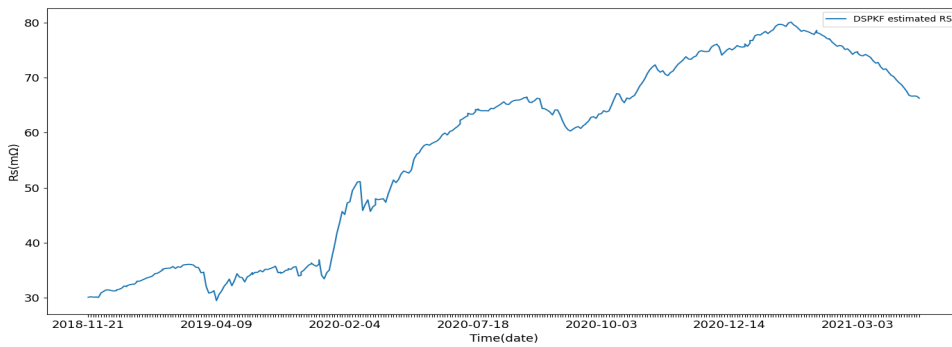


Figure 6.7: WESS operation data with longer operation time



(a)



(b)

Figure 6.8: GS Yuasa BESS R_s tracking (a) of the 3 year operation and (b) of the 3 year operation at fixed SOC.

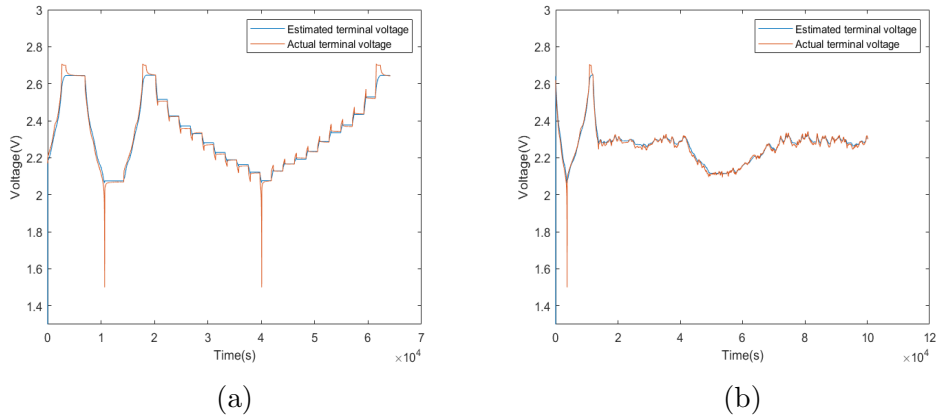


Figure 6.9: Voltage simulation results of an LTO cell from data profiles (a) OCV and (b) EFR low.

evaluation, the RMSEs are calculated with respect to the nominal voltages for the batteries, which are 2.3V, 3.6V and 607.2V for the LTO cell, JGNE cell, and the WESS respectively.

Cell-level results

It can be seen in Figure 6.9, with the same data as in previous chapters, that the calculated terminal voltage values are close to the actual ones with RMSEs of 1.15% and 0.59%. The errors mainly occur when the actual terminal voltage has significant changes, which is considered to be the limitation of the ECM model. The overall small errors indicate that the DSPKF estimated ECM parameters are within acceptable ranges.

Figure 6.10 shows the results of a JGNE NMC cell, which again has a small RMSE of 2.5%. The main errors again occur during the transient periods. Although still acceptable, this value is larger than the results of the LTO cell, and the reason is again assumed to be due to the changing OCV-SOC relationship of the JGNE cell, as discussed in the previous chapter. Although these are only cell-level results, similar to previous chapters, they show that this evaluation method is promising for being used in the system level.

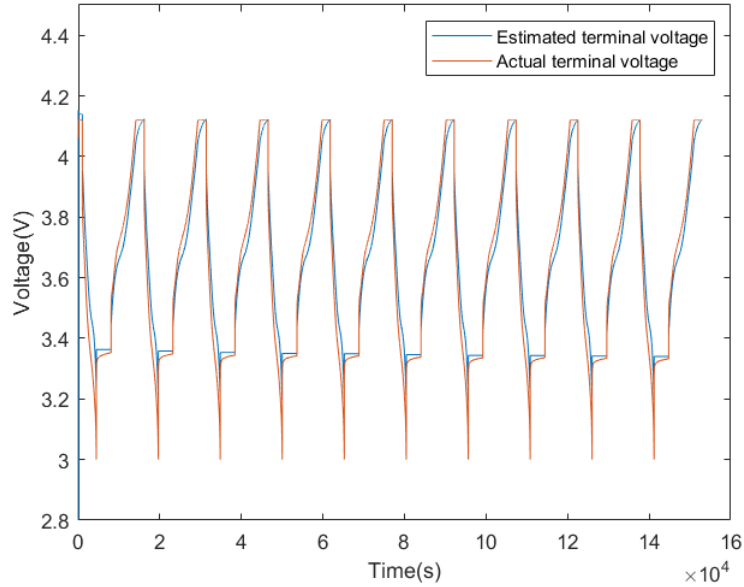


Figure 6.10: Voltage simulation results of the JGNE cell.

System-level results

System-level results are shown in this section with the same data profiles introduced above. In every profile, the actual terminal voltage, simulated voltage using DSPKF SOC and simulated voltage using BMS SOC are shown in the same figure. For the results using DSPKF SOC, the RMSEs of these profiles are 1.2%, 0.24% and 0.7% respectively. While for the results using BMS SOC, the RMSEs are 1.5%, 0.47% and 0.7% respectively. It can be seen that the errors are not much larger than in the cell-level, considering the more complex structure of the system, the less accurate data and a relatively less accurate model. Specifically, both the voltage simulation errors of the LTO cell and the WESS are less than 1.5%, and only the system-level errors using constant cycling are slightly larger than the cell-level counterparts.

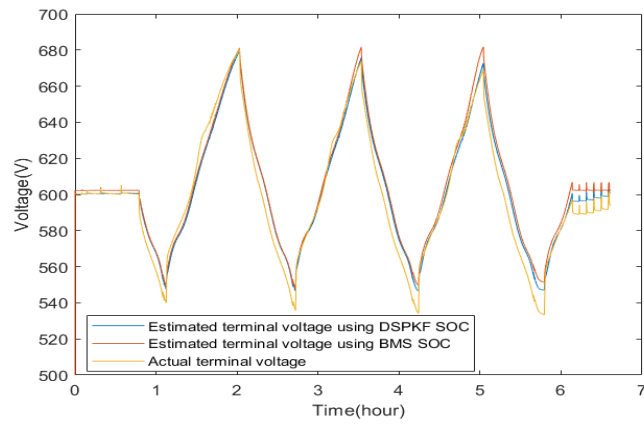
However, the successful simulation in the system-level can only indicate that the parameters are within the right range of values because other values that are close to the DSPKF estimated parameters have also been tried and the simulation results barely change. The SOC values are more essential for the accuracy of simulated terminal voltage due to the relationship between

SOC and OCV, which is the dominant part of calculating terminal voltage.

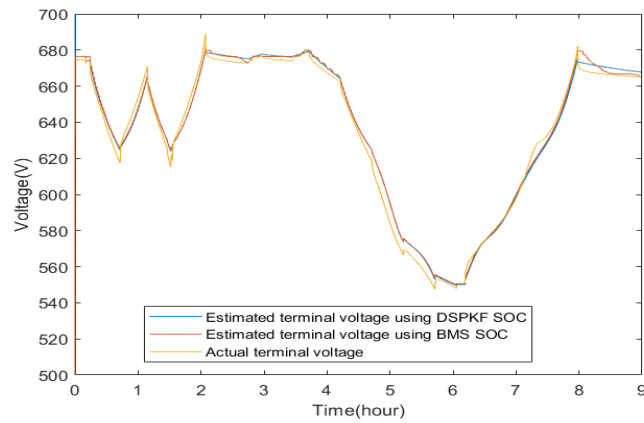
6.4 Conclusions

This chapter demonstrates successful system-level ECM parameter estimation using the DSPKF. The estimated R_s can converge to a reasonable value despite wrong initial values. The parameter estimation results are further evaluated by the voltage simulation. The simulated terminal voltage is calculated recursively by using estimated ECV parameters, SOC and current, to be compared with the actual terminal voltage.

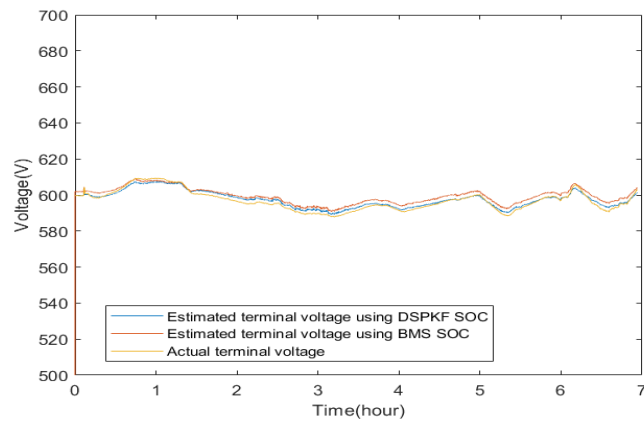
The accuracy of parameter estimation could be better evaluated if another evaluation method can be implemented at the system-level. Pseudorandom binary sequence (PRBS)[128], has been implemented in the cell-level, and it has been tried at the system-level but unsuccessfully, due to the fact that the current data of the WESS is updated much slower than at the cell-level. Future work could be conducted with access to faster data from either the WESS or other BESSs.



(a)



(b)



(c)

Figure 6.11: Voltage simulation results of an WESS with different profiles, using DSPKF SOC and BMS SOC (a) constant cycling, (b) mixed profile and (c) dynamic frequency response.

Chapter 7

Conclusions & Further Work

This work aims to provide methods for estimating the state and ECM parameters of BESSs, which are essential for maximising their technical potential and return on investment. It has been proposed, and experimentally validated, that by modelling a BESS as a single cell it is possible to achieve an accurate estimation of SOC and capacity for the entire system. The ECM parameter estimation has also been achieved by the DSPKF and validated by terminal voltage simulation, although evaluating the accuracy further is a possibility of future research. The advantage of these methods is that they respect the limits of data measurement accuracy and granularity in the real-world application as BESSs are scaled-up. Another advantage of this methodology compared to alternative approaches where cell-level models are scaled-up, is that this approach is significantly less computationally demanding and requires minimal cell-level knowledge. For example, it is shown that either the OCV-SOC relationship measured at the system-level or cell-level (and scaled appropriately) can be used, making this methodology suitable for situations where cell testing/data is not available.

The techniques for dealing with the invalid-data problem for SOC estimation using the KF methods are essential. Besides, it is clear that data selection is necessary, particularly for capacity estimation to achieve convergence and accurate results. The selection criteria and the techniques for optimal selection are presented in this thesis. The parameters of the DSPKF

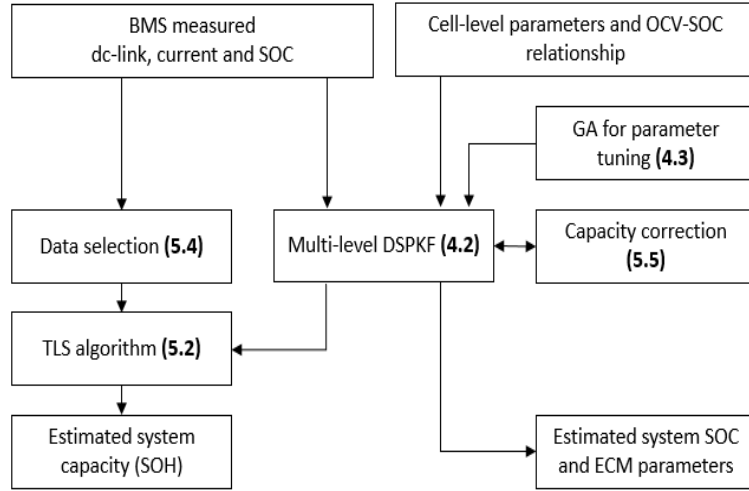


Figure 7.1: Battery system state estimation flowchart

are tuned by the GA to avoid time-consuming manual tuning work but more importantly it has been demonstrated to provide repeatable results in the general case. WESS efficiency calculations are conducted to compare the KF methods and the BMS SOC to investigate the accuracy of the results. The results show that the DSPKF SOC has greater accuracy than the BMS SOC, and the RTE of a BESS is affected by the C-rate significantly, as expected. To make the TLS algorithm suitable for the case where only system power is available, rather than the system-level current, a novel TLS algorithm is presented and analysed showing that in this case a mapping of inverter efficiency against power is required to achieve accurate results.

The overall methodologies of this work have been illustrated in Figure 7.1. The SOC, capacity and parameters algorithms have been implemented in real-time on the WESS and have provided reliable accurate results once the novel approaches to data selection have been implemented. This work not only presents the state and parameter estimation results of the WESS, but also the results of another BESS, GS Yuasa, although with limited information, which is a strong validation of the effectiveness of the algorithms.

In Figure 3.6b, it can be seen that the temperature differences between racks are significant, although the average temperature of all the cells is

within a narrower range. There are evident differences in temperature between operation modes. According to the mathematics shown in previous chapters, the accuracy of the KF methods and the TLS algorithm should not be affected by the temperature variations of a BESS and this graph further helps to prove that, because from the results shown in this thesis and the online tracking results the accuracy of the algorithms are not affected by different operating modes, i.e., different temperatures.

Future work will be required to assess the effectiveness of the capacity estimation further with more other degraded BESSs. More estimation of equivalent circuit parameters should be done, especially the series resistor, for degradation modelling and end of life prediction.

Kalman filter methods have been proved to be able to estimate battery capacity at the cell-level, but in this work it has not been achieved at the system-level using WESS data. The reasons may be the quality of the system-level data, and/or the ECM accuracy. Future work is needed to further investigate the reason and try to achieve system-level capacity estimation using KF methods, which should be a more advanced approach than the capacity correction technique proposed in this work.

From the capacity tracking results discussed in chapter 5, it can be concluded that the OCV-SOC relationship plays a significant role in the accuracy of the DSPKF algorithm. There are encouraging results from the WESS which could be because of the quality and the relatively linear OCV-SOC relationship of the LTO cells, because the accuracy of the algorithms decays even in cell-level results of the NMC cell. Thus, future work should aim at improving system-level OCV-SOC relationships of other BESSs with other chemistries.

References

- [1] M. Kampa and E. Castanas, “Human health effects of air pollution,” *Journal of The Electrochemical Society*, vol. 151, pp. 362–367, 2008.
- [2] O. Goksu, R. Teodorescu, C. L. Bak, F. Iov, and P. C. Kjaer, “Instability of wind turbine converters during current injection to low voltage grid faults and PLL frequency based stability solution,” *IEEE Transactions on Power Systems*, vol. 29, p. 1683–1691, 2014.
- [3] B. Xu, S. Member, Y. Shi, and S. Member, “Optimal battery participation in frequency regulation markets,” *IEEE Trans. Power Syst.*, vol. 33, no. 6, pp. 6715–6725, 2018.
- [4] B. Gundogdu, S. Nejad, D. T. Gladwin, M. Foster, and D. Stone, “A battery energy management strategy for uk enhanced frequency response and triad avoidance,” *IEEE Trans. Ind. Electron.*, vol. 65, pp. 9509 – 9517, 2018.
- [5] M. A. Hannan, M. S. H. Lipu, A. Hussain, and A. Mohamed, “A review of lithium-ion battery state of charge estimation and management system in electric vehicle applications: Challenges and recommendations,” *Renew. Sustain. Energy Rev.*, vol. 78, pp. 834–854, October 2017.
- [6] R. Xiong, L. Li, and J. Tian, “Towards a smarter battery management system: A critical review on battery state of health monitoring methods,” *Journal of Power Sources*, vol. 405, pp. 18–29, November 2018.

- [7] Z. Wang, D. T. Gladwin, M. J. Smith, and S. Haass, “Practical state estimation using kalman filter methods for large-scale battery systems,” *Applied Energy*, vol. 294, 2021. doi: 10.1016/j.apenergy.2021.117022.
- [8] L. F. Nazar, M. Cuisinier, and Q. Pang, *Lithium-sulfur batteries*, vol. 39. 2014.
- [9] D. Pavlov, *Lead-acid batteries: science and technology*. Elsevier, 2011.
- [10] M. Li, J. Lu, *et al.*, “30 years of lithium-ion batteries,” *Advanced Materials*, 2018. doi: 10.1002/adma.201800561.
- [11] B. Scrosati, J. Hassoun, and Y. Sun, “Lithium-ion batteries. a look into the future,” *Energy Environ. Sci*, p. 3287–3295, 2011. doi: 10.1039/c1ee01388b.
- [12] M. B. Pinson and M. Z. Bazant, “Theory of SEI formation in rechargeable batteries: Capacity fade, accelerated aging and lifetime prediction,” *J. Electrochem. Soc.*, vol. 160, pp. A243–A250, 2013.
- [13] C. Sandhya, B. John, and C. Gouri, “Lithium titanate as anode material for lithium-ion cells: a review,” *Ionics*, p. 601–620, 2014. doi: 10.1007/s11581-014-1113-4.
- [14] K. Chayambuka, G. Mulder, *et al.*, “Sodium-ion battery materials and electrochemical properties reviewed,” *Advanced energy materials*, March 2018. doi: 10.1002/aenm.201800079.
- [15] D. A. Stevens and J. R. Dahn, “High capacity anode materials for rechargeable sodium-ion batteries,” *Journal of The Electrochemical Society*, vol. 147(4), pp. 1271–1273, 2000. doi: 10.1002/sm11.201702514.
- [16] A. M. Skundin, T. L. Kulova, and A. B. Yaroslavtsev, “Sodium-ion batteries (a review),” *Russian Journal of Electrochemistry*, vol. 54, pp. 131–174, March 2017.
- [17] Y. Liang, W. Lai, *et al.*, “Nanocomposite materials for the sodium-ion battery: A review,” *Small*, 2018. doi: 10.1002/aenm.201800079.

- [18] J. T. Kummer and N. Weber, “A sodium-sulfur secondary battery,” *SAE Trans*, vol. 76, pp. 1003–1007, 1968.
- [19] X. Hu, C. Zou, C. Zhang, and Y. Li, “Technological developments in batteries: A survey of principal roles, types, and management needs,” *IEEE Power Energy Mag*, vol. 15, pp. 20–31, October 2017.
- [20] K. B. Hueso, M. Armand, Q. Luo, and T. Rojo, “High temperature sodium batteries: status, challenges and future trends†,” *Energy Environ. Sci*, vol. 6, pp. 734–749, 2013.
- [21] Y. Shi, C. Eze, *et al.*, “Recent development of membrane for vanadium redox flow battery applications: A review,” *Applied Energy*, vol. 238, pp. 202–224, 2019.
- [22] A. Hazza, D. Pletcher, and R. wills, “A novel flow battery: A lead acid battery based on an electrolyte with soluble lead(ii) part i. preliminary studies,” *Journal of The Electrochemical Society*, vol. 6, pp. 1773–1778, 2004.
- [23] W. Wang, Q. Luo, *et al.*, “Recent progress in redox flow battery research and development,” *Advanced Functional Materials*, vol. 23, pp. 970–986, 2013.
- [24] Y. Hu, W. Chen, *et al.*, “Strategies toward high-loading lithium–sulfur battery,” *Advanced Energy Materials*, 2020. doi: 10.1002/aenm.202000082.
- [25] N. Jayaprakash, J. Shen, *et al.*, “Porous hollow carbon sulfur composites for high-power lithium–sulfur batteries,” *Comuunications*, May 2011. doi: 10.1002/anie.201100637.
- [26] S. P. S. Badwal, S. S. Giddey, C. Munnings, I. Bhatt, I., and A. F. Hollenkamp, *Emerging electrochemical energy conversion and storage technologies*. September 2014. doi: 10.3389/fchem.2014.00079.

- [27] G. Girishkumar, B. McCloskey, A. C. Luntz, S. Swanson, and W. Wilcke, “Lithium-air battery: Promise and challenges,” *J. Phys. Chem. Lett.*, vol. 1, no. 14, pp. 2193–2203, 2010.
- [28] N. Imanishi and O. Yamamoto, “Perspectives and challenges of rechargeable lithium-air batteries,” *Materials Today Advances*, vol. 4, September 2019. doi: 10.1016/j.mtadv.2019.100031.
- [29] Z. Guo, C. Li, *et al.*, “A long-life lithium–air battery in ambient air with a polymer electrolyte containing a redox mediator,” *Electrochemistry*, 2017. doi: 10.1002/anie.201701290.
- [30] Y. Kato, S. Hori, *et al.*, “High-power all-solid-state batteries using sulfide superionic conductors,” *Nature energy*, vol. 1, 2016.
- [31] Y. Lee, S. Fujiki, *et al.*, “High-energy long-cycling all-solid-state lithium metal batteries enabled by silver–carbon composite anodes,” *Nature Energy*, vol. 5, 2020.
- [32] Y. Xiao, Y. Wang, *et al.*, “Understanding interface stability in solid-state batteries,” *Nature Reviews Materials*, vol. 5, p. 105–126, 2020.
- [33] E. Stringham, J. Miller, and J. Clark, “Overcoming barriers to entry in an established industry: Tesla motors,” *California Management Review*, vol. 57, 2015.
- [34] Bloomberg, “The breakneck rise of china’s colossus of electric-car batteries.” <https://www.bloomberg.com/news/features/2018-02-01/the-breakneck-rise-of-china-s-colossus-of-electric-car-batteries>, 2018.
- [35] National grid, “Frequency response services,” 2021. <https://www.nationalgrideso.com/industry-information/balancing-services/frequency-response-services>.
- [36] B. Dunn, H. Kamath, and J. Tarascon, “Electrical energy storage for the grid: A battery of choices,” *Sci. Mag*, vol. 334, no. 6058, pp. 928–936, 2011.

- [37] M. Armand and J.-M. Tarascon, “Building better batteries,” *Nature*, vol. 451, pp. 652–657, 2008.
- [38] D. Su, A. McDonagh, S. Z. Qiao, and G. Wang, “High-capacity aqueous potassium-ion batteries for large-scale energy storage,” *Adv. Mater.*, vol. 29, 2017. doi: 10.1002/adma.201604007.
- [39] L. Li, S. Kim, W. Wang, *et al.*, “A stable vanadium redox-flow battery with high energy density for large-scale energy storage,” *Adv. Energy Mater.*, vol. 1, no. 3, pp. 394–400, 2011.
- [40] L. Ahmadi, S. B. Young, M. Fowler, R. A. Fraser, and M. A. Achachlouei, “A cascaded life cycle: reuse of electric vehicle lithium-ion battery packs in energy storage systems,” *Int. J. Life Cycle Assess.*, vol. 22, no. 1, pp. 111–124, 2017.
- [41] J. M. Reniers, G. Mulder, S. Ober-Blobaum, and D. A. Howey, “Improving optimal control of grid-connected lithium-ion batteries through more accurate battery and degradation modelling,” *Journal of Power Sources*, vol. 379, pp. 91–102, 2018.
- [42] O. Ekren and B. Y. Ekren, “Size optimization of a PV/wind hybrid energy conversion system with battery storage using simulated annealing,” *Applied Energy*, vol. 87, no. 2, pp. 592–598, 2010.
- [43] B. Zhao, X. Zhang, J. Chen, C. Wang, and L. Guo, “Operation optimization of standalone microgrids considering lifetime characteristics of battery energy storage system,” *IEEE Trans. Sustain. Energy*, vol. 4, pp. 934–943, October 2013.
- [44] K. S. Ng, C.-S. Moo, Y.-P. Chen, and Y.-C. Hsieh, “Enhanced coulomb counting method for estimating state-of-charge and state-of-health of lithium-ion batteries,” *Applied Energy*, vol. 86, pp. 1506–1511, September 2009.
- [45] W. Chang, “The state of charge estimating methods for battery: a review,” *ISRN Appl Math*, 2013. doi: 10.1155/2013/953792.

- [46] G. L. Plett, “Extended Kalman filtering for battery management systems of LiPB-based HEV battery packs - part 1. modeling and identification,” *Journal of Power Sources*, vol. 134, pp. 262–276, August 2004.
- [47] G. L. Plett, “Sigma-point Kalman filtering for battery management systems of LiPB-based HEV battery packs part 1: Introduction and state estimation,” *Journal of Power Sources*, vol. 161, no. 2, pp. 1356–1368, 2006.
- [48] M. Nørgaard, N. K. Poulsen, and O. Ravn, “New developments in state estimation for nonlinear systems,” *Automatica*, vol. 36, pp. 1627–1638, 2000.
- [49] G. L. Plett, “Sigma-point Kalman filtering for battery management systems of LiPB-based HEV battery packs part 2: Simultaneous state and parameter estimation,” *Journal of Power Sources*, vol. 161, no. 2, pp. 1369–1384, 2006.
- [50] G. L. Plett, “Extended Kalman filtering for battery management systems of LiPB-based HEV battery packs, part 3: State and parameter estimation,” *Journal of Power Sources*, vol. 134, pp. 277–292, August 2004.
- [51] Y. Zou, X. Hu, H. Ma, and S. E. Li, “Combined state of charge and state of health estimation over lithium-ion battery cell cycle lifespan for electric vehicles,” *Journal of Power Sources*, vol. 273, pp. 793–803, January 2015.
- [52] C. Hu, B. D. Youn, and J. Chung, “A multiscale framework with Extended Kalman Filter for lithium-ion battery SOC and capacity estimation,” *Applied Energy*, vol. 92, pp. 694–704, 2012.
- [53] R. E. Kalman, “A new approach to linear filtering and prediction problems,” *Journal of Basic Engineering*, vol. 82, pp. 35–45, 1960.

- [54] X. Hu, S. Li, Z. Jia, and B. Egardt, “Enhanced sample entropy-based health management of li-ion battery for electrified vehicles,” *Energy*, vol. 64, pp. 953–960, January 2014.
- [55] R. Hecht-Nielsen, “Theory of the backpropagation neural network,” *Neural Networks for Perception*, pp. 65–93, 1992.
- [56] A. A. Hussein, “Kalman filters versus neural networks in battery state-of-charge estimation: A comparative study,” *Int. J. Modern Nonlin. Technol. Appl.*, vol. 3, pp. 199–209, December 2004.
- [57] I. Snihir, W. Rey, *et al.*, “Battery open-circuit voltage estimation by a method of statistical analysis,” *Journal of Power Sources*, vol. 159, pp. 1484–1487, 2006.
- [58] L. Zheng, L. Zhang, *et al.*, “Co-estimation of state-of-charge, capacity and resistance for lithium-ion batteries based on a high-fidelity electrochemical model,” *Applied Energy*, vol. 180, pp. 424–484, 2016.
- [59] W. Dreyer, J. Jamnik, *et al.*, “The thermodynamic origin of hysteresis in insertion batteries,” *Nature Materials*, vol. 9, pp. 448–453, 2010.
- [60] L. Ran, J. Wu, H. Wang, and G. Li, “Prediction of state of charge of lithium-ion rechargeable battery with electrochemical impedance spectroscopy theory,” *5th IEEE Conf Ind Electron Appl*, pp. 684–688, 2010.
- [61] U. Westerhoff, T. Kroker, K. Kurbach, and M. Kurrat, “Electrochemical impedance spectroscopy based estimation of the state of charge of lithium-ion batteries,” *Journal of Energy Storage*, vol. 8, pp. 244–256, 2016.
- [62] M. Charkhgard and M. Farrokhi, “State-of-charge estimation for lithium-ion batteries using neural networks and EKF,” *IEEE Trans. Ind. Electron.*, vol. 57, no. 12, pp. 4178–4187, 2010.
- [63] B. Pattipati, B. Balasingam, G. V. Avvari, K. R. Pattipati, and Y. Bar-Shalom, “Open circuit voltage characterization of lithium-ion batteries,” *Journal of Power Sources*, vol. 269, pp. 317–333, July 2014.

- [64] P. Spagnol, S. Rossi, and S. M. Savaresi, "Kalman filter SoC estimation for li-ion batteries," in *Proc. IEEE Int.*, pp. 587–592, September 2011.
- [65] A. J. Salkind, C. Fennie, P. Singh, T. Atwater, and D. E. Reisner, "Determination of state-of-charge and state-of-health of batteries by fuzzy logic methodology," *Journal of Power Sources*, vol. 80, pp. 293–300, July 1999.
- [66] M. Charkhgard and M. Farrokhi, "State-of-charge estimation for lithium-ion batteries using neural networks and EKF," *IEEE Trans. Ind. Electron.*, vol. 57, pp. 4178–4187, 2010.
- [67] R. Xiong, J. Cao, *et al.*, "Critical review on the battery state of charge estimation methods for electric vehicles," *IEEE access*, vol. 6, pp. 1832–1843, 2017.
- [68] X. Hu, J. Jiang, D. Cao, and B. Egardt, "Battery health prognosis for electric vehicles using sample entropy and sparse Bayesian predictive modeling," *IEEE Trans. Ind. Electron.*, vol. 63, pp. 2645–2656, April 2016.
- [69] J. Vetter, P. Novak, M. R. Wagner, C. Veit, K.-C. M"oller, J. Besenhard, M. Winter, M. Wohlfahrt-Mehrens, C. Vogler, and A. Hammouche, "Ageing mechanisms in lithium-ion batteries," *Journal of Power Sources*, vol. 147, pp. 269–281, September 2005.
- [70] S. K. Spurgeon, "Sliding mode observers: a survey," *International Journal of Systems Science*, vol. 39, no. 8, pp. 751–764, 2008. doi: 10.1080/00207720701847638.
- [71] M. E. Y. Xing *et al.*, "A case study on battery life prediction using particle filtering," *Proceedings of the IEEE 2012 Prognostics and System Health Management Conference (PHM-2012 Beijing)*, 2012.
- [72] J. Remmlinger, M. Buchholz, *et al.*, "State-of-health monitoring of lithium-ion batteries in electric vehicles by on-board internal resistance estimation," *Journal of Power Sources*, pp. 487–494, 2006.

- [73] D. Store, M. Swierczynski, *et al.*, “Behavior and state-of-health monitoring of li-ion batteries using impedance spectroscopy and recurrent neural networks,” *2014 IEEE Energy Conversion Congress and Exposition (ECCE)*, 2014.
- [74] K. Tseng, J. Liang, *et al.*, “Regression models using fully discharged voltage and internal resistance for state of health estimation of lithium-ion batteries,” *2014 IEEE Energy Conversion Congress and Exposition (ECCE)*, 2015.
- [75] A. Eddahech, O. Briat, *et al.*, “Behavior and state-of-health monitoring of li-ion batteries using impedance spectroscopy and recurrent neural networks,” *Electrical Power and Energy Systems*, pp. 487–494, 2006.
- [76] J. Christensen and J. Newman, “Effect of anode film resistance on the charge/discharge capacity of a lithium-ion battery,” *J. Electrochem. Soc.*, vol. 150, no. 11, pp. A1416–A1420, 2003.
- [77] J. Christensen and J. Newman, “A mathematical model for the lithium-ion negative electrode solid electrolyte interphase,” *J. Electrochem. Soc.*, vol. 151, no. 11, pp. A1977–A1988, 2004.
- [78] M. Safari and C. Delacourt, “Simulation-based analysis of ageing phenomena in a commercial graphite/LiFePO₄ cell,” *J. Electrochem. Soc.*, vol. 158, no. 12, pp. A1436–A1447, 2011.
- [79] J. Wang, P. Liu, *et al.*, “Cycle-life model for graphite-lifepo₄ cells,” *Journal of Power Sources*, vol. 196, pp. 3942–3948, April 2011.
- [80] M. Safari, M. Morcrette, A. Teyssot, and C. Delacourt, “Life-prediction methods for lithium-ion batteries derived from a fatigue approach i. introduction: Capacity-loss prediction based on damage accumulation,” *J. Electrochem. Soc.*, vol. 157, no. 6, pp. A713–A720, 2010.
- [81] M. Petit, E. Prada, and V. Sauvant-Moynot, “Development of an empirical ageing model for li-ion batteries and application to assess the

- impact of vehicle-to-grid strategies on battery lifetime,” *Appl. Energy*, vol. 172, pp. 398–407, June 2016.
- [82] W. Kempton and J. Tomić, “Vehicle-to-grid power implementation: From stabilizing the grid to supporting large-scale renewable energy,” *Journal of Power Sources*, vol. 144, pp. 280–294, 2005.
- [83] B. Xu, A. Oudalov, A. Ulbig, G. Andersson, and D. Kirschen, “Modeling of lithium-ion battery degradation for cell life assessment,” *IEEE Trans. Smart Grid*, vol. pp, no. 99, pp. 1–1, 2016.
- [84] M. Rezvani, M. AbuAli, S. Lee, and J. Lee, “A comparative analysis of techniques for electric vehicle battery prognostics and health management (PHM),” *Soc. Automotive Eng (SAE) Int., Chicago*, 2011. doi: 10.4271/2011-01-2247.
- [85] W. He, N. Williard, M. Osterman, and M. Pecht, “Prognostics of lithium-ion batteries based on Dempster-Shafer theory and the Bayesian monte carlo method,” *Journal of Power Sources*, vol. 196, pp. 10 314–10 321, December 2011.
- [86] M.-W. Cheng, S.-M. Wang, Y.-S. Lee, and S.-H. Hsiao, “Fuzzy controlled fast charging system for lithium-ion batteries,” *IEEE Power Electronics and Drive Systems*, pp. 1498–1503, 2009. doi: 10.1109/PEDS.2009.5385724.
- [87] A. Barré, B. Deguilhem, S. Grolleau, M. Gérard, F. Suard, and D. Riu, “A review on lithium-ion battery ageing mechanisms and estimations for automotive applications,” *Journal of Power Sources*, vol. 241, pp. 680– 689, 2013.
- [88] L. Zheng, J. Zhu, D. D. Lu, G. Wang, and T. He, *Incremental capacity analysis and differential voltage analysis based state of charge and capacity estimation for lithium-ion batteries*, vol. 150. 2018.

- [89] B. Wu, V. Yufit, and others., “Differential thermal voltammetry for tracking of degradation in lithium-ion batteries,” *Journal of Power Sources*, vol. 273, pp. 495–501, January 2015.
- [90] C. Weng, Y. Cui, *et al.*, “On-board state of health monitoring of lithium-ion batteries using incremental capacity analysis with support vector regression,” *Journal of Power Sources*, vol. 235, pp. 36–44, 2013.
- [91] A. Barré, F. Suard, M. Gérard, M. Montaru, and D. Riu, “Statistical analysis for understanding and predicting battery degradations in real life electric vehicle use,” *Journal of Power Sources*, vol. 245, pp. 846–856, January 2014.
- [92] F. S. A. Barré *et al.*, “Statistical analysis for understanding and predicting battery degradations in real-life electric vehicle use,” *Journal of Power Sources*, vol. 245, pp. 846–856, 2014.
- [93] A. Farmann, W. Waag, A. Marongiu, and D. U. Sauer, “Critical review of on-board capacity estimation techniques for lithium-ion batteries in electric and hybrid electric vehicles,” *Journal of Power Sources*, vol. 281, pp. 114–130, May 2015.
- [94] G. L. Plett, “Recursive approximate weighted total least squares estimation of battery cell total capacity,” *Journal of Power Sources*, vol. 196, no. 4, pp. 2319–2331, 2011.
- [95] P. Ramadass, B. Haran, P. M. Gomadam, R. E. White, and B. N. Popov, “Development of first principles capacity fade model for li ion cells,” *J. Electrochem. Soc.*, vol. 151, pp. A196–A203, 2004.
- [96] R. Spotnitz, “Simulation of capacity fade in lithium-ion batteries,” *Journal of Power Sources*, vol. 113, no. 1, pp. 72–80, 2003.
- [97] K. H. Tseng, J. W. Liang, W. Chang, and S. C. Huang, “Regression models using fully discharged voltage and internal resistance for state of health estimation of lithium-ion batteries,” *Energies*, vol. 8, no. 4, pp. 2889–2907, 2015.

- [98] J.-S. Jang, C.-T. Sun, and E. Mizutani, *Neuro-Fuzzy and Soft Computing-A Computational Approach to Learning and Machine Intelligence*. IEEE Transactions on Automatic Control, 1997.
- [99] P. A. Topan, M. N. Ramadan, G. Fathoni, A. I. Cahyadi, and O. Wahyunggoro, “Fuzzy logic modelling of state-of-charge and available capacity of nickel/metal hydride batteries,” *Journal of Power Sources*, vol. 136, p. 322–333, 2004.
- [100] P. A. Topan, M. N. Ramadan, G. Fathoni, A. I. Cahyadi, and O. Wahyunggoro, “State of charge (soc) and state of health (soh) estimation on lithium polymer battery via kalman filter,” *2016 2nd International Conference on Science and Technology-Computer (ICST)*, pp. 93–96, 2016.
- [101] R. R. Richardson, M. A. Osborne, and D. A. Howey, “Gaussian process regression for forecasting battery state of health,” *Journal of Power Sources*, vol. 357, pp. 209–219, 2017.
- [102] X. Su, S. Wang, M. Pecht, L. Zhao, and Z. Ye, “Interacting multiple model particle filter for prognostics of lithium-ion batteries,” *Microelectron. Reliab.*, vol. 70, pp. 59–69, 2017.
- [103] H. Li, D. Pan, and C. L. P. Chen, “Intelligent prognostics for battery health monitoring using the mean entropy and relevance vector machine,” *IEEE Trans. Syst. Man Cybern.*, vol. 44, no. 7, pp. 851–862, 2014.
- [104] W. Xian, B. Long, M. Li, and H. Wang, “Prognostics of lithium-ion batteries based on the verhulst model, particle swarm optimization and particle filter,” *IEEE Trans. Instrum. Meas*, vol. 63, no. 1, pp. 2–17, 2014.
- [105] W. He and N. Williard, “Prognostics of lithium-ion batteries based on dempster–shafer theory and thebayesian monte carlo method,” *Journal of Power Sources*, vol. 196, pp. 10314–10321, 2011.

- [106] J. Zhang and J. Lee, “A review on prognostics and health monitoring of li-ion battery,” *Journal of Power Sources*, vol. 196, pp. 6007–6014, 2011.
- [107] G. L. Plett, “Efficient battery pack state estimation using Bar-Delta filtering,” *EVS24 International Battery, Hybrid and Fuel Cell Electric Vehicle Symposium*, 2009.
- [108] H. Dai, X. Wei, Z. Sun, J. Wang, and W. Gu, “Online cell soc estimation of li-ion battery packs using a dual time-scale kalman filtering for ev applications,” *Applied Energy*, vol. 95, p. 227–237, 2012.
- [109] R. Xiong, F. Sun, X. Gong, and H. He, “Adaptive state of charge estimator for lithium-ion cells series battery pack in electric vehicles,” *Journal of Power Sources*, vol. 242, pp. 699–713, 2013.
- [110] W. Li, M. Rentemelster, J. Badede, D. Jost, and D. Schulte, “Digital twin for battery systems: Cloud battery management system with on-line state-of-charge and state-of-health estimation,” *Journal of Energy Storage*, vol. 30, 2020. doi: 10.1016/j.est.2020.101557.
- [111] J. Hernández, F. Sanchez-Sutil, and F. Muñoz-Rodríguez, “Design criteria for the optimal sizing of a hybrid energy storage system in PV household-prosumers to maximize self-consumption and selfsufficiency,” *Energy*, vol. 186, 2019. doi: 10.1016/j.energy.2019.07.157.
- [112] J. Hernández, F. Sanchez-Sutila, F. Muñoz-Rodríguez, and C. Baier, “Optimal sizing and management strategy for PV household-prosumers with self-consumption/sufficiency enhancement and provision of frequency containment reserve,” *Applied Energy*, vol. 277, 2020. doi: 10.1016/j.apenergy.2020.115529.
- [113] Toshiba, “SCiB cells.” <https://www.scib.jp/en/product/cell.htm>, 2019.

- [114] GS Yuasa, “GS yuasa dual chemistry energy storage system.” <https://www.yuasa.co.uk/2019/01/gs-yuasa-power-the-worlds-first-container-dual-chemistry-energy-storage-system/>, 2021.
- [115] Maccor, “Specifications of maccors s4000.” <http://www.maccor.com/Products/Series4000.aspx>, 2018.
- [116] BioLogic, “Specifications of biologic sp-300.” <https://www.biologic.net/products/sp-300/>, 2021.
- [117] S. Nejad, D. T. Gladwin, M. P. Foster, and D. A. Stone, “Parameterisation and online states estimation of high-energy lithium-titanate cells,” *IECON*, November 2017.
- [118] S. Nejad, D. T. Gladwin, and D. A. Stone, “A systematic review of lumped-parameter equivalent circuit models for real-time estimation of lithium-ion battery states,” *Journal of Power Sources*, vol. 316, pp. 183–196, 2016.
- [119] M. Chen and G. A. Rincon-Mora, “Accurate electrical battery model capable of predicting runtime and I–V performance,” *IEEE Transactions on Energy Conversion*, vol. 21, pp. 504–511, 2006.
- [120] S. Sivanandam and S. Deepa, *Genetic Algorithms*. Berlin Heidelberg: Springer, 2008. doi: 10.1007/978-3-540-73190-0_2.
- [121] K. Deb, S. Agrawal, A. Pratap, and T. Meyarivan, “A fast and elitist multiobjective genetic algorithm: NSGA-II,” *IEEE Trans. Evol. Comput.*, vol. 6, pp. 182–197, April 2002.
- [122] G. L. Plett, “High-performance battery-pack power estimation using a dynamic cell model,” *IEEE transactions on vehicular technology*, vol. 53, pp. 1586–1593, 2004.
- [123] F. Yang, D. Wang, Y. Zhao, K. Tsui, and S. J. Bae, “A study of the relationship between coulombic efficiency and capacity degradation of commercial lithium-ion batteries,” *Energy*, vol. 145, pp. 486–495, 2018.

- [124] S. Mori, M. J. Smith, D. T. Gladwin, and D. A. Stone, “Experimental analysis of efficiencies of a large scale energy storage system,” *2020 2nd IEEE International Conference on Industrial Electronics for Sustainable Energy Systems (IESES)*, pp. 50–55, 2020. doi: 10.1109/IESES45645.2020.9210684.
- [125] B. Sinopoli, L. Schenato, M. Franceschetti, K. Poolla, M. I. Jordan, and S. S. Sastry, “Kalman filtering with intermittent observations,” *IEEE Trans. on Automatic Control*, vol. 49, pp. 1453–1464, September 2004.
- [126] M. J. Smith, D. T. Gladwin, and D. A. Stone, “A comparison of the effects of charging strategies on lithium-ion cell performance in high temperature environments,” *2019 IEEE International Conference on Industrial Technology (ICIT)*, pp. 1107–1112, 2019. doi: 10.1109/ICIT.2019.8755246.
- [127] I. Snihir, W. Rey, E. Verbitskiy, A. Belfadhel-Ayeb, and P. H. L. Notten, “Battery open-circuit voltage estimation by a method of statistical analysis,” *Journal of Power Sources*, vol. 159, pp. 1484–1487, September 2006.
- [128] A. Fairweather, M. Foster, and D. Stone, “Battery parameter identification with pseudo random binary sequence excitation (PRBS),” *Journal of Power Sources*, vol. 196, p. 9398–9406, 2011.

Appendix

.1 Data links

Some operating data of the WESS can be found in the links below:

https://ukerc.rl.ac.uk/DC/cgi-bin/edc_search.pl?WantComp=164

https://ukerc.rl.ac.uk/DC/cgi-bin/edc_search.pl?GoButton=Detail&WantComp=141

Data sheet of the Yuasa modules inside the Yuasa rack and the ADEPT BESS:

http://www.gsyuasa-lp.com/SpecSheets/LIM50EN_Data_Sheet.pdf